

UNIVERSITÀ DEGLI STUDI DI NAPOLI “FEDERICO II”



Department of Chemical Sciences

CHARGE AND PROTON TRANSFER REACTIONS:
INSIGHTS FROM THEORY

Student:
Marika SAVARESE

Tutor:
Prof. Nadia REGA

2011-2014

*that which we are, we are;
...but strong in will
To strive, to seek, to find, and not to yield.*

Contents

Introduction	4
1 On the characterization of electronic excited states and relative processes	12
1.1 Glossary of photoinduced events and processes	13
1.2 Time independent and time dependent density functional theory . . .	18
1.3 Accuracy of TD-DFT calculations	19
1.4 Charge transfer indices: D_{CT} and $D_{CT,react}$	21
1.5 Excited States properties	24
1.6 Hybrid methods	27
1.7 Atom-centered Density Matrix Propagation	28
2 New insights in Rhodamine photophysics: radiative and non radiative decays	30
2.1 Rhodamine dyes	30
2.2 A new protocol to characterize dyes signatures	33
2.3 S_0 and S_1 characterization	35

2.4	Radiative decay process	43
2.5	Non radiative decay processes	48
2.5.1	Structural and Energetic features at the ground and the excited state	48
2.5.2	A non-radiative decay path	53
2.6	Conclusion	60
3	Excited state proton transfer reactions	62
3.1	Structural and electronic features of neutral and anionic species at the ground and the excited state	67
3.2	The energetic aspects of the proton transfer event: ground and excited state potential energy landscape	76
3.3	Analysis of density based indices: D_{CT} and $D_{CT,react}$	81
3.4	A proton shuttle for the phototautomerism	86
4	Proton coupled electron transfer reactions	94
4.1	A model for PCET in oligopeptides	96
4.2	2,4,6-trimethoxyphenylalanine as electron acceptor	100
4.3	Tryptophan as electron acceptor	104
4.4	Results of the molecular dynamics simulation	105
4.5	2,4,6-trimethoxyphenylalanine versus tryptophan: a comparison of relative reactivity	107

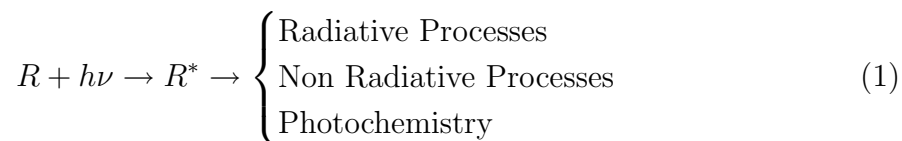
5	On DFT accuracy in describing PCET reactions	111
5.1	Proton coupled electron transfer modeling and benchmarking	112
5.1.1	PCET energy profiles in the gas phase	116
5.1.2	PCET energy profiles with an explicit solvation model	121
5.1.3	PCET energy profiles with an implicit solvation model	122
5.2	Excited state proton transfer modeling and benchmarking	128
5.2.1	Unrelaxed energy profiles	131
5.2.2	Relaxed energy profiles with other functionals	138
6	Non Radiative Decay Process: the Intriguing Spiropyran Case	143
6.1	Structural and electronic features of SPt and BIPS	145
6.2	The energetic aspects of ring opening reaction: ground and excited state potential energy profiles	148
6.3	2D PESs for the HOOP Valley and OBF path	150
6.4	Analysis of density based indices, D_{CT} , for the $S_1 \rightarrow S_0$ interconversion	152
A	Computational details	162
A.1	Rhodamine dyes: Chapter 2	162
A.2	Coumarin dyes: Chapter 3	164
A.3	PCET reaction: Chapter 4	166
A.4	Spyropiran : Chapter 6	167
	Bibliography	167

Introduction

Photochemistry is a science concerned with structures and dynamical processes resulting from the interaction of the light with molecules. [1] Starting from the first step, a molecule absorbing a photon, such many different processes regarding many topics from Biology to Health Science, Energy production, Material science, as well Chemistry, can be individuated.

Some examples of fundamental light induced processes are: Absorption, Fluorescence and Phosphorescence, Charge Transfer (CT), Energy transfer (ET), electron transfer (eT), Proton Coupled Electron Transfer, Excited State Proton Transfer, and straightforward photo-activated reactions. All these processes can be related to a more wide classification.

Let's us consider a generical overall process:



where R is a molecule which absorbs a photon ($h\nu$) and R^* represents the electronically excited molecule, which is essentially the specie in common to photo-physics and photochemistry. According to a traditional classification, Photochem-

istry concerns all processes in which R^* evolves into a product, while, on the other hand, Photophysics includes all the events where R^* does not undergo a net chemical change. [1]

However, the distinction between Photophysics and Photochemistry can sometimes be particularly subtle. For example, how to classify the process by which a molecule maintains the same connectivity between atoms upon the excitation, but evolves into a different stable conformation? As matter of fact, such a distinction is going to be overcome by a more modern vision by which it is possible to model several photo-processes in a unified and consistent manner. This vision is rooted in the most advanced developments of theoretical chemistry.

The picture of photochemistry and photophysics given by theoretical and computational chemistry can be introduced recalling the definition of Potential Energy Surface (PES), namely the electronic potential energy function of the $3N - 6$ independent nuclear coordinates of a molecular system. The several processes listed in the so-called Jablonsky diagram can be detailed and described in terms of transitions, interconversions, and couplings among several electronic PESs. On the other hand, photoreactivity can be described in terms of relaxation evolution along the PESs as well.

An example of hypothetical ground and first excited PESs, and related possible photo-processes that can occur are reported in Figure 1 (we consider the two states having the same multiplicity).

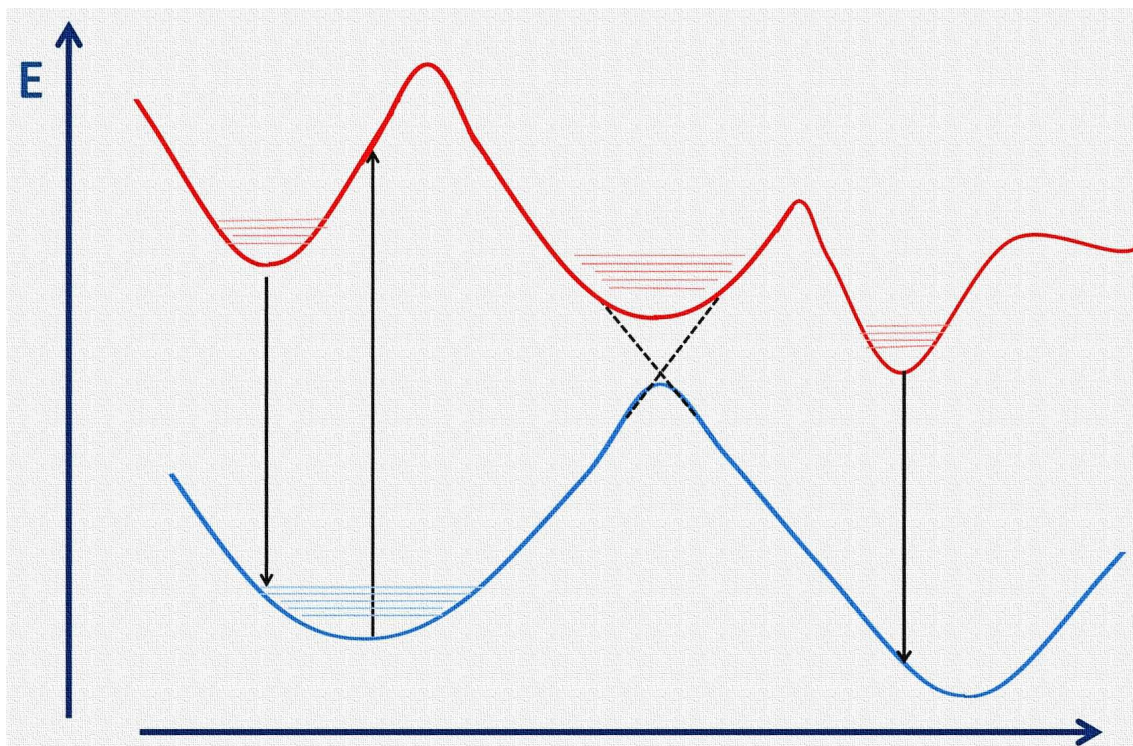


Fig. 1: Ground and Excited State Potential Energy Surfaces. Arrows represent some processes that can occur when light interact with a molecule

Thanks to recent advances in the electronic structure theory, it is possible nowadays to reconstruct with accuracy both the ground and the excited PESs. Moreover, we have the possibility to locate and characterize stationary points of excited PESs, which are associated with a chemical photoreaction. [2]

Therefore, we can carefully analyze by a theoretical-computational perspective all the steps of an hypothetical process starting with the interaction of the light with the matter. The theoretical-computational study can be also a powerful tool able to separately analyse the structural, electronic, and environmental factors affecting an excited process, finding useful structure/property connections.

Many of recent advances in electronic theory is due to Density Functional Theory, DFT, and its Time Dependent version, TD-DFT, allowing for applications to real-world molecular systems with a good compromise between accuracy and computational cost. The main purpose of this Ph.D. project has been the study and the characterization of examples of phenomena which are initiated by the interaction of light with matter, through the use of sophisticated methodologies provided by DFT and TD-DFT.

Moreover the main motivation has been to provide new points of view and insights to such fascinating phenomena, keeping in mind a stairways of growing complexity.

As first instance the study and the characterization of photophysical processes, such those finding an experimental counterpart in spectroscopy have been taken into consideration. Quantities related to radiative decays of a family of xanthenic dyes has been characterized and analyzed. The development of a theoretical model to obtain some relevant photochemical parameters (radiative decay constant, excited state lifetime and quantum yields) from calculated quantities to be compared with experimental counterparts, represented the first issue afforded during the Ph.D. After that, it was taken into consideration the analysis of non radiative decays, and in particular factors affecting the quenching of rhodamine dyes excited states. [3] Charge transfer and photo-induced electron transfer are the main actors which regulate the balance between radiative e non radiative decay constants.

As a further step, photochemical reactions based on Proton Coupled Electron Transfer (PCET), including the so called Excited State Proton Transfer (ESPT), playing a key role in many biological and electrochemical processes, have been taken into consideration. [4,5]

More in details, a light induced Proton Transfer, PT, between a coumarin dye and a base molecule was taken under study [6]. The analysis of this excited state reactivity have been supported by the use of the so-called electronic density based indices. In this direction it is very promising the development of such new tools, *ad hoc* designed indices to search and analyse possible excited state minimum energy reaction pathways, has been proven to be very promising. Very interestingly, after irradiation in presence of a great amount of base and in presence of a non-protic solvent, different emitting specie have been experimentally detected, related to the tautomerism of the coumarin dye. Concerning the photo-tautomerism of the coumarin, a possible base molecules chain which provides the way to transport a proton from one oxygen atom of the coumarin to the other has been analyzed in terms of feasibility and reliability. [7] Thanks to a combined analysis of energetics and electron density based indices, it was individuated the photo-acidity of the dye as the driving force of the entire process, for both the first event of coumarin-deprotonation and the following inter-bases proton transfer. Moreover, regarding to the first PT event, a combined analysis of different electronic density based indices resulted to be able to locate possible excited state reaction path. [8]

Then it was analyzed the Proton Coupled Electron Transfer Reaction, for an oligo-peptides in solution which has been experimentally characterized. [9] A first challenge regarded the accurate description of both the ground and the excited state PESs, in order to have a clear definition of the reaction space, including micro and bulk solvation effects. The benchmarking of various levels of theory in describing the PCET in gas phase and in aqueous solvent was performed. Once tuned the method, it has been investigated the influence of solvation effect on the PCET event in oligopeptides. Moreover, by comparing results obtained with two different electron acceptors, an explanation of the experimental trend was given.

Finally, the photo-chromism of a well known member of a family of photo-switches was taken under study. From ultra-fast experiments [10] the spiropyran to merocyanine conversion is known to take place in less than 100 fs and the measured quantum yields of the conversion is less than 0.1. To explain the low quantum yield of the reaction, and to explore the energy path along the S_1 surface, a DFT analysis was performed. It was investigated the possibility to better understand this S_1 path with combined analysis of energetics and electron density based indices. Particular attention has been paid to the non radiative decay affecting the ring-opening reaction. In this direction it has been explored the possibility of analyse this effect through the use of a new parameter able to account for the non radiative decay probability. The discussion on each case of study is given in the following chapters, after a brief methodological introduction on the treatment of excited states. Fi-

nal remarks and a perspective on future developments are given in the Conclusion.

Technical details on the computational protocols adopted during the work are given

as Appendix.

Chapter 1

On the characterization of electronic excited states and relative processes

"The beauty of DFT is that the formalism is exact...

... all the complexity is hidden in one term, the exchange-correlation functional.

Insight into Current Limitations of Density Functional Theory, *Science*, **2008**

Before to give an overview of methods used and implemented during this work, a glossary of elementary photoinduced events and reactions is given in the following Section.

As mentioned in the Introduction, the first step for an accurate analysis of light induced processes is the representation of ground and excited PESs.

To this aim, both time independent and dependent methods based on the Density Functional Theory (DFT) will adopted. Even if, a detailed description of methods rooted in DFT is out of the purpose here, a rapid sketch is provided in Section 1.2. An accurate description of a given PES starts with the so-called *methodologi-*

cal calibration, therefore performances of several functionals in providing excitation energies is discussed in Section 1.3.

Furthermore, another theoretical challenge is represented by the description and analysis of excited state PES through new excited state properties descriptors, i.e., *ad hoc* designed parameters developed to describe the intrinsic charge transfer character of a given excitation [11], or to search and analyze possible excited state minimum energy path [8]. The theoretical formulation of such indices is reported and discussed in Section 1.4.

TD-DFT calculations have been widely employed here to model molecular absorption and emission for organic dyes, and it has been also combined with hybrid schemes to mimick specific interactions with bulk solvent or to deal with large biomolecules. Some details about hybrids approaches are provided in Section 1.6.

Finally, to have a clear definition of the reaction space including micro and bulk solvation effects methods rooted in ab-initio molecular dynamics have been also considered. In Section 1.7 the atom-centered Density Matrix Propagation (ADMP) method is rapidly overviewed.

1.1 Glossary of photoinduced events and processes

Traditionally, processes occurring when a molecule absorbs a photon can be represented through an energetical diagram, for example the Jablosky one, which is an efficient scheme of the possible photophysical processes involving transitions between two electronic states. [12]

Regarding radiative processes, the following events are possible:

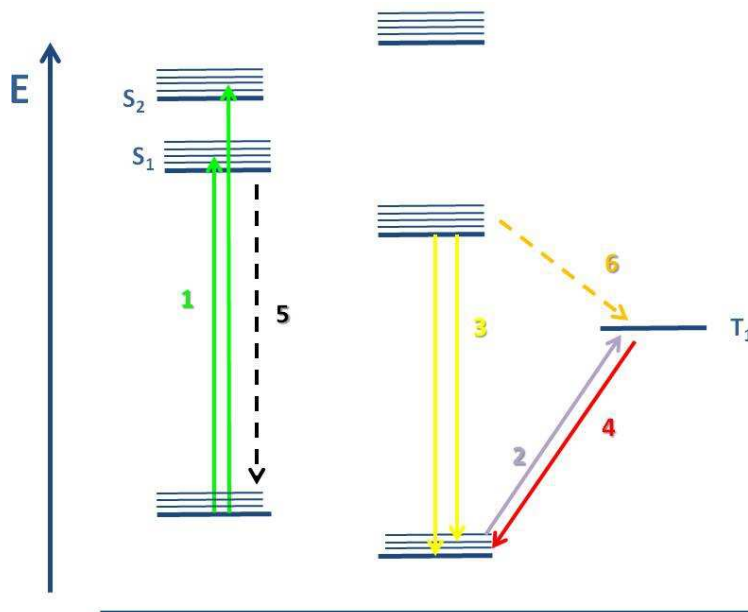


Fig. 1.1: Jablonsky diagram.

-1 "Spin allowed" singlet-singlet absorption, e.g. $S_0 + h\nu \longrightarrow S_1$

-2 "Spin forbidden" singlet-triplet absorption, e.g. $S_0 + h\nu \longrightarrow T_1$

-3 "Spin allowed" singlet-singlet emission, characterized by a rate constant K_F ,
e.g. *fluorescence* $S_1 \rightarrow S_0 + h\nu$

-4 "Spin forbidden" triplet-singlet emission, characterized by a rate constant K_P
e.g. *phosphorescence* $T_1 \rightarrow S_0 + h\nu$

All these processes involve the absorption or the emission of a photon. Singlet-triplet absorption and triplet-singlet emission are referred to as *forbidden processes*, although they are actually *plausible* with low probability.

There also *radiation-less* processes:

-5 "Spin allowed" transition between states of the same spin, called *internal conversion*, e.g. $S_1 \rightarrow S_0 + \text{heat}$

-6 "Spin forbidden" transition between states with different spin, called *intersystem crossing* e.g. $S_1 \rightarrow T_1 + \text{heat}$

If no other deactivation processes takes place, the excited state will emit a photon and the *fluorescence* process will bring the excited state to its ground level. Thus, any other process must take place in a time scale shorter than that associated with *fluorescence*. The *fluorescence* $S_1 \rightarrow S_0 + h\nu$ rate constants of organic molecules cover a range of $10^9 s^{-1}$ - $10^6 s^{-1}$ orders of magnitude and competitive processes must take place in a shorter time period.

The Jablosky diagram in figure 1.1 is not complete, because *photochemical reactions* can occur to dissipate the extra energy of an excited molecule. In addition to radiative and non radiative decays, the excited state molecule can undergo reaction which can be of intra- or inter-molecular type. In the case of inter-molecular reaction, the excited state molecule can interact both with a ground state molecule or an excited one.

In the framework of frontier molecular orbital theory [13] the absorption process can be described by a simplified picture, according to which an electron "jumps" from the Highest Occupied Molecular Orbital(HOMO) to the Lowest Occupied Molecular Orbital(LUMO), resulting in a system characterized by two half-filled orbitals. The stabilization of R^* depends on the overlap of and energy differences between HOMO

and LUMO.

More in general, electron transfer (eT) is one of the most important processes than can be photoinduced, occurring both in intra-or-inter molecular manner.

Important example of eT based reactions, are given by some proteins involved in the conversion of light into chemical energy in photosynthetic reaction centers. [14]

Photo induced eT processes, actually belong to the wider class of excited state charge transfer (CT) processes, namely, reactions in which a charge redistribution occurs between an initially reactant state and a well defined product state.

In the case of eT a net charge is transferred. In this respect it is important to evidence that, from a theoretical point of view, the transfer of the electron, or more in general of a charge, does not take place at a fixed electronic configuration.

On the contrary, the electronic wave function changes from the initial one, ϕ_{react} , to the one of the product ϕ_{pro} . It follows that a reorganization of all molecular orbitals is involved while the transfer occurs.

It is also possible to individuate a molecular portion which act as a Donor of the electron, and an Acceptor one. If the Donor and the Acceptor are well separated in the space the process is called *through-space* eT, with the maximum distance at which reaction can occur is generally fixed at 20 Å. Otherwise, a molecular bridge can participate to the transfer with some unoccupied orbitals, and the reaction is called *through-bonds* eT.

In this case, two distinct mechanisms has been individuated: *superexchange* or

electron tunneling and the *hopping* mechanism. While the electron tunneling is a one step mechanism strongly dependent on the distance between the Donor and the Acceptor, the hopping mechanism provides a path for electron transfers across long distances.

Another elementary reaction that can occur in the electronic Excite State is the Proton Transfer (ESPT). [15] ESPT reactions can be prompted by the enhance of pK_a of a certain molecule, as it was observed for example for 1-naphtol, [16–18] thanks to recent developments of ultra-fast spectroscopies. [19] ESPT reactions can occur between different molecules or in an intra-molecular way.

Finally, the coupling between electron and proton transfer reactions gives rise to the Proton Electron Transfer (PCET) reaction which plays a vital role in many biological processes such as photosynthesis, enzymatic reactions, and others chemical devices.

A very relevant example provided by Nature of the PCET capability, is represented by the photooxidation of water into dioxygen by Photosystem II oxygen evolving complex. [20] Further complication can be met when dealing with PCET reactions, because the transfer of the electron and the proton may be sequential, where either the electron or the proton transfers first, or concerted, in the case they transfer simultaneously.

1.2 Time independent and time dependent density functional theory

Density functional theory (DFT) is a quantum mechanical tool used to investigate the ground state electronic structure of many-electron system, through the use of the probability density $\rho_0(r)$ which allows us to replace the complicated N -electron wave function ψ by collecting all observable properties of a static many-electron system into a density which in turn depends on only three variables collected into r . [21,22].

The ground state Energy E_0 is a functional of $\rho_0(r)$, which in turn depends on the external potential, namely, the potential the electrons experience due to the nuclei, which is different for different systems under study :

$$E_0 = E_v[\rho_0(x, y, z)] \quad (1.1)$$

Accurate DFT allows us to predict many interesting features such as atomic energies, vibrational and rotational energies, reaction energies with high accuracy and an affordable computational cost for realistic systems. The tendency of approximated functionals to spread out electronic density, determines the so called "self interaction error" (SIE), which is one of the fundamental problems in ground state DFT. [23] It is well defined for one electron systems and analogies have been done with many electron one, [24, 25] with consequences with underestimations of transition state energies and reaction barriers. [26] Another problem affecting DFT concerns the dealing with degenerate or near-degeneracy systems, namely, associated to multideterminant wave function, due to the intrinsic mono-determinantal

nature of DFT. [27]

In these years, it is provided carefully attention to the accurate representation of both the ground and excited states PESs. In particular the excited state representation have been achieved by the time-dependent version of the density functional theory [28–31]. The conceptual and computational foundations of TD-DFT are similar to the corresponding for DFT, but regard a time-dependent density instead of an independent one. The formal foundation of TD-DFT is the linear representation of the density response to a time-dependent external potential as the response of non-interating electrons to an effective time-dependent potential. The Rounge-Gross theorem (the analogue of the Hohenberg-Kohn theorem) demonstrates how the time-dependent external potential can be mapped to its time-dependent density in an unique way. A linear response of the initial electronic density in the ground state can be calculated by a self consistent scheme, and from this procedure it is possible to derive the excitations energies of the system. [32]

1.3 Accuracy of TD-DFT calculations

The accuracy of TD-DFT methods in reproducing absorption spectra and properties of optically allowed excited states has been deeply studied, a well known problem of TD-DFT lies in reproducing Rydberg transicions, spin forbidden excitation, double character excitation and charge transfer one.

Investigation about the capability of many functionals ranging from local density approximation functionals (LDA), Gradient-corrected (GGA), meta (GGA), global-

hybrid functionals (GHs), to Range Separated Hybrid functionals (RSHs) in last years [33] have been tested, regarding many topics as for instance, thermochemistry [34–36], binding energies [34, 37], electron affinity [35, 36], reaction energies [38], hydrogen bonds [35, 36, 39], proton transfer barrier [40] charge transfer [36, 41].

Regarding to TD-DFT singlet excitation energies a general trend of LDA functionals is to underestimate vertical excitation energies, deviations in the range of ~ 1 eV are typical of this class, while if pure TD-HF are into consideration overestimations of the energy are found, with an average of ~ 1 eV. A little improvement compared to LDA functionals can be achieved by considering gradient corrected functionals, while meta-GGA performs better. Global Hybrid functionals average between LDA underestimations and HF overestimations. GHs with an HF exchange of 20-25% produces quite accurate excitations. Poor performances are obtained when dealing with transitions presenting a charge transfer with standard global-hybrid functionals (GHs). [42, 43] Regarding to the specific $\pi - \pi^*$ transitions for organic dye, Adamo and co-workers found that the most accurate estimates absorption are obtained by using GHs containing between 22%– 25%.

In this direction in recent years Range Separated Hybrid functionals have been proposed [44–49]. Compared to GH functionals, RSHs ones present a fraction of exact exchange depending on the inter-electronic distance.

The Coulomb attenuated exchange-correlation has been successfully applied to the B3LYP functional in order to gain the CAM-B3LYP one. [50] Recently it was

found that, CAM-B3YLP functional [50] can provide much smaller deviations compared to B3LYP [51] on a group of small chromophores, being the averaged B3LYP error for charge transfer excitation > 0.1 eV.

In this framework it is worth to recall of the Longe range correction scheme (LC correction) applied by Scuseria to gain the LC- ω PBE [48] where the damping parameter, ω , regulates the balance between long and short range exact exchange. In general it was found that RSHs perform similar to GH functionals for singlet $n - \pi^*$ and $\pi - \pi^*$ transition [52, 53]. More in detail, Adamo reported that a LC- ω PBE functionals family member, the LC- ω PBE(20), with a small damping parameter as ($\omega = 0.20$) performs excitations with smaller mean average errors. [52] Self interaction error (SIE) affecting ground state DFT calculations, affects TD-DFT as badly it does with ground state DFT.

1.4 Charge transfer indices: D_{CT} and $D_{CT,react}$

The formulation of the original CT index (D_{CT}), recently developed by Ciofini and co-workers [11] to quantify the spatial extent of a charge-transfer event associated to a vertical excitation, will be here summarized. Having defined $\rho_{GS}(r)$ and $\rho_{EX}(r)$ as the ground and excited state density, respectively, the variation in electronic density associated to an electronic transition is given by:

$$\Delta\rho(r) = \rho_{EX}(r) - \rho_{GS}(r) \quad (1.2)$$

Two functions, $\rho_+(r)$ and $\rho_-(r)$, can be defined collecting, respectively, the points

in the space where an increment or a decrease of the electronic density upon transition is produced and corresponding to positive and negative values of $\Delta\rho(r)$, respectively:

$$\rho_+(r) = \begin{cases} \Delta\rho(r) & \text{if } \Delta\rho(r) > 0 \\ 0 & \text{if } \Delta\rho(r) < 0 \end{cases} \quad (1.3)$$

$$\rho_-(r) = \begin{cases} \Delta\rho(r) & \text{if } \Delta\rho(r) < 0 \\ 0 & \text{if } \Delta\rho(r) > 0 \end{cases} \quad (1.4)$$

Defining R_+ and R_- the barycenters of the spatial regions associated to $\rho_+(r)$ and $\rho_-(r)$, respectively, the D_{CT} can be simply defined as the distance between R_+ and R_- :

$$D_{CT} = |R_+ - R_-| \quad (1.5)$$

This index has been used to quantify the spatial extent of CT excitation in different families of push-pull dyes [11, 54–56] as well as diagnostic index for erratic behavior of standard DFT approaches in the description of through space CT excitations. [11]

A new index ($D_{CT,react}$) has been developed in order to offer a simple, tool to follow excited state reactions. [8] $D_{CT,react}$ is able to describe reactions which implies a concomitant structural reorganization and an intra or intermolecular charge transfer as occur generally in light induced reactions. This new index is defined, as the original one, as a distance between barycenters of two difference density functions, $\rho_{+,react}(r)$ and $\rho_{-,react}(r)$. Nonetheless, these latter are no more related to a vertical excitation, as in the case of the original index. In particular, in the case of $D_{CT,react}$,

$\rho_{GS}(r)$ is fixed to ground state density computed vertically on the minimal energy structure of the excited state PES and thus will be named as $\rho_{GS,minS1}(r)$. $\rho_{EX}(r)$, on the other hand, is defined as the excited state density associated to a given point (i) on the excited PES. As a consequence, $\Delta\rho(r)_{CT,react}$ is defined as:

$$\Delta\rho(r)_{CT,react} = \rho_{ES,i}(r) - \rho_{GS,minS1}(r) \quad (1.6)$$

In analogy with Equations 1.3 and 1.4, $\rho_{+,react}(r)$ and $\rho_{-,react}(r)$ can be defined as

$$\rho_{+,react}(r) = \begin{cases} \Delta_{CT,react}\rho(r) & \text{if } \Delta_{CT,react}\rho(r) > 0 \\ 0 & \text{if } \Delta_{CT,react}\rho(r) < 0 \end{cases} \quad (1.7)$$

$$\rho_{-,react}(r) = \begin{cases} \Delta_{CT,react}\rho(r) & \text{if } \Delta_{CT,react}\rho(r) < 0 \\ 0 & \text{if } \Delta_{CT,react}\rho(r) > 0 \end{cases} \quad (1.8)$$

The associated $D_{CT,react}$ somehow quantifies how much the density changes from the most stable excited state conformation for the reactants along excited state PES, and thus implicitly takes into account both the electronic reorganization upon transition (actually already contained in the original D_{CT} index) and the structural reorganization occurring from the excited state minimum to the excited state actual geometry. It is therefore clear that this index maybe suitable, as in the present case, when aiming at following CT reaction occurring at the excited state, that is under irradiation, more than simply quantifying the vertical (absorption related) CT character.

1.5 Excited States properties

The absorption of a photon involves a transition from the electronic ground state PES to the excited one. From a quantum mechanical point of view, in the Born-Oppenheimer approximation, [57] according to the Franck-Condon principle, [58,59] the excited state geometry has the greatest probability to be close to the ground state equilibrium geometry. The electronically excited state molecule, with a geometry corresponding to the minimum of the ground state PES, will be referred as the Franck-Condon structure. Generally speaking, in all cases previously shown, when a molecule interact with light, the perturbed excited electronic density can differ or not with the ground state one, generating an excitation with a charge transfer character (CT) in the first case, and a locally excited one (LE) in the second case.

In a similar way, the emission of a photon, the fluorescence, takes place from the minimum of the excited state PES and the evolution along the excited state PES will be referred as relaxation process. The number of molecule produced per photon absorbed is called the quantum yield ϕ , and in particular for the fluorescence process, the number of emitting molecules per number of absorbed photons is the fluorescence quantum yield. In principle, during the relaxation, many processes can happen and reduce the occurrence of the fluorescence event, as for example a radiationless deactivation, internal conversion. In the internal conversion event, the vibrational relaxation is an important feature in which electronic energy is converted into vibrational energy associated to the nuclear motion. Moreover, non radiative

decays can involve also, surface crossing with lower-energy surfaces. Transitions between PESs can be very fast, in that case a "funnel" is said to exist, or weakly or strongly avoided. The *lifetime* of an excited state is defined as the time range comprised between the absorption event and the faster process that takes place. In absence of other competitive process the *lifetime* is simply the time range between the absorption event and the *fluorescence* [60]. The measured fluorescence lifetime τ is numerically equivalent to the average lifetime value $\langle \tau \rangle$, this statement being based on the assumption that the fluorescence decay follows a first order kinetic (this is not valid for a fluorophore possessing different lifetimes). Fluorescence lifetime is not a true independent photophysical parameter, and it can be derived from steady-state spectra as first shown by Einstein. [61] He assumed that, when only a radiative emission is allowed between levels 1 and 0, since the fluorescence Einstein coefficient A_{10} has a unit of $[s^{-1}]$, in the absence of any quenching process, the *lifetime*, τ can be expressed as:

$$A_{10} = \frac{1}{\tau} \quad (1.9)$$

The well known Einstein coefficient A_{10} , can be also related to the emission or absorption rate of a classical, single electron oscillator with a frequency ω_{10} . We define an emission oscillator strength f_{10} by the relation:

$$f_{10} = -\frac{A_{10}}{3\gamma} \quad (1.10)$$

where the radiative decay rate is:

$$\gamma = \frac{e^2 \omega_{10}^2}{6\pi \epsilon_0 m c^3} \quad (1.11)$$

where e is the electron charge, m is the mass of the electron, ϵ_0 is the dielectric constant in vacuo.

An absorption oscillator strength f_{01} is then defined by:

$$g_1 f_{01} = -g_2 f_{10} = g f \quad (1.12)$$

where g_1 and g_0 are the degeneracy of the state 1 and 0, respectively.

We may now relate the absorption oscillator strength to the A_{10} coefficient:

$$f_{10} = \frac{g_1}{g_0} \frac{2\pi\epsilon_0 m c^3 A_{10}}{\omega_{10}^2 e^2} \quad (1.13)$$

The oscillator strength f measures the intensity or probability of an electronic transition to occur, and can be also expressed explicitly in terms of the transition electric moment as:

$$f_{10} = \frac{2mc}{3\hbar^2} (E_0 - E_1) | \langle \psi_1 | \hat{r} | \psi_0 \rangle |^2 \quad (1.14)$$

where \hbar is the reduced Plank constant, E_0 and E_1 are the state energy levels, r is the electric moment operator, ψ_0 and ψ_1 are the two electronic eigenstates, and the integral is the transition electric moment. This relationship, along with expression 1.9, allows us to connect the experimental lifetime with the oscillator strength f and the associated frequency calculated by quantum mechanical methods, according to:

$$\omega^2 f \propto \frac{1}{\tau} \quad (1.15)$$

1.6 Hybrid methods

The balance between the accuracy of results and the computational cost is a very challenge task. The computational cost of accurate methods scales very unfavorably with the system size (N). When dealing with very large systems the scaling problem becomes very severe and the required accuracy can be reached with effort. The so called hybrid methods can constitute a solution to this problem. Basically the idea comes with the observation that different regions of the system under study can play very different roles in the process under investigation, as for example it occurs when dealing with molecules in solution. Thanks to a hybrid methods approach, it is possible to treat each region at a different computational level. In this way the expensive computational method can be only employed for the molecular portion 'where the action takes place', while less expensive methods can be used for the surrounding regions. In this context the ONIOM (Our N-layered Integrated molecular Orbital + molecular Mechanics) method [62] is an oniom skin-like extrapolation method, that allows to combine different quantum mechanical (QM) methods, as well as, a molecular mechanics (MM) method in multiple layer.

The concept of the ONIOM method is extremely simple. In order to gain the total energy of the entire system at the high level method $E(\text{high,real})$ it is performed an inexpensive low level calculation $E(\text{low, real})$ for that system, and an accurate high level calculation for a smaller portion of the system $E(\text{high, model})$. Assuming that the correction for the high level, $E(\text{high, model}) - E(\text{low, model})$, and the

correction for the real system, $E(\text{low, real}) - E(\text{low, model})$, to be additive, the energy of the real system at the high level can be estimated extrapolatively from three independent calculations as:

$$E(\text{ONIOM, real}) = E(\text{low, real}) - E(\text{low, model}) + E(\text{high, model})$$

There is no restriction about combining Molecular orbitals methods (OM) and MM ones, this is a unique signature of ONIOM methods. The definition of the model system is rather straightforward if covalent bonds are not present between the layers. If a solute molecule complexed with one solvent molecule constitutes the real system, the solute will be the model system, and the solute-solvent interaction is included at the low level calculation of the real system.

1.7 Atom-centered Density Matrix Propagation

Methods of ab initio molecular dynamics (AIMD) are based on the calculation of the electronic potential energy surface traversed by the classical nuclei on-the-fly during the dynamics procedure. Both BornOppenheimer (BO) molecular dynamics (MD), as well as, extended Lagrangian molecular dynamics fall into this category.

The Atom-centered Density Matrix Propagation (ADMP) [63–66] method is essentially an extended Lagrangian Molecular Dynamics (MD) scheme in which the electronic degrees of freedom are not iterated to convergence at each step, but are instead treated as fictitious dynamical variables and propagated along with the nuclear degrees of freedom by as a simple adjustment of time scale [63]. Such an

approach offers significant computational advantages for efficient MD calculations. The individual elements of the reduced one-particle density matrix, are chosen as dynamical variables to represent the electronic degrees of freedom. The electronic variables are allowed to have fictitious masses, which leads to a simple adjustment of the relative time scales, thus facilitating the adiabatic propagation of the electronic degree of freedom along with the nuclei. This approximation enables the ADMP approach to predict effectively similar nuclear dynamics as MD on the BO surface, but with a significantly reduction of computational cost.

The ADMP method offers the possibility of simulating systems by accurately treating all electrons or by using pseudopotentials. A wide variety of exchange-correlation functionals can be utilized, including hybrid density functionals. Atom-centered functions can be used with the correct physical boundary conditions for molecules, polymers, surfaces, and solids.

Chapter 2

New insights in Rhodamine photophysics: radiative and non radiative decays

2.1 Rhodamine dyes

Recent literature clearly shows how rhodamine dyes are founding an increasing number of applications as molecular fluorescence probes in different fields ranging from material science, to chemistry and biology, mainly thanks to their peculiar photophysical properties, such as high photostability, sensitivity and selectivity [67–76].

The photophysical behavior of rhodamines is not fully understood or established, in spite of the large amount of studies published along the decades, [77–86] thus, a clear and complete picture of the photophysical behavior of rhodamines is far to be fully and unambiguously established.

Several models have been debated to interpret the quantum yield behavior of rhodamine dyes. [78,80,82–90] All these experimental observations claim for a higher degree of comprehension of the complex decay pathway(s) taking place in such class

of molecules if one aims at obtaining a full control of their photophysical behavior so to achieve a rational design of modern optical sensors.

Nonetheless from a theoretical point of view, the modeling of such type of process, is far to be trivial, especially at TD-DFT level. The main problem spreads from the correct description of the excited state Potential Energy Surface (PES) in regions close to the crossing points between different electronic states or even in regions where they become very close in energy (near degenerate). As a matter of fact, the Born Oppenheimer approximation breaks down in these regions, the non adiabatic coupling terms becoming infinite at the degenerate points.

In this context, qualitative and quantitative tools enabling the characterization of excited state potential energy surfaces are becoming appealing for the description of excited state PES and promising to help for the in-silico design of new fluorescent probes.

Rhodamine dyes are known to have a very low intersystem crossing rate. [78,79] It follows that the non-radiative decay should occur through an internal conversion. Nonetheless, there is not a general consensus on which such a reorganization mechanism is. One of the most corroborated theory indicates a structural rearrangement corresponding to a decrease of the C-N bond order upon the $S_0 \rightarrow S_1$ excitation, as the responsible for non-radiative paths opened through the amino groups torsional motions. [82–86] In fact, rhodamine dyes are usually given as a prototypical examples of the so called Twisted Intramolecular Charge Transfer (TICT) mechanism. [91]

Nevertheless, several arguments against the TICT hypothesis exist, [87, 88] and other mechanisms have been debated in literature, such as, for instance, the Umbrella Like Mechanism (ULM). [78, 80]

In particular, recently, some theoretical works suggested that a dark state (with strong HOMO-1→LUMO character) can interconvert with the fluorescent state in specific cases such as for the tetramethylrhodamine isothiocyanate in water. [89, 90]

Experimentally, and in analogy with what previously observed for the structurally related fluorescein dyes [92], Nagano and coworkers developed Si-Rhodamine-Based NIR fluorescence probes, controlling their fluorescence properties through the tuning of the mechanism of the intramolecular photo-induced electron transfer (PeT). In this case a PeT is indeed taking place from the phenyl group (acting as the electron donor moiety) to the xanthene ring (behaving as the electron withdrawing group). [93]. More recently, Liu and coworkers discussed the possibility of an intra-molecular PeT occurring in Rhodamine B and its derivatives involving the dialkylated amino groups as electron donors [94], while Yan-qiang and coworkers characterized an ultrafast intermolecular PeT between Rhodamine 101 dye and N,N-diethylanyline from a spectroscopic point of view. [95]

Recently, a new density based index was developed, the so called D_{CT} index (for a detailed discussion about D_{CT} index, please refer to Chapter 1). This index, originally devised as a diagnostic tool to identify the erratic behavior of standard DFT approaches in the description of through space CT excitations, has found other

applications, such as a measure of the charge separation efficiency of dyes belonging to different push-pull dyes families [11, 54–56, 96]

In this Chapter, this index will be used to assess and quantify the nature of the excited states involved in the non-radiative decay near the region of their intersection, and, in particular to get insights on the interconversion process to the dark state responsible for the quenching.

2.2 A new protocol to characterize dyes signatures

The emission process can be modeled by a vertical $S_1 \rightarrow S_0$ transition, considering as structure of reference the minimum on the excited energy potential. [97] According to this model, the spontaneous emission decay rate k_r from excited to ground state ($S_1 \rightarrow S_0$ transition) can be expressed as [98, 99]

$$k_r = \frac{4}{3} \frac{\Delta E^3}{c^3} \mu_{10}^2 \quad (2.1)$$

Where ΔE is the $S_1 \rightarrow S_0$ transition energy, c is the light speed and μ_{10} the transition dipole strength in atomic units.

We stress that ΔE and μ_{10} are evaluated on the minimum structure of the excited state potential energy surface, including averaged solvent effects. Eq. 2.1 can be also compared to Eq. 20 in Ref. [100], corresponding to the Strickler-Berg formula for the fluorescence lifetime of molecules. The radiative lifetime τ_r can be therefore

obtained as

$$\tau_r = \frac{1}{k_r} \quad (2.2)$$

Finally, considering the experimental FLIM lifetime τ_{exp} affected by the non-radiative decay rate k_{nr} according to

$$\tau_{exp} = \frac{1}{k_r + k_{nr}} \quad (2.3)$$

we can estimate the quantum yield as the radiative fraction of the total decay rate

$$\Phi = \frac{k_r}{k_r + k_{nr}} = \frac{\tau_{exp}}{\tau_r} \quad (2.4)$$

A fragment analysis of the molecular orbitals was also performed according to the following procedure. We can partition a molecular structure into M_{frag} fragments, and we can decompose the electronic density described by a molecular orbital in terms of fragment contributions as

$$C_{frag} = \sum_{j=1}^{n_{frag}} c_j^2 + \sum_j^{n_{frag}} \sum_{i<j}^{n_{frag}} 2c_i c_j S_{ji} \quad (2.5)$$

where i and j run over the n_{frag} basis set atomic orbitals centered on nuclei belonging to the fragment, c_i is the coefficient by which the basis function enters the molecular orbital, S_{ij} is the basis set overlap matrix element, and

$$\sum_i^{M_{frag}} C_{frag_i} = 1 \quad (2.6)$$

The charge transfer following the $S_1 \rightarrow S_0$ transition and involving a certain molecular fragment can be therefore expressed as

$$\Delta C_{frag} = C_{frag}^{HOMO} - C_{frag}^{LUMO} \quad (2.7)$$

where the reference structure is the minimum of the S_1 potential energy surface.

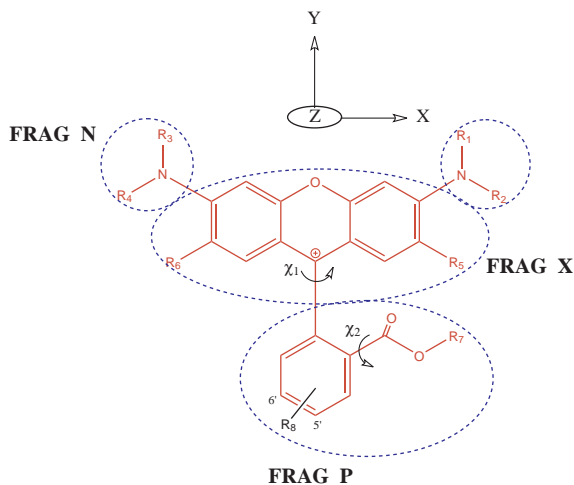


Fig. 2.1: General structural formula, labeling and fragments decomposition of the xantheno dyes studied in the present work.

2.3 S_0 and S_1 characterization

The motif common to all rhodamine dyes is a diamino-xantheno ring with an almost perpendicular carboxyphenyl substituent, this arrangement adopted by symmetry and sterical reasons (see Figure 2.1). The systems chosen in the present work cover a large variety of both amino and phenyl substituents, while pyronin systems (diamino-xantheno dyes), were also investigated as reference. Structural formula and substituents characterizing the xantheno dyes investigated in the present work are reported in Table 2.1. Abbreviations of commonly used names, adopted hereafter to facilitate the reader, are also reported. Being the diamino-xantheno moiety a cation, the rhodamine can be in different forms according to the pH and to the phenyl substituent. More specifically, we considered both cations (Rhod6G, Rhod123, Rhod19, along with PyrB and PyrY) and neutral molecules (RhodB,

5TMR, 6TMR, Rhod101, 5Rox, 6Rox). The theoretical treatment of environmental effects was performed to be consistent with experimental conditions of lifetime measurements, and solvents used for each system are listed in Table 2.1 as well.

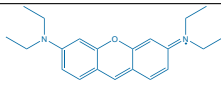
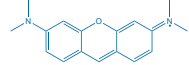
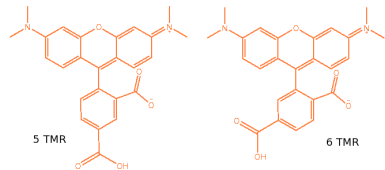
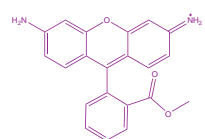
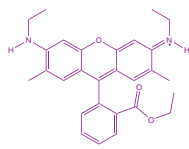
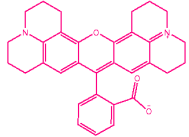
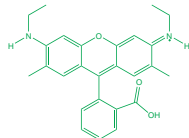
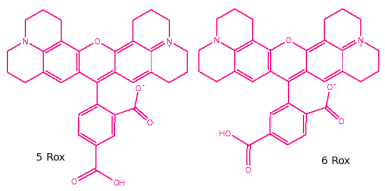
Common name	Abbreviation in this work	Structural formula	Solvent
Pyronin B	PyrB		H ₂ O
Pyronin Y	PyrY		H ₂ O
Rhodamine B	RhodB		ACN
5(6)-Carboxytetramethyl-rhodamine	5(6)TMR		ACN
Rhodamine 123	Rhod123		EtOH
Rhodamine 6G	Rhod6G		ACN
Rhodamine 101	Rhod101		EtOH
Rhodamine 19	Rhod19		MeOH
5(6)-Carboxy-X-rhodamine	5(6)Rox		ACN

Table 2.1: Short names and structural formula of xanthene dyes considered in the present work.

In Table 2.2 we report χ_1 and χ_2 dihedral angles (see Figure 2.1) of the rhodamines optimized in both the ground S_0 and the excited S_1 states at the B3LYP-D/6-31+G(d,p) and TD-B3LYP-D/6-31+G(d,p) levels, respectively.

	$ \chi_1 $		$ \chi_2 $	
	S_0	S_1	S_0	S_1
RhodB	94.8	92.3	0.0	0.1
5TMR	94.6	92.4	0.0	4.7
6TMR	94.5	94.4	0.1	0.5
Rhod123	94.4	122.6	2.6	22.9
Rhod6G	115.2	127.3	25.5	37.9
Rhod101	117.6	123.6	33.8	39.2
Rhod19	111.0	126.9	16.5	12.7
5RoX	116.1	129.3	33.4	34.1
6Rox	117.5	124.6	40.1	42.0

Table 2.2: χ_1 and χ_2 dihedral angles (degrees, see Figure 2.1) of rhodamine dyes optimized in the ground S_0 and first excited singlet S_1 state at the B3LYP-D/6-31+G(d,p)/CPCM and TD-B3LYP-D/6-31+G(d,p)/CPCM levels of theory, respectively.

Dihedral angle χ_1 represents the relative orientation of the phenyl and the xanthene rings, while χ_2 describes the rotation of the carboxy group with respect to the phenyl ring. Therefore, variation from the $\chi_1 = 90^\circ$ and $\chi_2 = 0^\circ$ arrangement accounts for the overall distortion of the two main moieties in rhodamine from the C_s symmetry. X-ray structures exhibit a symmetric arrangement in Rhod123 and a deviation of about 33° from the full symmetry in Rhod6G. [101] This distortion, however, was attributed to crystal packing effects and previous calculations suggested a symmetrical Rhod6G structure. [102]

Concerning our results in the ground state, from inspection of Table 2.2 we note that RhodB, 5TMR, 6TMR and Rhod123 adopt an almost symmetrical arrangement, while a variable and consistent distortion is observed for Rhod6G, Rhod101, 5Rox and 6Rox. The cationic Rhod19 (carboxylic group as phenyl substituent) also shows a less important, but significant distortion ($|\chi_1| \approx 110^\circ$). These results reproduce the different behavior shown by crystallographic structures of Rhod123 and Rhod6G, and demonstrate how the minimum energy arrangement may be driven by several forces. In fact, χ_1/χ_2 distortion can result from a subtle balance of coulombic and non classical interactions involving the two rings and the solvent. C_s symmetry is favored by Coulombic attraction and steric repulsion between the polar carboxy group and the positively charged xanthen. Asymmetry, on the other hand, can lead to stabilizing dispersion interactions between the carboxy substituent and the xanthen. Moreover, distortion may enhance the carboxylic oxygen exposure to the polar solvent, leading to more stabilizing solute-solvent interactions.

After the electronic excitation to the S_1 state, RhodB, 5TMR and 6TMR maintain the ground state C_s symmetry. The methyl ester substituted Rhod123, on the other hand, switches from the almost symmetrical S_0 structure to a largely distorted arrangement ($|\chi_1|=123^\circ$) in S_1 . The remaining rhodamines exhibit an enhancement of about 10° for both the χ_1 and χ_2 angles upon the excitation. Recently, a χ_1 distortion upon electronic excitation has been calculated for the tetramethyl isothiocyanate rhodamine in water, [103] while a different χ_1 adopted in the ground and

excited state has been hypothesized to explain the Stokes shift of Rhod19 experimentally recorded in the gas phase. [74]

A detailed discussion about the absorption and emission spectra of the xanthene dyes is out of the main purpose of the present work, nevertheless some important comments are in order after inspection of Table 2.3, where we report a summary of the absorption and emission frequencies calculated at the TD-DFT level for all the pyronin and rhodamine dyes, compared to the corresponding experimental data.

	Absorption energy		Emission energy	
	TD-DFT	Exp.	TD-DFT	Exp.
PyrB	2.61	2.27 ^a	2.34	2.14 ^e
PyrY	2.64	2.24 ^a	2.35	2.17 ^e
RhodB	2.66	2.29 ^b	2.41	2.18 ^b
5TMR	2.66	2.28 ^c	2.40	2.18 ^c
6TMR	2.66	2.28 ^c	2.40	2.18 ^c
Rhod123	2.88	2.43 ^f	2.51	2.33 ^d
Rhod6G	2.69	2.59 ^g	2.36	2.23 ^d
Rhod101	2.52	2.20 ^b	2.26	2.11 ^b
Rhod19	2.70	2.40 ^b	2.32	2.28 ^b
5Rox	2.46	2.18 ^c	2.10	2.08 ^c
6Rox	2.49	2.18 ^c	2.21	2.08 ^c

a) Ref. [104]; b) Ref. [105]; c) Ref. [106]; d) Ref. [105]; e) Ref. [107]. f)Ref. [108]. g)Ref. [109].

Table 2.3: Absorption and emission energies (eV) of pyronin and rhodamine dyes calculated at the TD-B3LYP-D/6-31+G(d,p)/CPCM level of theory. Experimental values are also reported for comparison.

According to a general trend of TD-DFT methods, [110, 111] previously reported calculations overestimate the rhodamines absorption band peak of about 0.4 eV. [103, 112, 113] Computational results can ameliorate when solvent or dynamical ef-

fects are taken into account. [103]

Our results show the same trend, although the agreement with the experiment improves when the emission energy is considered. In this case we obtain an average error of 0.15 eV with a standard deviation of 0.007 eV. We can reasonably conclude that our TD-DFT calculations provide a comparable accuracy in all cases considered. This consistency is an important prerequisite to pursue further our comparative analysis of rhodamine dyes, because the emission energy, along with the corresponding dipole strength, determine the radiative decay rate k_r according to Eq. 2.1.

According to the theory discussed in Sec. 2.2, radiative lifetime τ_r and quantum yields Φ can be calculated by Eqs. 2.1-2.4 (see Sec 2.2). Results are listed in Table 2.4.

	τ_{exp}	τ_r	Φ_{calc}	Φ_{exp}
PyrB	1.34 ^a	3.22	0.42	0.40 ^a , 0.36 ^b
PyrY	1.77 ^a	3.24	0.55	0.35 ^a , 0.47 ^b
RhodB	1.92 ^c	3.26	0.59	0.53 ^d
5TMR	2.50 ^c	3.42	0.73	/
6TMR	2.50 ^c	3.68	0.68	/
Rhod123	3.60 ^e	3.77	0.89	0.90 ^f
Rhod6G	3.87 ^c	3.89	0.99	0.95 ^f
Rhod101	4.10 ^g	3.81	1.08	0.96 ^f , 0.98 ^h
Rhod19	4.16 ⁱ	4.40	0.94	0.95 ^f
5Rox	4.30 ^c	5.35	0.80	/
6Rox	4.30 ^c	4.05	1.06	/

a) Ref. [104]; b) Ref. [114]; c) this work; d) Ref. [80]; e) Ref. [115]; f) Ref. [105]; g) Ref. [116]; h) Ref. [71]; i) Ref. [117];

Table 2.4: Experimental and calculated lifetimes (ns) for pyronin and rhodamine dyes. Corresponding quantum yields are also reported and compared to experimental counterparts.

Calculated quantum yields Φ_{calc} are also compared to experimental counterparts Φ_{exp} reported from literature, when consistent data in terms of experimental conditions and reference standard are available.

We observe that Φ_{calc} are slightly larger than the corresponding Φ_{exp} : the over-estimation of the TD-DFT emission energy leads to an enhancement of the radiative decay rate and, as a consequence, of the calculated quantum yield.

Nevertheless, Φ_{calc} and Φ_{exp} values are in agreement within an average and maximum error of 0.05 and 0.1, respectively. The experimental trend of the whole set is nicely reproduced, from the low values of pyronines to the value of ≈ 1.0 for Rhod101, which is usually considered as a reference of the full quantum yield. This result is a solid argument in favor of the accuracy of our combined experimental/theoretical approach. In Figure 2.2 we report calculated radiative and non radiative decay rates for the xanthene dyes ordered by an increasing value of Φ .

We note that both the k_r and k_{nr} rates generally decrease with the quantum yield, although the k_{nr} with a larger derivative. Xanthene dyes with a low quantum yield ($\Phi < 0.75$) correspond to k_r and k_{nr} of the same order of magnitude ($k_{nr} > 0.1 \text{ ns}^{-1}$). k_r has been often approximated as a constant with respect to both the rhodamine substituents and the experimental conditions. [77, 118] By contrast, k_r values calculated here cover the not negligible range of 0.124 ns^{-1} .

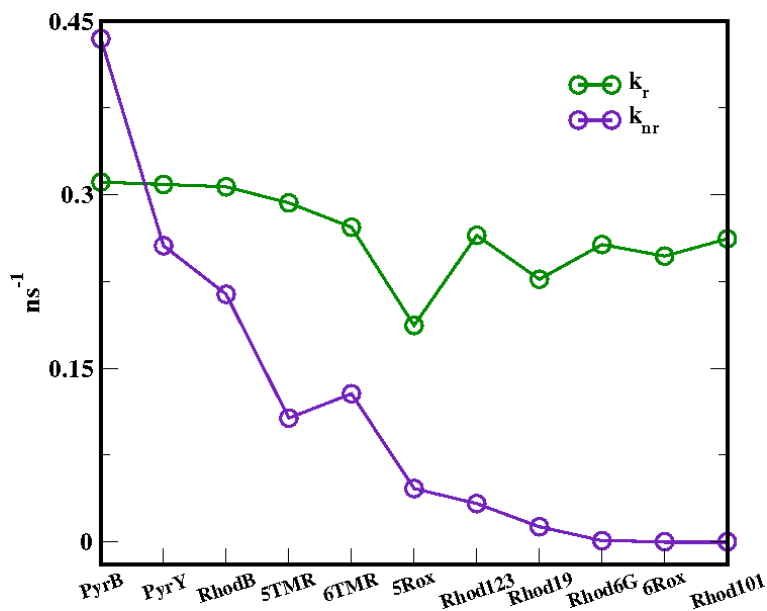


Fig. 2.2: Calculated non-radiative and radiative decay rates (ns⁻¹) for pyronin and rhodamines dyes.

2.4 Radiative decay process

According to Eq. 2.1, the $S_1 \rightarrow S_0$ radiative decay process depends upon the transition energy ΔE and the transition dipole strength $|\mu_{10}|^2$. This latter quantity is increased by the overlap of the ground and the excited electronic density (transition electronic density) along the x axis of Figure 2.1, namely along the direction of the $-N=C-C=C-O-C=C-C-N-$ moiety. [119] On the contrary, transition electronic density involving the phenyl ring (yz plane) gives a zero contribution to the dipole integral.

At first approximation we can analyze the $S_1 \rightarrow S_0$ transition electronic energy in terms of the difference between HOMO and LUMO.

Diamino-xanthe systems are characterized by a π HOMO with a nonbonding

character located on the xantheno ring and, to some extent, on the amino substituents. The π^* LUMO, on the other hand, is mainly located on the xantheno ring and can be partially located on the phenyl ring, depending on the rhodamine structure.

As an example, we report in Figures 2.3 the contours of HOMO and LUMO for Rhod123 in the ground and the excited state structure, respectively. We recall that

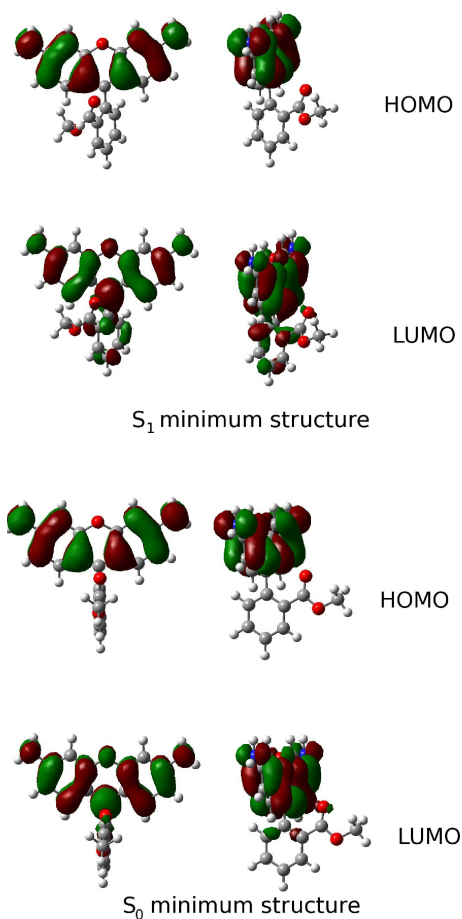


Fig. 2.3: HOMO and LUMO contours calculated at the TD-DFT level for Rhod123. Upper panel: S_0 minimum structure. Lower panel: S_1 minimum structure.

Rhod123 is characterized by a torsion of the phenyl ring with respect to the xantheno plane following the $S_0 \rightarrow S_1$ excitation (See Table 2.2). At variance with the ground

state configuration, we note that the excited asymmetrical structure shows a partial location of the LUMO density on the phenyl ring.

On the basis of the considerations above regarding the symmetry of the transition dipole moment, we can expect that a charge transfer involving the phenyl ring upon the $S_1 \rightarrow S_0$ de-excitation may result in a smaller value of the transition dipole strength $|\mu_{01}|^2$, and, as a consequence, a larger fluorescence lifetime τ_r .

To verify this hypothesis we performed the fragment orbital analysis of Eqs. 2.5-2.7 for our set of molecules in the S_1 optimized structures. More precisely we partitioned the rhodamine derivative into three fragments according to the scheme in Figure 2.1, collecting the xanthene chromophore (FragX), the amino substituents (FragN) and the phenylic group (FragP), respectively. We then calculated the difference between the HOMO and LUMO contributions from the xanthene (ΔC_{fragX}), the amino (ΔC_{fragN}) and the phenyl (ΔC_{fragP}) fragments, assuming these quantities to be representative of the electronic density rearrangement upon the radiative de-activation

The electronic structure of the fragments was analyzed adopting both the B3LYP and the long-range corrected CAM-B3LYP functionals, which gave very similar results. Details are reported as Supporting Information. In Figure 2.4 we report the charge transfer involving the phenyl and the amino fragments ($|\Delta C_{fragP}|$ and ΔC_{fragN}) with respect to the radiative lifetime τ_r , calculated at the B3LYP/6-31+G(d,p) level of theory.

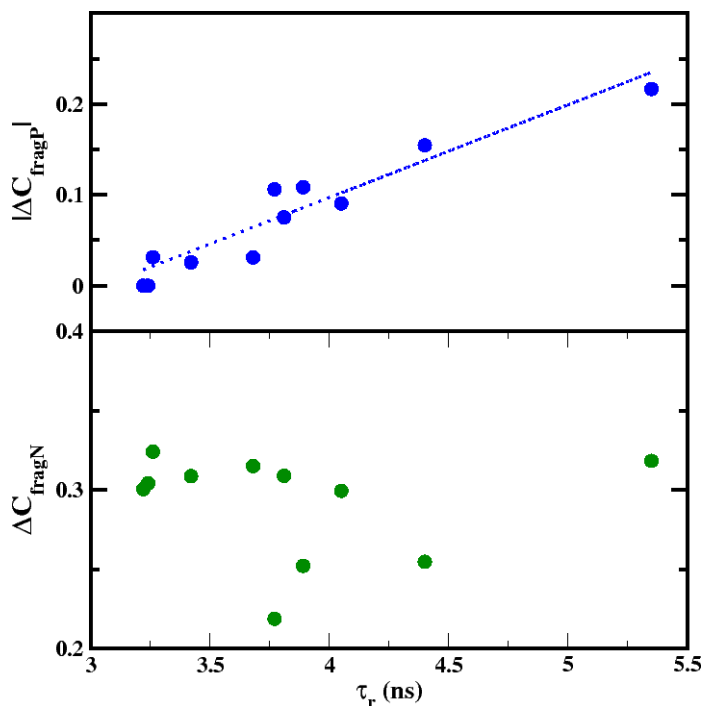


Fig. 2.4: Charge transfer from amino and phenyl fragments (ΔC_{fragN} and $|\Delta C_{fragP}|$) upon the the $S_1 \rightarrow S_0$ de-excitation of rhodamines reported with respect to the corresponding calculated radiative lifetime (ns).

We observe a remarkable linear relationship between the radiative property and the charge transfer amount involving the phenyl fragment, while no dependence is noticed for the electronic density rearrangement on the amino groups.

As we already observed from inspection of the Rhod123 orbitals, the phenyl involvement can be related to the distortion of the rhodamine structure from the symmetrical arrangement ($\chi_1=90^\circ$). In figure 2.4 we report both the phenyl charge transfer $|\Delta C_{fragP}|$ and the radiative lifetime with respect to the χ_1 dihedral angle. We note that the increasing of the xanthene-phenyl torsion results in a larger amount of the phenyl $|\Delta C_{fragP}|$ and a longer lifetime, with a maximum value of 5.35 ns for the

5Rox ($|\chi_1| \approx 130^\circ$), characterized by a 0.22 electron transfer upon the de-excitation.

On the other hand, the S_1 excited state of symmetrical structures (RhodB, 5TMR and 6TMR $\chi_1 \approx 90^\circ$) is characterized by a shorter fluorescence lifetime ($\tau_r \approx 3.5$ ns).

This result suggests an important structure/property relationship: rhodamine dyes characterized by a xanthene-phenyl distortion in the S_1 minimum structure have larger values of the radiative lifetimes.

2.5 Non radiative decay processes

2.5.1 Structural and Energetic features at the ground and the excited state

Starting from the observation reported in previous sections, namely, the classification based on low and high quantum yield rhodamines coincides with rhodamines characterized by symmetric and asymmetric S_1 minimum structures, we considered the hypothesis that, in symmetrical rhodamines, a quenching internal conversion mechanism could be activated by rotation around the χ_1 and χ_2 torsion angles (refer to 2.1 for labeling) leading to a more stable, but dark, excited state.

Indeed, both RhodB and 5TMR molecules in the Frank Condon region are characterized by the presence of two closely lying states : a bright Locally Excited (LE) state, centered on the xanthene moiety, and a dark Charge Transfer (CT) state corresponding to a transition from the carboxyphenyl to the xanthene group.

Both relative energy of these two states and their intensity are expected to depend on the relative orientation of the two subgroup present in the molecule actually ruled by the χ_1 and χ_2 torsion. Indeed, since χ_1 represents the relative orientation of the phenyl and the xanthene rings and χ_2 describes the rotation of the carboxy group with respect to the phenyl ring, any change from the $\chi_1 = 90^\circ$ and $\chi_2 = 0^\circ$ arrangement will account for the overall distortion of the two main moieties in rhodamine from the ideal C_s symmetry.

	$ \chi_1 $	$ \chi_2 $		
	S ₀	S ₁	S ₀	S ₁
RhodB	94.84	92.26	0.01	0.05
RhodB _{asym}	–	62.55	–	19.15
5TMR	94.57	92.37	0.01	4.70
5 TMR _{asym}	–	62.77	–	19.19
Rhod101	117.17	123.87	33.82	39.39

Table 2.5: χ_1 and χ_2 dihedral angles (in degrees, refer to 2.1) computed for rhodamine dyes optimized in the ground (S₀) and first excited singlet (S₁) state at the B3LYP-D/6-31+G(d,p)/CPCM and TD-B3LYP-D/6-31+G(d,p)/CPCM levels of theory, respectively.

From inspection of Table 2.5 it is possible to easily notice that, both at the ground and the first excited state rhodamines such as RhodB, 5TMR all possess a symmetric structure, with the xanthene and phenyl planes almost perpendicular and the carboxyl group lying in the phenyl plane. On the other hand, the Rhod101 dye is rather unsymmetrical the carboxyl group being tilted of about 30-40 degrees with respect to the phenyl ring, this latter being far from orthogonality with respect to the xanthene plane.

Analyzing the vertical transition energies reported in Table 3.2 it can be noticed that in all cases the first absorption corresponds to a $\pi - \pi^*$ excitation (LE state) centered on the xanthene moiety characterized by a high oscillator strength (intensity). On the other hand, the second electronic transition presents a different character depending on the nature of the amino group carried by the xanthene moiety. In the case of RhodB and 5TMR, this state is of intramolecular CT character, corresponding to a transition from the carboxyphenyl group to the xanthene unit, while in the case of Rhod101 this state is still of LE nature, that is centered on the xanthene.

	S_1			S_2		
	Abs.	Oscil.streng.	Character	Abs.	Oscil.streng.	Character
RhodB ^a	2.66	0.9745	LE	2.96	0.1323	CT
5TMR ^a	2.66	0.9111	LE	2.98	0.1321	CT
Rhod101	2.35	1.2563	LE	2.86	0.0203	LE

a) Ref. [3]

Table 2.6: Absorption energies (eV) and oscillator strength (a.u.) of rhodamine dyes calculated at the TD-B3LYP-D/6-31+G(d,p)/CPCM level of theory

Relaxation of the first excited state in the Franck Condon region let to the emission energies and structures reported in Table 2.5 and 3.2, respectively. Generally, and in agreement to what previously reported in literature [3], the level of theory used allows to obtain a good agreement between observed and computed emission energies, with an average error of about 0.15 eV.

	Relaxed S_1			Vertical S_2 at Relaxed S_1 geometry			
	Energy	Oscil. streng.	D_{CT}	Energy	Oscil. streng.	D_{CT}	Exp.
RhodB	2.41 ^a	1.2200	1.201	2.76	0.1504	2.474	2.18 ^b
RhodB _{asym}	1.45	0.0300	2.599	2.34	1.0862	1.200	
5TMR	2.40 ^a	1.1706	1.375	2.77	0.1554	2.477	2.18 ^c
5 TMR _{asym}	1.51	0.0432	2.546	2.29	0.9722	1.443	
Rhod101	2.25	1.1904	1.672	2.71	0.0006	2.631	2.06 ^d

a) [3] b) Ref. [105]; c) Ref. [120]; d) Ref. [94]

Table 2.7: Relaxed S_1 and vertical S_2 excited state energies (in eV) of rhodamine dyes calculated at the TD-B3LYP-D/6-31+G(d,p)/CPCM level of theory. Available experimental values are reported for comparison.

The nature of the emitting state is further confirmed by the analysis of the associated D_{CT} index. Indeed, in the case of RhodB it results that the distance between the

two barycenters of density distribution in the Franck-Condon region is of 1.306 Å and 2.474 Å for the first -relaxed- and second -vertically computed- excited state, respectively (Table 2.7). These data clearly show the larger electronic density reorganization involved in the case of the second excited state and it allows to confirm its intramolecular charge transfer character, in agreement with the orbital picture discussed for vertical excitation. Therefore, both in the case of RhodB and 5TMR basically in the Franck-Condon region, corresponding to symmetric structure with orthogonal rings, the first relaxed excited state corresponds to a bright Locally Excited state (LE) which is found to lie roughly 0.3 eV below a dark CT state. On the other hand, in the case of the asymmetric Rhod101, while the lowest lying state is also of LE character, no closely lying CT states are found.

In order to verify the hypothesis concerning the possibility of a conversion of the bright LE state to a dark CT state by internal rearrangement around $|\chi_1|$ and $|\chi_2|$ in the case of symmetric rhodamines the S_1 structures of RhodB and 5TMR was also optimized starting from an initial distorted guess geometry ($|\chi_1|=110^\circ$, $|\chi_2|=20^\circ$). Starting from this distorted structure, both RhodB and 5TMR relaxed on asymmetrical singlet excited states (here referred to as RhodB_{asym} and 5 TMR_{asym}, respectively) showing clearly asymmetrical structures with $|\chi_1|$ of 118° and 123° for RhodB and 5TMR, respectively as reported in Table 2.5. From an energetic point of view, these singlet states are characterized by a significantly lower energy with respect to those of the corresponding symmetric structures and by a very low

oscillator strength ($f=0.004$ a.u., Table 2.7), in contrast with the high value of oscillator strength computed for symmetric excited singlet state minimum discussed above ($f=1.22$ and $f=1.17$, Table 2.7).

The analysis of the D_{CT} index computed for these asymmetric singlet states allows to clearly define them as ICT ones with of D_{CT} 2.599 and 2.546 Å , respectively for RhodB and 5TMR. On the other hand, the -vertically computed- second excited state shows a clear $\pi-\pi^*$ locally excited state character with D_{CT} of 1.200 and 1.443 Å , respectively. Therefore, both for RhodB and 5TMR not only the two excited states computed in the Franck-Condon region have interconverted upon torsion along the dihedral angles but also, the LE/CT state shows a sizable (about 0.1 Å) decrement/increment of in the electronic density reorganization upon transition. Furthermore, due to the strong stabilization of the dark CT state, the energy difference between the first and the second excited state increases up to roughly 0.9 eV for both RhodB and 5TMR in their asymmetric geometry. In the case of Rhod101 on the other hand starting from a symmetric or asymmetric guess structure for the optimization of the first excited state has no impact on the final results, always corresponding to the same LE distorted structure as reported in Tables 2.5 and 2.7. This is due to the absence of a closely lying CT state which maybe sufficiently stabilized by a structural distortion.

2.5.2 A non-radiative decay path

In order to further investigate possibility of conversion of the bright LE into the dark state CT upon rotation around the χ_1 and χ_2 , in the case of rhodamines presenting a symmetric ground state structure, a linear synchronous path (LSP) consisting of 20 points linking the symmetrical and asymmetrical excited state minima for RhodB was constructed. For each of these structures the second excited state was vertically computed. Basically, this linear synchronous coordinate (c_{LSP}) represents the structural evolution from the symmetrical Franck Condon region ($c_{LSP}=0$), where the emitting state is a bright LE one to the asymmetrical minimum ($c_{LSP}=1$) corresponding to a dark CT state. In order to define the nature of the excited states the D_{CT} index was computed for both first and second excited state for all points along the path. The computed energy profiles associated to the first and second excited states are reported in Figure 2.5 while the associated D_{CT} are reported in Figure 2.6. From the analysis of these figures it is clear that the two excited states cross in the region around $c_{LSP}=0.25$, the detailed study of the crossing being clearly impossible at the level of theory here applied. Indeed, from the combined analysis of the D_{CT} it is possible to point out that in the crossing region also the character of the transitions is inverted. Indeed, the first excited state showing a more local character, translating into a lower D_{CT} value, in the case of symmetric structures becomes of a more marked ICT character moving towards the asymmetric minimum ($c_{LSP}=1$). The inversion of the two states thus allows the conversion of the emissive

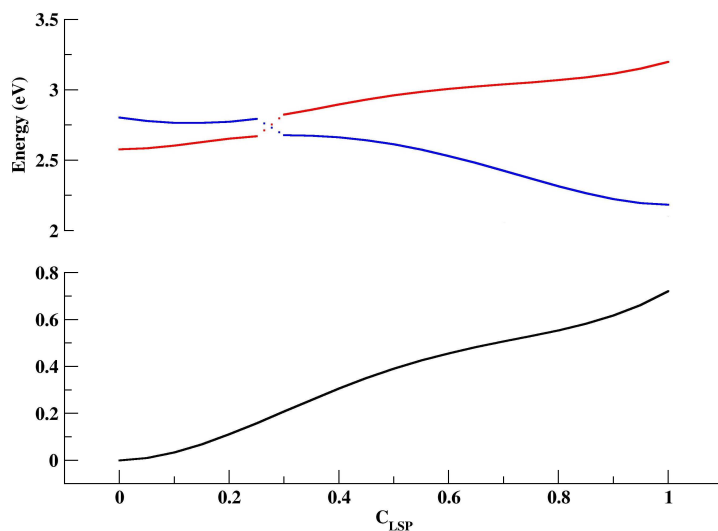


Fig. 2.5: Evolution the energy associated to the LE and CT excited states (in eV) of RhodB along the LSP connecting the symmetrical ($c_{LSP}=0$) to the asymmetrical $c_{LSP}=1$ excited state minima

bright LE state present in the Franck Condon region to the dark CT and more stable distorted minimum thus justifying a low yield for this compound.

Nonetheless the question still unanswered is related to the electronic reason that causes the inversion of the excited states. Analysis of the molecular orbitals mainly involved in the one-electron excitations describing at TD-DFT level the excited states for RhodB, allows clarifying this point. Actually, at any point of the LSP, the first (or second) excited state corresponds essentially to a one electron excitation from the HOMO (or HOMO-1) to LUMO. While the LUMO (reported in Figure 2.7) is completely insensitive to the structural rearrangement occurring along the LSP and keeps always the same nature (localized on the xanthene unit) and energy this is not the case for the HOMO and HOMO-1 as shown in Figure 2.7.

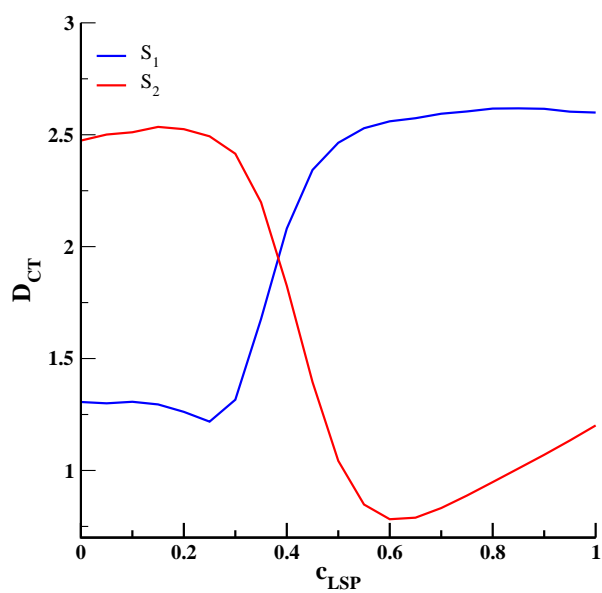


Fig. 2.6: Evolution of the D_{ct} (in Å) associated to the first S_1 and second S_2 excited states computed along the LSP connecting the symmetrical ($c_{LSP}=0$) to the asymmetrical ($c_{LSP}=1$) excited state minima of RhodB.

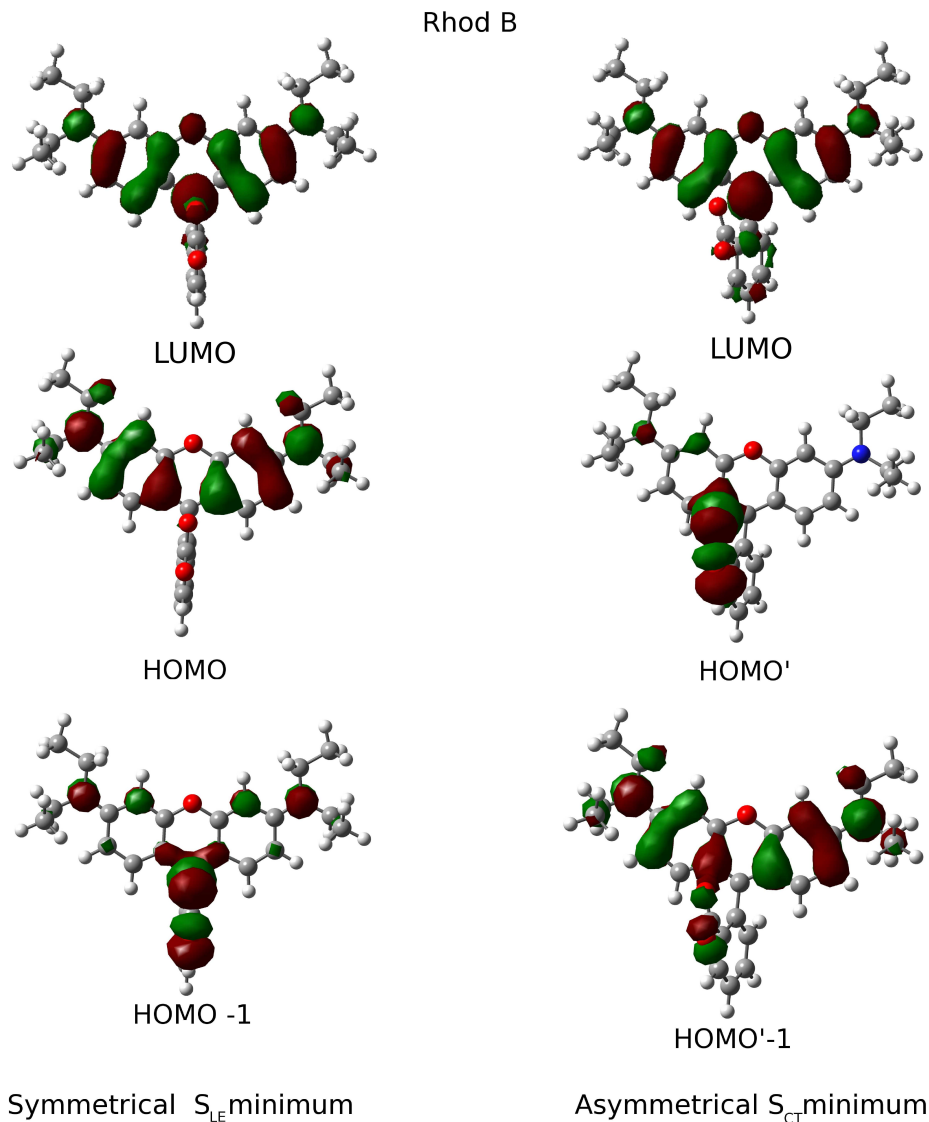


Fig. 2.7: LUMO, HOMO and HOMO-1 computed for symmetrical and asymmetrical RhodB structures corresponding to the optimized first singlet excited state.

For the symmetric structure, the HOMO is essentially a π xanthenic orbital with associated orbital energy (ϵ) of -0.211 a.u., while the HOMO-1 is mainly localized on the carboxylate group on the phenyl substituent lying roughly 0.018 a.u. below the HOMO. As a consequence the HOMO \rightarrow LUMO excitation leads to the LE

first excited state responsible for the radiative decay providing fluorescence. The HOMO-1 \rightarrow LUMO excitation, on the other hand, leads to a dark CT excited state. Considering the asymmetrical minimum ($c_{LSP}=1$), we notice that the HOMO and HOMO-1 actually corresponds to carboxylate and xanthen centered orbitals, respectively with corresponding ϵ values of -0.195 a.u. and -0.218 a.u. That means that the HOMO and HOMO-1 have inverted with respect to the symmetrical minima. This inversion is related mainly to the strong destabilization of the doubly occupied carboxylate centered orbital while the xanthen centered one is actually almost unaffected. The destabilization of the carboxylate orbital is related to the increasing repulsion with the xanthen π systems which is also responsible for the increase in the total energy of the ground state of the molecule. Noteworthy, the frontier orbitals inversion when going from a symmetrical to an asymmetrical arrangement can be schematized as an hole transfer from the xanthen to the carboxylate moiety at the excited state as shown in Figure 2.8. In this simplified orbital

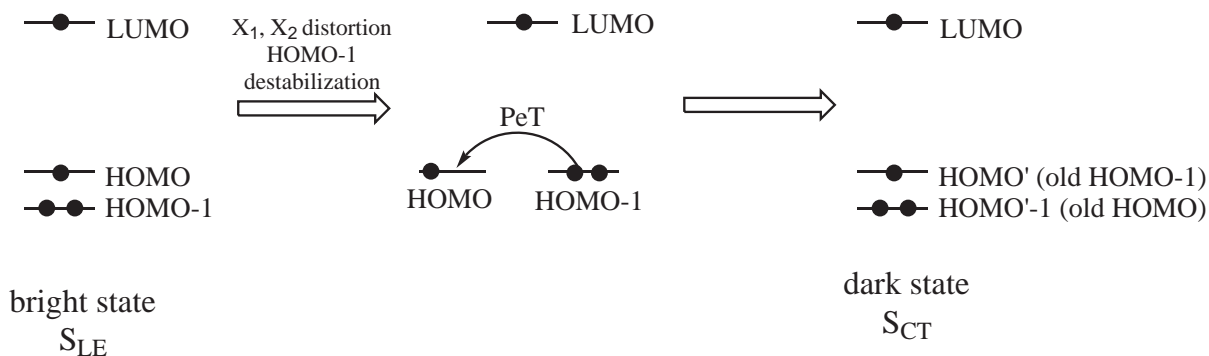


Fig. 2.8: Scheme of the photo induced electron transfer mechanism active in RhodB.

picture, the starting first excited state is the bright state LE state populated in the

Franck Condon region, schematically represented by singly occupied HOMO and LUMO and a doubly occupied HOMO-1. Upon relaxation, corresponding to the distortion of xanthene and phenyl rings, the HOMO-1 undergoes a destabilization and eventually switches with the HOMO. This orbital interchange actually allows an electron transfer from new HOMO (previously HOMO-1) to HOMO-1 (previously HOMO), leading to the final dark state. The quenching mechanism described above is triggered by the destabilization of carboxylate group orbital so that this mechanism should thus be active in principle for all rhodamines. Indeed, for rhodamines that show no contribution stemming from the carboxylate group to the lowest lying excited state, this quenching mechanism is completely negligible. This is actually the case of all asymmetric rhodamines since in such case the carboxy group always contributes to more internal orbitals. As an example, in 2.9 the HOMO-1 computed for the symmetric structure of RhodB, 5TMR can be compared to that computed for the Rhod101. For the latter system (Rhod101), at variance with dialkyl- and tetraalkyl- amino rhodamines, the HOMO-1 is mainly localized on the xanthene ring. It is reasonable to assume that in this case the above discussed quenching mechanism is precluded and this is also the reason why a single minima on the first excited state potential energy surface of LE character is found, always corresponding to a distorted structure.

In order to check that the mechanisms and results discussed above are not affected by methodological artifacts related to the use of a global hybrid functional (B3LYP)

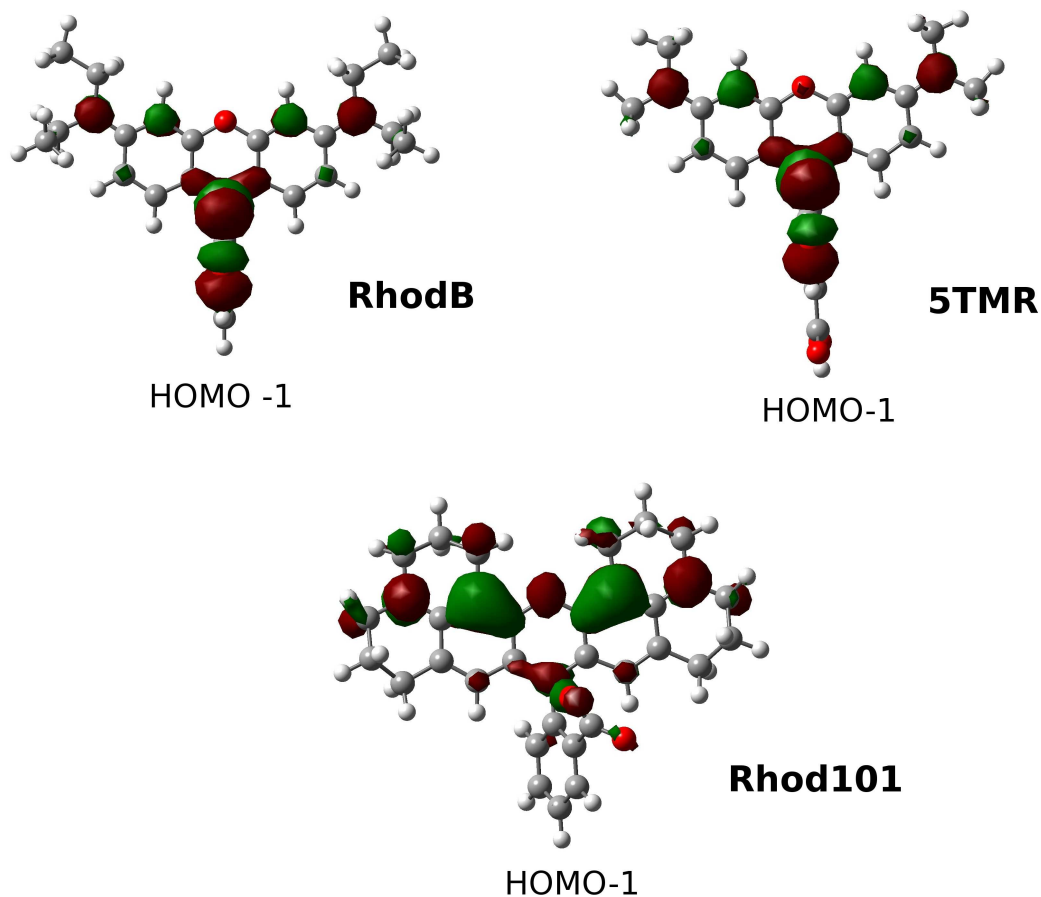


Fig. 2.9: HOMO-1 orbitals computed for RhodB, 5TMR and Rhod101 their Franck Condon first excited state minimum energy structure (symmetric structure for RhodB and 5TMR; asymmetric structure for Rhod101)

for the description of the relative energy of an ICT and LE state, CAM-B3LYP calculations were also performed on the symmetric and asymmetric excited state [46]

The results obtained at the TD-CAM-B3LYP/6-31G+(d,p)/CPCM level in acetonitrile qualitatively producing the same picture and discussed above, confirming our analysis.

In this context worth recalling that, the accuracy of global hybrids such as B3LYP in the description of CT states when combined with LR-PCM has been previously

reported and analyzed. [43, 121] Indeed, the good results obtained are probably ascribable to an error compensation since global hybrid functionals over-stabilize CT excitations while the linear response treatment of the solvent leads to an under-stabilization of states characterized by a large change of the electric moment, such is the case of CT states. [122].

2.6 Conclusion

Fluorescence lifetime and quantum yield of several commonly used rhodamine dyes by combining TD-DFT calculations were systematically analyzed.

It was demonstrated that the photophysical trends in rhodamines are tuned by the interplay of different interactions involving the two main moieties of the molecule, namely the phenyl and the xanthene rings. Quantum mechanical calculations of minimum structures in the fluorescent excited state can be combined with experimentally determined fluorescence lifetimes to gain quantum yield values in good agreement with experimental counterparts. Moreover, the radiative lifetime depends on the amount of charge transfer occurring from the xanthene toward the phenyl group upon the $S_0 \rightarrow S_1$ excitation. This transfer, on turn, can be related to the xanthene/phenyl relative orientation assumed in the S_1 minimum structure. This orientation is variable upon amino and phenyl substituents, is modulated by the solvent, and, in general, is increased when going from the ground S_0 to the excited S_1 state.

By combining experiment and theory we provide a procedure to better under-

stand the complex photophysical behavior of fluorescent probes.

A possible non radiative decay pathway able to explain the different quantum yield observed for different type of rhodamine dyes has been investigated and supported by theoretical analysis of the ground and excited state potential energy surfaces performed at DFT and TD-DFT level. This mechanism, active for rhodamines where two different excited state of bright (LE) and dark (CT) character are sufficiently close in energy in the Franck-Condon region, is triggered by a structural deformation involving the mutual rotation of the xanthene and carboxyphenyl moieties and it can be schematically interpreted as a Photo-induced intramolecular electron transfer. Beside the possibility of using the theoretical tools here applied to the modeling of other emission processes, more interestingly we hope that the elucidation of this non-radiative decay path may help the design and synthesis of new systems and, in particular, of rhodamines with enhanced emission properties obtained by the suppression of this de-activation pathway by chemical modification (such as inclusion of bulky, but electronically inert substituent or by rigidification of the molecular skeleton).

Chapter 3

Excited state proton transfer reactions

Recently great attention has been paid to the study of the the so called Excited State Proton Transfer class of reactions (ESPT). [4, 5, 123–126] The driving force for this type of reactions is indeed the change (i.e. increase) in acidity of a given molecule induced by irradiation (usually referred to as photoacidity). [127] At experimental level, ESPT reactions can indeed be followed using ultra fast pump-probe and time resolved emission experiments, [128] or coherent Raman methods [129, 130] and they can occur, either at intra- or inter-molecular level. From a mechanistic point of view, the irradiation produces the population of charge transfer (CT) excited state characterized by an electronic distribution that changes the acidity of the protonated site of the molecule allowing for its spontaneous deprotonation. The consequent PT reaction can occur either at the intra- or intermolecular level (for instance to a solvent molecule or to a specific base molecule present in solution).

The detailed experimental information available in literature for many ESPT

reactions has pruned their theoretical investigation mainly aimed to an accurate description and analysis of the Potential Energy Surface (PES) associated to the ground or excited state PT reaction.

It is not surprising, therefore, that ESPT reactions are very sensitive to the quantum approach used, as illustrated by several papers. [131–139]

Recently, Hammes-Schiffer and co-workers, [140] showed that beside post-Hartree Fock methods also an accurate DFT approach, taking also into account the effects of the environment, could be successfully applied to get a fairly quantitative characterization of the Excited State PES describing the PCET reaction between two organic molecules (4-hydroxy-4-nitro-biphenyl and t-butylamine in 1,2 dichloro-ethane, recently experimentally investigated by Westlake and collaborators [128]). This theoretical work also highlights the intrinsic difficulty in defining possible proton transfer reaction coordinates over the internal coordinate space. Therefore, beyond their intrinsic relevance in chemistry and biology, PCET and ESPT reactions represent a challenge for theoretical approaches, requiring both electronic structure methods giving an accurate description of the ground and excited state PES and a clear definition of the reaction space.

In this context, the goal of the present work is to show how, using reliable and robust DFT approaches, it is possible to correlate the charge transfer character of ESPT to the main photophysical features of the reaction, including the characterization of stationary points of the ES PES. In particular, well-suited electronic density

based indices can be of great support in providing hints on the most probable reaction channels.

To illustrate this approach, the ESPT occurring between 7-hydroxy-4-(trifluoromethyl)coumarin (CouOH, Figure 6) and 1-methylimidazole (1-MeId, Figure efabrname) schematically represented in Figure 5.9 is here considered as case study.

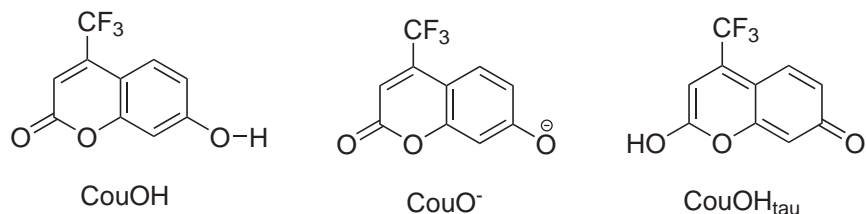


Fig. 3.1: Acronyms and structural formula of the species considered in this work.

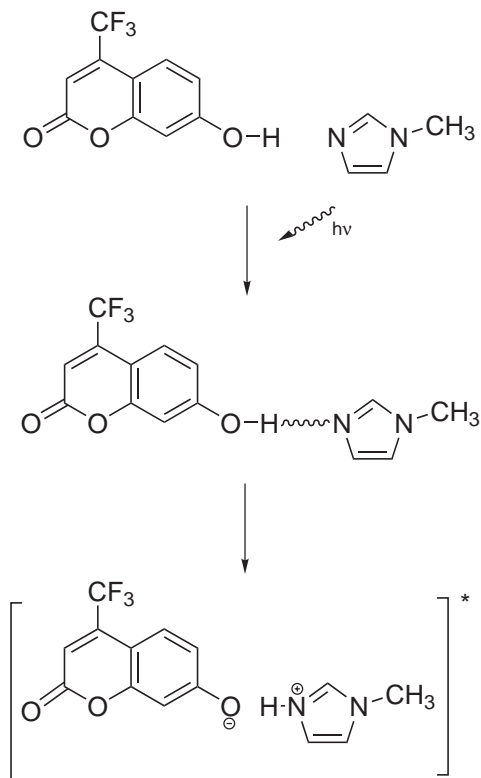


Fig. 3.2: Schematic representation of the ESPT reaction analyzed in this work

Recently, this system was deeply characterized by Papanikolas and co-workers from a spectroscopic point of view and both the nature and the mechanism of the excited-state proton coupled electron transfer reaction were analyzed as a function of the concentration of the base molecule, using ultrafast pump-probe and time resolved methods. [6].

We also focused on the proton shuttling mechanism, mediated by a chain of coordinating base molecules, which has been experimentally proposed to justify the formation of the emissive photoproduct, characterized as the CouOtau- - 1MeIdH⁺ adduct, from the normal form of CouOH initially excited (see Figure 3). [6] Since in

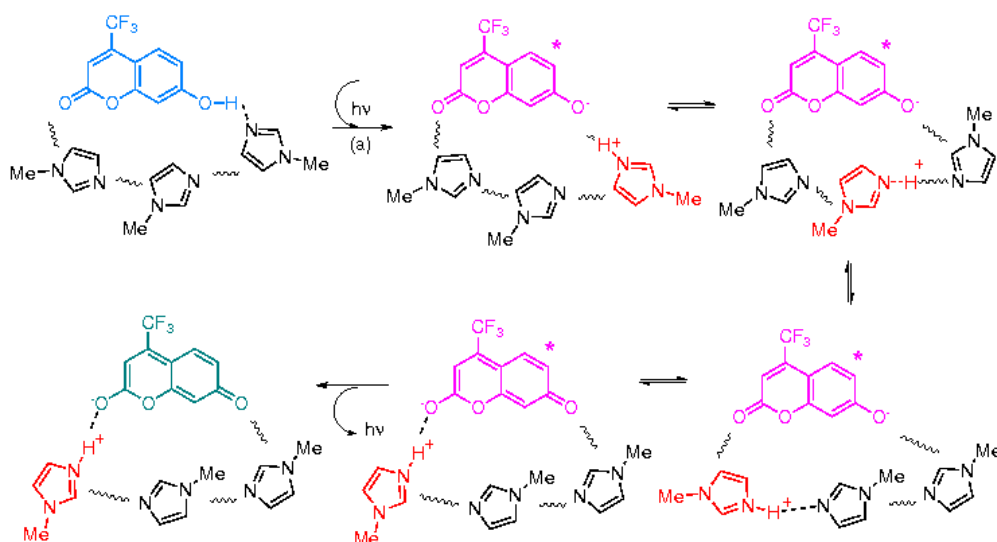


Fig. 3.3: Schematic ES proton transfer (a) and shuttling mechanisms proposed for the reaction occurring between CouOH and 1-MeId at high base concentration in toluene solution. The normal form of coumarin (CouOH) is represented in light blue, its excited anionic form in violet and the tautomeric form (CouOtau-) in light green. Protonated 1-MeId bases are represented in red.

toluene the proton shuttling cannot be attributed to solvent molecules, and experimental evidences support the hypothesis that the mechanism of shuttling involves more than one base molecule and that also does not occur by simple diffusion, it is

reasonable to assume that the shuttled proton is the one transferred from the normal form of the CouOH molecule as schematically depicted in Figure 3.

To this aim, a minimal model able to represent the chain of imidazole molecules responsible for the proton shuttling was defined. Specifically, only three molecules of 1-MeId were explicitly considered since they represent the smallest number of molecules enabling to setup a linear chain which geometrically covers the distance between the two oxygen atoms of coumarin, as schematically depicted in Figure 3. Even if under experimental conditions the ratio CouOH to 1-MeId is much smaller, we can assume that the present chain of base molecules represents, at least, the least energetically favored pathway for proton shuttling. Indeed, in presence of other 1-MeId molecules, energetically less expensive proton transfer pathways may be envisaged so that we can assume that the present model will provide estimation of the maximal energy requested for the proton shuttling.

3.1 Structural and electronic features of neutral and anionic species at the ground and the excited state

Before describing in more details the ESPT mechanism, the electronic and structural features of the different species supposed to be the responsible for the absorption and emission features in absence and in presence of a base will be here briefly summarized. The main structural parameters predicted for the neutral (CouOH and CouOH_{tau}) and anionic (CouO⁻) forms of the coumarin (depicted in Figure efabr-name) both at the ground and the excited state are reported in Table 3.1 while the associated absorption and emission energies are collected in Table 3.2 and Table 3.3, respectively.

The 7-hydroxy-4-(trifluoromethyl)coumarin molecule can exist in two tautomeric forms schematically represented in Figure 6 and, in agreement with experiments, the normal form (here defined as CouOH) is computed to be predominant in toluene since it is predicted to be more stable than the corresponding tautomeric form (CouOH_{tau}) of about 26 kcal/mol. The large energy difference computed between the two tautomers allows to rule out the presence of the CouOH_{tau} in solution at room temperature.

	CouOH		CouOH+1-MeId		CouO⁽⁻⁾+1-MeIdH⁽⁺⁾
	S ₀	S ₁	S ₀	S ₁	S ₁
CO	1.36	1.34	1.34	1.32	1.30
CO _t	1.21	1.23	1.22	1.23	1.23
CC	1.41	1.23	1.41	1.23	1.40
OH	0.97	0.97	1.01	1.08	1.43
O _t H					
NH			1.67	1.48	1.12
ON			2.69	2.55	2.54
θ (°)			1.63	1.93	6.50
	CouOH_{tau}		CouO⁽⁻⁾		CouO_{tau}⁽⁻⁾+1-MeIdH⁽⁺⁾
	S ₀	S ₁	S ₀	S ₁	S ₁
CO	1.24	1.31			1.27
CO _t	1.33	1.34	1.26	1.27	1.27
CC	1.45	1.41	1.23	1.24	1.40
OH			1.43	1.40	
O _t H	0.97	0.97			1.45
NH					1.10
ON					2.55
θ					1.32

Table 3.1: Main structural parameters (Å and degrees), computed for the ground S₀ and excited S₁ states of coumarin and coumarin-base species in toluene. Full cartesian coordinates of minimum energy structures are given as Supporting Information.

	Calculated		Experimental
CouOH	328	(0.4221)	330
CouOH+1-MeId	347	(0.4588)	342
CouOH _{tau}	437	(0.3410)	
CouO ⁻	426	(0.4371)	

Table 3.2: Computed and experimental absorption energies (nm) in toluene. Computed oscillator strengths are given in parenthesis. Experimental values from ref. [6].

	Calculated		Experimental
CouOH	368	(0.3781)	403
CouOH+1-MeId	409	(0.3229)	
CouO ⁽⁻⁾ +1-MeIdH ⁽⁺⁾	454	(0.3067)	460
CouO ⁽⁻⁾	514	(0.2840)	506
CouOH _{tau}	518	(0.2707)	
CouO _{tau} ⁽⁻⁾ +1-MeIdH ⁽⁺⁾	537	(0.2878)	520

Table 3.3: Calculated and experimental emission energies (nm) in toluene solvent. Computed oscillator strengths are given in parenthesis. Experimental values from ref. [6].

Indeed, at the ground state the structural parameters computed for the two tau-tomers are rather similar: the C-O distances of the carbonyl group range from 1.21 to 1.24 Å, while the corresponding C-O distances, involving the hydroxyl oxygens, are computed to be slightly longer 1.36 and 1.33 Å. Both molecules are practically planar as a consequence of the extended π conjugated system and, in presence of a coordinating base, they are lying in the same plane as indicated by the small value for the intermolecular dihedral angle (θ) computed. The anionic form is structurally very similar to the protonated ones although, as expected, the C-O and C-O_{tau} distances tends to equalize (1.26 and 1.23 Å, respectively).

When adding a base molecule coordinating the OH hydrogen atom of CouOH (i.e considering the CouOH+1-MeId system), the C-O distance contracts of 0.02 Å (to 1.34 Å), while the C-O_{tau} elongates to 1.22 Å. This results is due to the formation

of a hydrogen bond between the nitrogen atom of the 1-MeId and hydroxyl hydrogen atom, the O-H distance elongating of 0.04 Å and the corresponding vibration being red-shifted of about 900 cm⁻¹ (from 3811 to 2907 cm⁻¹). Interestingly, at the ground state, a stable minimum corresponding to a hydrogen bonded neutral CouOH is found, that is no spontaneous proton transfer from CouOH to 1-MeId is computed, in agreement with the experimentally known pKa values of CouOH and 1-MeId of 7.26 and 7.4, respectively. On this basis, it is thus possible to rule out a spontaneous proton transfer reaction for the normal form of coumarin at the ground state, consistently to the computed formation of a stable H-bond adduct with short O-H distance (1.01Å with respect to 0.97 Å computed for the isolated CouOH). The stability of this H-bond adduct in H₂O (computed to be 0.9 kcal/mol) is also in line with the experiments since it corresponds to a formation constant of 1071M⁻¹ in good agreement with the measured constant (of 2100M⁻¹). [141] The pKa of the tautomeric form CouOH_{tau} can simply be estimated from the experimental pKa of CouOH (pKa) and the computed CouOH_{tau} to CouOH tautomerization constant in water (K_{tau}) as:

$$pKa_{tau} = pKa + pK_{tau} \quad (3.1)$$

since K_{tau} is related by the acidic constant of the tautomers by:

$$K_{tau} = \frac{k_{a,tau}}{k_a} = \frac{[CouO^-][H^+][CouOH]}{[CouOH_{tau}][CouO^-][H^+]} = \frac{[CouOH]}{[CouOH_{tau}]} \quad (3.2)$$

Considering the relative stabilities of the tautomers computed in water (performed at B3LPY/6-31G(d,p)/PCM level) it turns indeed out that the pKa of CouOH_{tau} should be much lower (roughly 16 units lower) than that of CouOH, in line with the expected strong acidity of this site. Consistently, a stable H-bonded adduct of 1-MeId with CouOH_{tau} cannot be located, since, in agreement with the relative acidity of CouOH_{tau} and 1-MeId a spontaneous deprotonation of the coumarin tautomer is computed.

The vertical excitation energies corresponding to the first, and most intense, electronic transition computed for the neutral and anionic species, are collected in Table 2. The nature of these intense vertical transitions, all corresponding basically to a one electron excitation from the HOMO to the LUMO, can be inferred from the analysis of the orbitals involved and of the associated ground to excited state density difference reported in Figure eprofileGSES. If the transition is clearly of π - π^* type and mainly localized on the π conjugated skeleton, a partial intramolecular CT character (ICT) can be observed, the CF₃ unit acting as an electron acceptor. The CT character can be somehow quantified by the D_{ct} value associated to these vertical transition of 2.231 and 1.415 Å for the CouOH and CouOH_{tau}, respectively. Furthermore, in the case of CouOH a density depletion at the excited state is observed for the hydroxyl oxygen atom thus justifying the increase in acidity at the excited state and overall the possibility, when adding a base, of a proton coupled electron transfer reaction. On the other hand, a slight increase in density at the

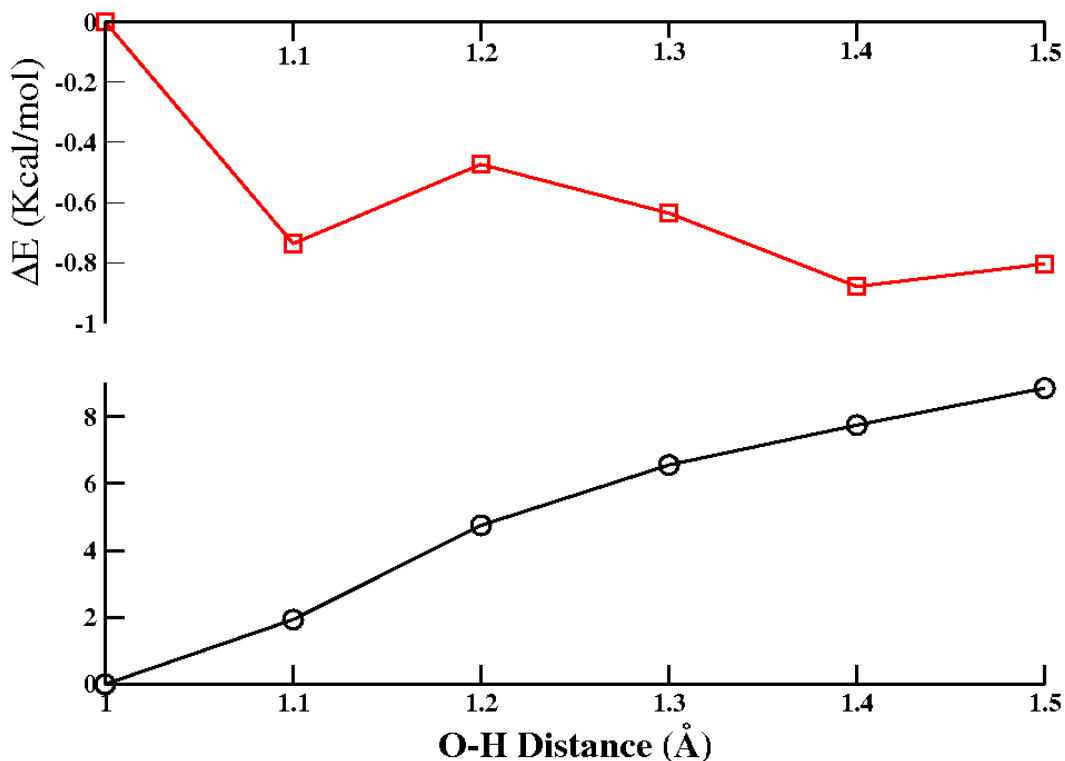


Fig. 3.4: Energetic profiles computed at B3LYP/6-31+G(d,p)/PCM level of theory. Black circle and red square lines correspond to the ground and excited states, respectively.

excited state is computed for the hydroxyl oxygen atom of the $\text{CouOH}_{\text{tau}}$, thus in principle pointing out an expected decrease in acidity of this group at the excited state. From a more quantitative point of view, due to the only partial CT character associated to the vertical excitations, and to the absence of through space character, the absorption energies computed at B3LYP level nicely correlated to the experimental value. Indeed, in toluene the computed absorption energy of the most stable tautomer (CouOH) is 328 nm that very well compares with the experimental absorption maximum recorded, in the same conditions, at 330 nm . [6] On the other hand, for the tautomeric form ($\text{CouOH}_{\text{tau}}$) a transition at 437 nm is predicted which finds

no comparison with steady state absorption spectra reported in Ref. [6]. Therefore, based on both stability and on vertical excitation energies, the presence of this tautomeric species in toluene solution can be safely ruled out. In presence of a base such as 1-MeId, experimentally the absorption is found to be red-shifted to 342 nm [6], as a consequence of the H bond formation and in quantitative agreement with our result predicting an absorption at 347 nm for the CouOH+1-MeId adduct. Therefore, based on the structural, thermodynamical, and vertical absorption data we can conclude that the level of theory used here enables for a quantitative description of the ground and vertical excited state.

Relaxation of the first excited state at TD-DFT level allows obtaining the structural parameters of the three potentially emissive forms, as reported in Table 1. Experimentally, the emission of the neutral form in absence of a base is reported at 403 nm while, in presence of a strong base, the emission of the anionic species is measured at 506 nm. This nicely agrees with the computed values in 3.3 for CouOH and CouO⁻ species of 368 and 514 nm, respectively, while the CouOH_{tau} is predicted to emit at 518 nm. Indeed, considering the two different tautomers, their relative stability in toluene at the excited state is computed to be 0.3 kcal/mol in favor of the CouOH_{tau}. Nonetheless, the CouOH tautomer, more stable in the ground state, is initially excited and it will not be able to tautomerize in absence of a sufficiently high concentration of a base, thus justifying the fact that the emissive species observed will be exclusively the CouOH one.

Consistently to the electronic reorganization upon excitation previously commented and, in particular, to the density depletion occurring at the hydroxyl oxygen atom, at the excited state the CouOH molecule displays a C-O distance 1.34 Å, and an O-H distance 1.23 Å, both of them significantly elongated with respect to the GS structure. The O-H distance on the other hand is rather insensitive to the electronic excitation. Interestingly, a significant shortening of the inter-ring CC bond is also computed (from 1.41 to 1.23 Å) which actually represents the most important structural modification of the coumarin skeleton upon excitation.

When considering the presence of a 1-MeId base molecule, the formation of an H bond adduct red-shifts the calculated emission energies from 368 nm (computed for CuOH in toluene) to 409 nm (computed for CouOH+1-MeId in toluene, Table 3). Nevertheless, although qualitatively in line with the experimentally recorded red-shifted emission in presence of low concentration of 1-MeId, the predicted values are still significantly overestimating the experimental emission measured at 460 nm [6]. Indeed, in presence of a 1-MeId molecule, a ESPT reaction can take place to form the -more stable- emitting species $\text{CouO}^{(-)}+1\text{-MeIdH}^{(+)}$ which is the product of the EPST reaction, as it will be discussed in more detail in the next paragraph. This species is computed to emit at 454 nm in very good agreement with experimental emission recorder at 460 nm [6] and ascribed to the ESPT reaction product at low base concentration.

Finally, it is worth recalling that in presence of a very high concentration of base, the emission is experimentally observed at 520nm. The observed shift in emission energy as a function of the base concentration was experimentally attributed to the formation of the tautomeric species via the shuttling of proton from the normal form through a chain of 1-MeId molecules. Indeed, this chain of PT reactions occurring between base molecules in the first coordination shell of the coumarin allows the formation of the tautomeric form. For these reasons emission from the tautomeric form and base adduct were also computed. The computed emission energies are 518 and 537 nm, respectively, which both very well correlate with the experimental value of 520 nm observed at high concentration of the base. [6]

In conclusion, by comparison of the computed and experimental emission energies, it is possible to clearly identifying the emissive species in toluene as : 1) the CouOH neutral form (in absence of a base), 2) the CouO⁽⁻⁾ anionic form (in presence of a strong base), 3) the CouO⁽⁻⁾+1-MeIdH⁽⁺⁾ (at low 1-MeId concentration), and 4) the CouOH_{tau} and CouO_{tau}⁽⁻⁾+1-MeIdH⁽⁺⁾ at very high 1-MeId concentration and in quantitative agreement with the experimental data and hypothesized relaxation mechanism [6].

As in the case of ground state properties, the level of theory here applied thus enables us for a quantitative recover of the experimental emission spectra in absence and in presence of 1-MeId and moreover supports the experimentally proposed proton transfer mechanism.

3.2 The energetic aspects of the proton transfer event: ground and excited state potential energy landscape

Having proven the accuracy of the level of theory used in quantitatively reproducing the minima on the ground and excited state potential energy surfaces, the same approach was applied to describe the ESPT mechanism at the excited state. As previously explained, a spontaneous proton transfer reaction at the ground state between the coumarin and MeId molecule cannot occur, independently of the tautomeric form considered. In order to understand why a PT reaction can actually occur at the excited state we focused on the analysis of the reactivity of the CouOH form in presence of one 1-MeId molecule. The reactants and the product of the PT reaction at the excited state have been already discussed in the previous section since they actually correspond to the H bond adduct CouOH+1-MeId and to the CouO⁽⁻⁾+1-MeIdH⁽⁺⁾ complex, respectively. In order to get a first flavor of the potential energy surface associated to the PT reaction, a constrained potential energy profile following an ad-hoc defined reaction coordinate was computed on the excited electronic state. In particular, in order to follow the proton transfer from the CouOH to the nitrogen atom of the 1-MeId base, the O-H distance was scanned in the 1.00-1.50 Å range while relaxing all other degrees of freedom. The main geometrical parameters obtained for the different points of the PT profiles are reported in the Supporting Information while efgidenergy are reported the corresponding

relaxed potential energy profiles computed at the excited state and, vertically, at the ground state. In both cases the energy of the first point, corresponding to the CouOH+1-MeId adduct optimized at the excited state, was set to zero. In Figure 5.10 are reported the corresponding relaxed potential energy profiles computed at the excited state and, vertically, at the ground state. In both cases the energy of the first point, corresponding to the CouOH+1-MeId adduct optimized at the excited state, was set to zero. From these two relative energy profiles it is evident

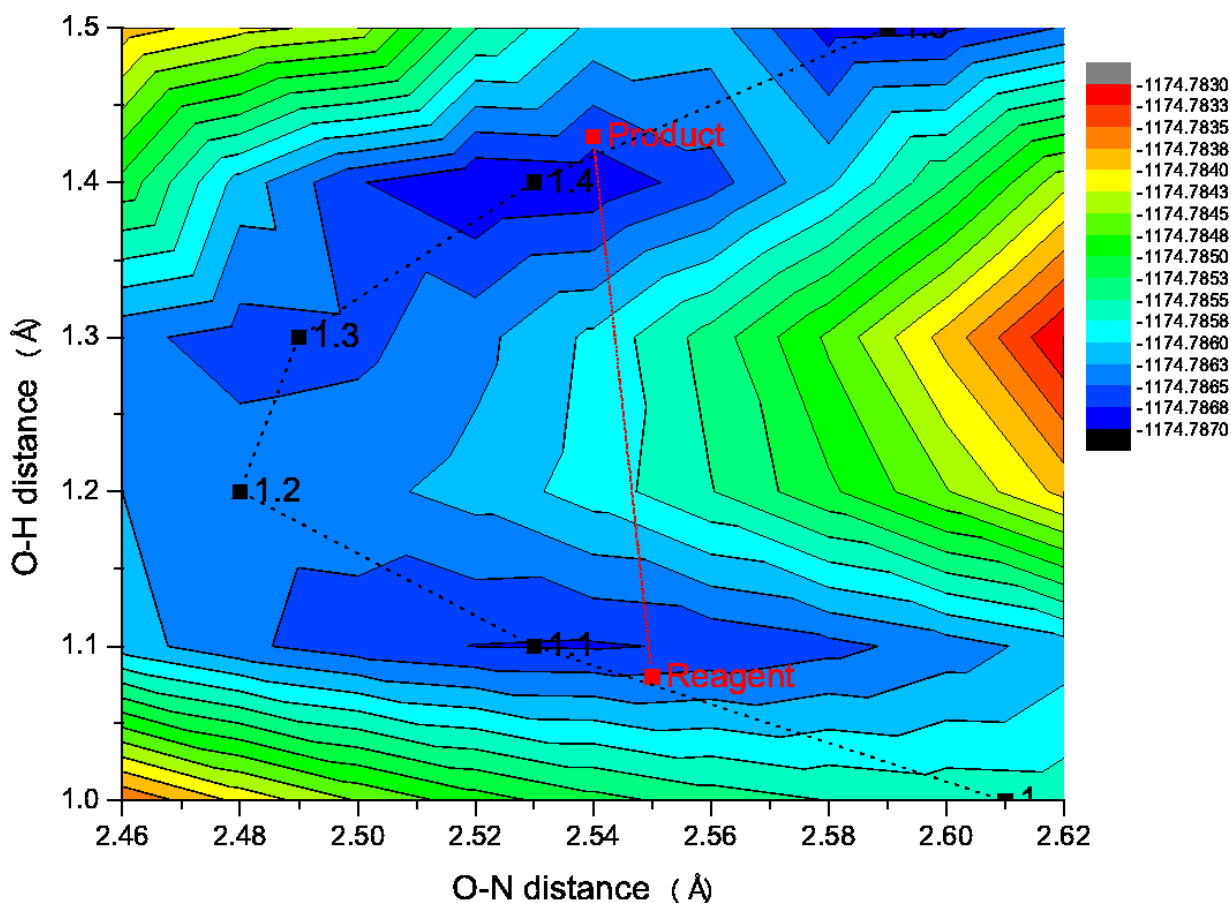


Fig. 3.5: Potential energy surface computed for the first excited state (S_1) for the CouOH+1-MeId system in solution. Red circles correspond to fully relaxed structure (reactants and products). Black squares correspond to structures obtained by relaxing all structural parameters except the O-H distance.

that at the ground state the proton transfer does not spontaneously occur with a monotonic energy increase as a function of the O-H distance of about 9 kcal/mol. On the other hand, at the excited state two stable states corresponding to the H bonded CouOH+1-MeId adduct and to the CouO⁽⁻⁾+1-MeIdH⁽⁺⁾ product, are indeed found. This profile clearly illustrates the possibility of getting a PT reaction at the excited state. Furthermore, the ESPT product (CouO⁽⁻⁾+1-MeIdH⁽⁺⁾) is found to lie roughly 0.1 kcal/mol lower in energy with respect to the H bonded adduct with a barrier of only 0.3 kcal/mol thus providing evidence for a spontaneous PT at the excited state.

This finding is also consistent with the increase in acidity of CouOH at the excited state that has already been qualitatively justified by a density depletion occurring under excitation at the hydroxyl oxygen atom. More quantitatively, the variation of the pK_a from the ground to the excited state can be estimated, under the assumption of Förster model which should hold in the present case but not necessarily for every system [142], from the computed absorption (or emission) vertical energies.

Thus absolute pK_a^* values can be computed from experimental ground state pK_a as follows: [143, 144]

$$pK_a^* = pK_a + \frac{\Delta E_i}{RT \ln(10)} \quad (3.3)$$

$$pK_{a,tau}^* = pK_{a,tau} + \frac{\Delta E_{i,taut}}{RT \ln(10)} = pK_{tau} + pK_a + \frac{\Delta E_{i,tau}}{RT \ln(10)} \quad (3.4)$$

where ΔE_i (i=abs or emi) are the differences in vertical absorption or emission

energies computed between the neutral (CouOH or CouOH_{tau}) and anionic (CouO⁻) species and K_{tau} is the tautomerization constant defined in equation 3.2.

Using these relations an increase in acidity of -14.7/-16.1 pK units is computed for CouOH considering absorption or emission energies of Tables 3.2 and 3.3, respectively. The pK of CouOH_{tau}, on the other hand, is hardly affected and actually predicted only to slightly increase (of 1.2 and 0.3 pK units, respectively). Thus, while at the ground state the CouOH molecule is a very weak acid, at the excited state it is computed to behave like a strong acid with a pKa* in the order of -7.4 to -8.9 thus justifying the spontaneous ESPT reaction observed. On the other hand, although still extremely acid, the CouOH_{tau} form is predicted to become slightly more basic at the excited state, behavior that play a role in presence of a excess of 1-MeId molecules.

From a mechanistic point of view, more carefully analyzing the structures computed at the excited state for each constrained O-H distance, it can be observed that the O-N distance is minimal at the maximum in the energetic profile of Figure 5.10.

It is therefore reasonable to assume that a reaction coordinate for the ESPT would hardly be defined by the variation of a single molecular parameter, but it is probably better described by a simultaneous variation of the OH and O-N distances. This is analog to what happens in the ground electronic state, where it is well established that the acceptor and the donor atoms move closer in a concerted way to facilitate the proton transfer event. [145–147]

Thus, a better understanding of how the proton transfer relates to the relaxation of the electronic density necessarily includes a scan at least over both the O-H and O-N distances on the excited state potential energy surface. To this end a 2D grid of energy points was constructed scanning both the O-H distance (from 1.00 to 1.50 Å) and the O-N distance (from 2.46 to 2.62 Å).

For each point of this grid, all other structural parameters were fully relaxed. The obtained PES is reported in Figure 3.5, together with the position of the fully relaxed reactant and product. From this plot it is rather clear that at least two different reactions pathways are possible for the ESPT reaction.

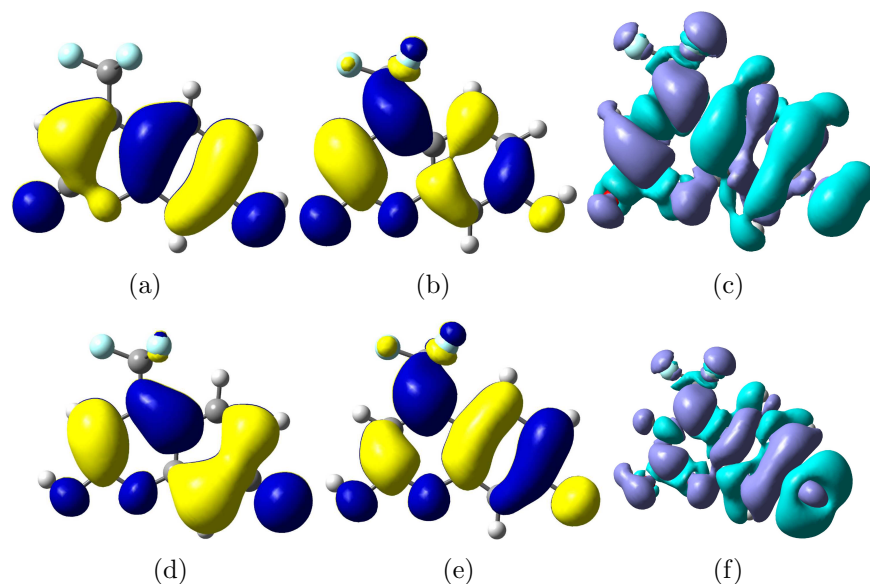


Fig. 3.6: Ground state HOMO (a,d) and LUMO (b,e) contours computed for CouOH (up) and CouOH_{tau} (down) together with the corresponding density difference (c,f) associated to the first vertical transition. Positive and negative variations of the density are represented in dark and light blue, respectively.

The most favorable (1) possessing the lowest barrier (of ca 0.4 kcal/mol) corresponding to what already described on the 1D profile that is the combined contrac-

tion of the O-N distance (up to 2.48 Å) and elongation of the O-H distance, and (2) an energetically allowed one having a slightly higher barrier (of 0.6 kcal/mol) which basically corresponds to a proton transfer at fixed O-N distance.

3.3 Analysis of density based indices: D_{CT} and $D_{CT,react}$

As described in the previous subsection, the ESPT reaction in CouOH-1-MeId system is characterized by a smooth energy surface as can be expected for a reaction which spontaneously occurs and for which very low reaction barriers are computed. Furthermore, two degrees of freedom, namely the O-H and O-N distances, undergo significant variations along the possible reactions paths, eventually in a concerted (coupled) way. However, the electron density redistribution upon electronic excitations does not exclusively take place on the atoms involved into PT (that is on H, N and O atoms) but also strongly involves the whole coumarin skeleton, as evident from the different density charts depicted in Figure *efprofileGSES*.

In other words, structural reorganization and CT do not necessarily affect the same part of the molecule so that a metric recovering both the structural and the electronic reorganization would be ideally needed to correctly describe the ESPT reactions. In this sense it is interesting to analyze if density based indices can provide such a description helping in identifying stationary points on the PES or even possible reaction paths.

As matter of fact, the transition state of the ESPT reaction represents the max-

imal charge separation that can be attained before the proton will transfer. Being the reaction triggered by a strong electronic rearrangement of the hydroxyl oxygen atom upon the excitation, we can reasonably expect that the transition state is also characterized by a maximum of the vertical charge transfer length D_{CT} .

This intuitive picture is confirmed and quantified by the calculation of D_{CT} index over the 2D grid previously defined, as reported in Figure 3.7(a).

Exploring the 2D D_{CT} surface as a function of the O-H and the O-N distances and following the 1D O-H reaction profile it is indeed possible to show that initially the CT length increases (larger D_{CT}) up to, basically, the transition state (located in the region of O-H and O-N distances equal to 1.2 and 2.48 Å, respectively) where it reaches its absolute maximum value. After the proton is released to the base, the D_{CT} monotonically decays to the value computed for the product.

Although the variation of the D_{CT} going from the reactants (2.268 Å) to the products (2.229 Å) is small (0.039 Å), it is interesting to note how the transition states associated to both the minimal energy path (corresponding to a simultaneous O-H and O-N variation) and to a proton transfer occurring at constant O-N distance always correspond to maxima using a D_{CT} metrics. In particular, the maximal D_{CT} value is associated to the TS corresponding to the minimal energy reaction path. Thus, the original D_{CT} index, taking into account only the variation of the electronic density associated to a vertical CT transition, is indeed able to identify the region where the TS is located. Nonetheless, the evolution of this index over the coordinate

space seems unsuitable to define the preferential reaction path at the excited state.

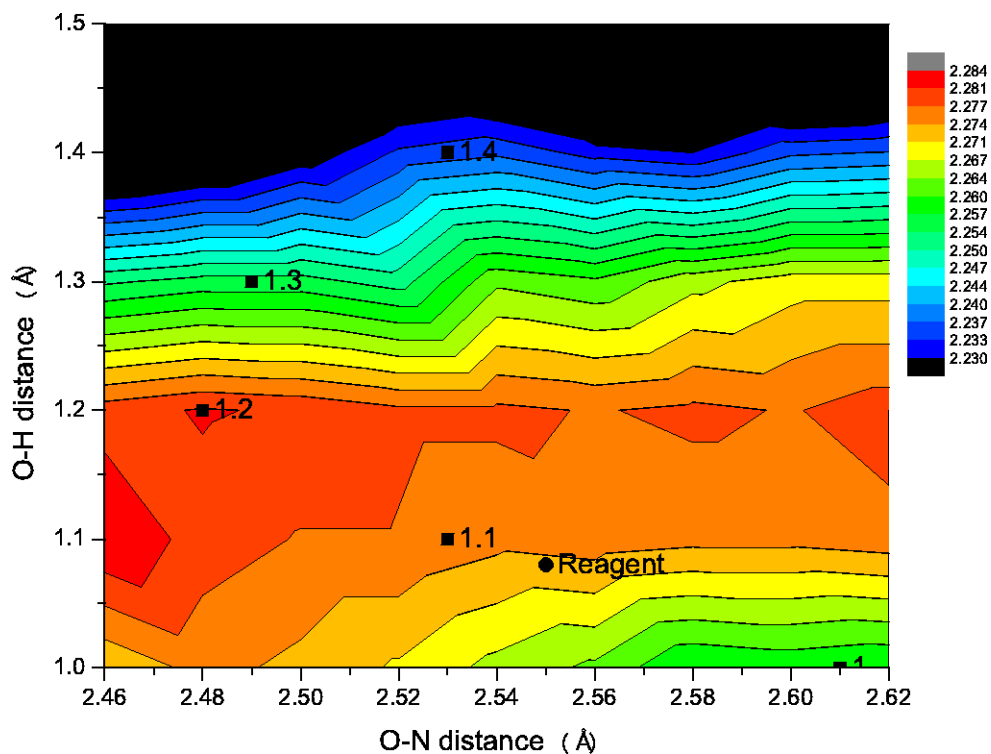
In order to include the effect of nuclear relaxation directly in our description, we thus decided to consider the new index ($D_{CT,react}$), introduced in Section 1.4. $D_{CT,react}$ describes indeed the variation associated to electronic and geometrical structure going from the ground state electronic configuration (computed at the ES reactants' geometry) to a given point in coordinate space on the PES.

The computed $D_{CT,react}$ values, reported in Figure 3.7, overall show how going from the reactants to the product, the $D_{CT,react}$ decreases. Carefully analyzing the most significant region, that is the one close to the reagent (here defined by O-H and O-N distances in the 2.52-2.58 Å and 1.0-1.2 Å range, respectively), we notice that the H transfer minimum energy paths of Figure 3.5 are here mirrored by paths that tend to reduce the $D_{CT,react}$.

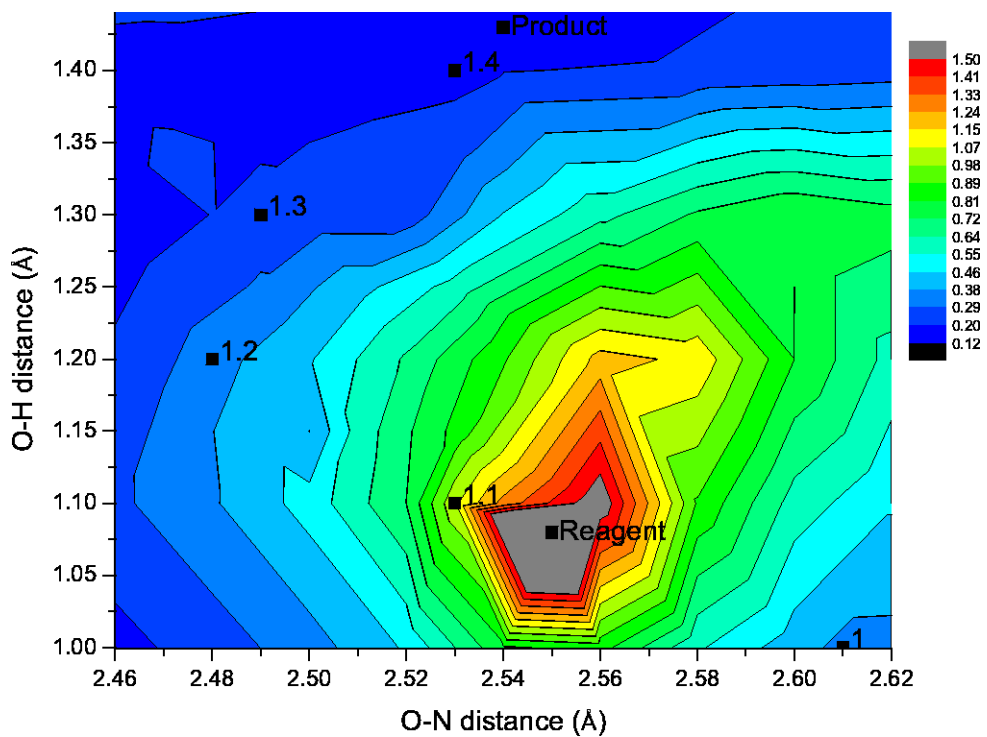
Remarkably, the most favorable route from the energetical point of view corresponds to the steepest variation of the $D_{CT,react}$, that is the one involving a combined shortening of the O-N distance (corresponding to a formation of the stable H bond adduct) and an elongation of the O-H distance (resulting of the different acidic strength of the sites).

For example, let us consider the hypothetical reaction path involving the increase of the O-H distance only, keeping the O-N distance fixed at the value of the reactant (O-N=2.55 Å, i.e. the shortest path). In this case, $D_{CT,react}$ decreases up to the product with variations of 1.00, 1.39, 1.78 Å at O-H values of 1.10, 1.20,

1.30 Å , respectively. When we compare this to the path suggested by the energy surface, i.e. including the O-N component into the reaction coordinate, we observe $D_{CT,react}$ variations of 1.22, 1.92, 2.02 Å respectively, at the same values of O-H distances. In this case, the $D_{CT,react}$ of the product is smaller. In other words, the O-N shortening allows for a steepest decreasing of $D_{CT,react}$. In conclusion, from the combined analysis of density based indices it is possible to locate the most favorable reaction channel over a ESPT surface (minimal energy TS) and to identify possible competing mechanisms when associated PES are very flat and hardly allows for a fine description of the mechanism based on the sole energetic criteria. These findings open a new scenario in the modeling of photo-induced reactions, for which electronic density based indices can be used as effective reaction coordinates.



(a)



(b)

Fig. 3.7: D_{CT} (\AA , upper panel) and $D_{CT,react}$ (\AA , lower panel) surfaces computed for CouOH+MeId in toluene solution.

3.4 A proton shuttle for the phototautomerism

The normal form of the coumarin molecule at the ground state was found to be 26 kcal/mol more stable than its tautomeric form. In presence of base molecules, the normal form (CouOH-(1-MeId)₃, 1 in Figure 3.4) is still predicted to be largely more stable (of roughly 17 kcal/mol) with respect to the tautomeric form (CouOH_{tau}-(1-MeId)₃) thus confirming that, at the ground state, even in presence of an excess of base the only species present in toluene solution is predicted to be the CouOH-1-MeId adduct in agreement with experimental data. [6] Interestingly, the introduction of further base molecules in the model does not sizably affect the H-bonding to the coumarin molecule at the ground state. Indeed, comparing the OH and NH distances computed for the CouOH-(1-MeId)₃ (1.02 Å and 1.63 Å) and CouOH-1-MeId (1.01 Å and 1.67 Å) adducts differences of maximum 0.04 Å can be found. The only relevant difference is that, contrary to what happens in a 1:1 adduct, in the CouOH-(1-MeId)₃ one the coordinated base molecule is no longer coplanar with the coumarin, due to the interaction with the next 1-MeId molecule in the base chain, with a tilt angle with respect to the CouOH plane of roughly 30°. Indeed, at the ground state, in absence of a proton transferred to the bases chain, the neutral base to base interactions are relatively weak of the order of 6 kcal/mol so that the leading interaction is still represented by the H-bond to the coumarin molecule which is computed to be 19.6 kcal/mol. Not surprisingly, the absorption maximum computed for the CouOH-(1-MeId)₃ model (at 354 nm) not only very well compares

with the value experimentally recorded for CouOH in presence of 1-MeId in toluene (342 nm) but it is also very similar to what previously computed for the CouOH-1-MeId adduct (347 nm). In other words, the red-shift experimentally observed when adding 1-MeId to a toluene solution of CouOH has to be ascribed to the formation of an H-bond between the CouOH and 1-MeId but it is insensible to the overall base concentration, that is not quantitatively enhanced by the involvement of the 1-MeId in a base network, which is also in good agreement with the experimental data. Relaxation of the excited state of the CouOH-(1-MeId)₃ adduct yields, as expected,

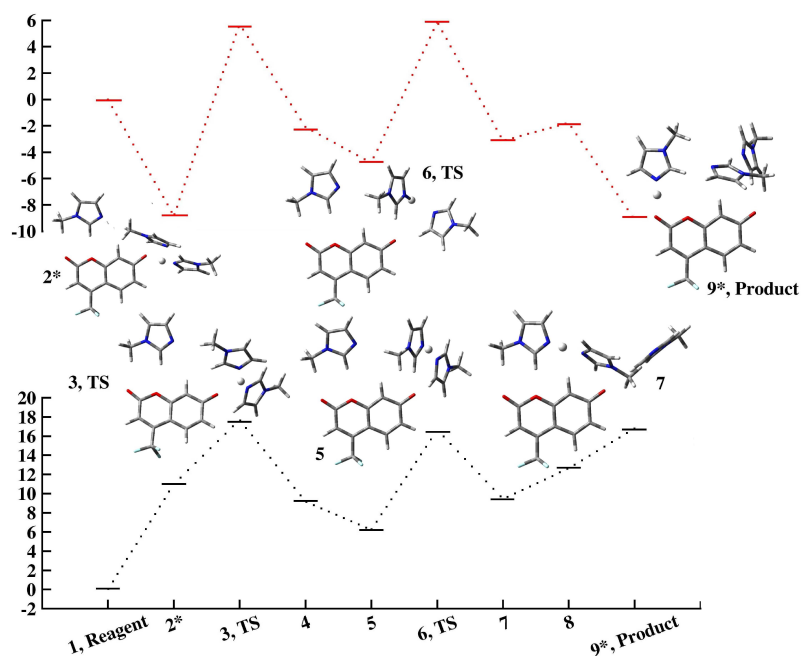


Fig. 3.8: Computed Proton Transfer (1 to 2) and Proton Shuttling (2* to 9*) ground (bottom) and excited (upper) state potential energy profiles. GS and ES relative energy (in kcal/mol, reagents energy set to zero) in different scales for the sake of clarity.

a proton transfer to the 1-MeId base molecule and the formation of the [CouO]⁻-(1-MeIdH)+(1-MeIdH)₂ adduct (2* in Figure 3.4), the product of the ESPT reaction

and the starting point for the proton shuttling mechanism depicted in Figure 3. Analysis of the structural features of this adduct shows OH and HN distances (1.53 and 1.08 Å) in qualitative agreement with the results obtained with the model containing only one base molecule (1.43 and 1.12 Å) although a slightly larger OH distance is found. A slight planarization (variation of about 5° with respect to the ground state value) of the tilt angle between the coumarin and the base is also computed. Emission from this relaxed excited state (2* in Figure 3.4) is computed at 470 nm in very good agreement with the value experimentally observed at low base concentration at 460 nm, [6] and slightly red-shifted with respect to what computed with a single base molecule model (454 nm). Indeed, the ground state energy of the CouO-(1-MeIdH)+ (1-MeIdH)₂ adduct, vertically computed from the 2* geometry, lies 11.0 kcal/mol higher than the CouOH-(1-MeIdH)₃ reactant, ruling out the possibility of a spontaneous PT at the GS (Figure 3.4). At the excited state, on the contrary, the [CouO-]*-(1-MeIdH)+ (1-MeIdH)₂ adduct is stabilized of -8.8 kcal/mol, in agreement with the well characterized photoacidity of the CouOH molecule. Inspection of frontier orbitals involved in the excitation (Figure 3.4) shows that the electronic transition involves only a reorganization of the electronic density of the CouOH molecule with a density depletion occurring on the hydroxyl moiety responsible of the photoacidity of the molecule and of the favorable deprotonation, while the imidazole bases are not directly involved in the transitions. Starting from structure 2*, that is the excited state relaxed structure corresponding to the PT

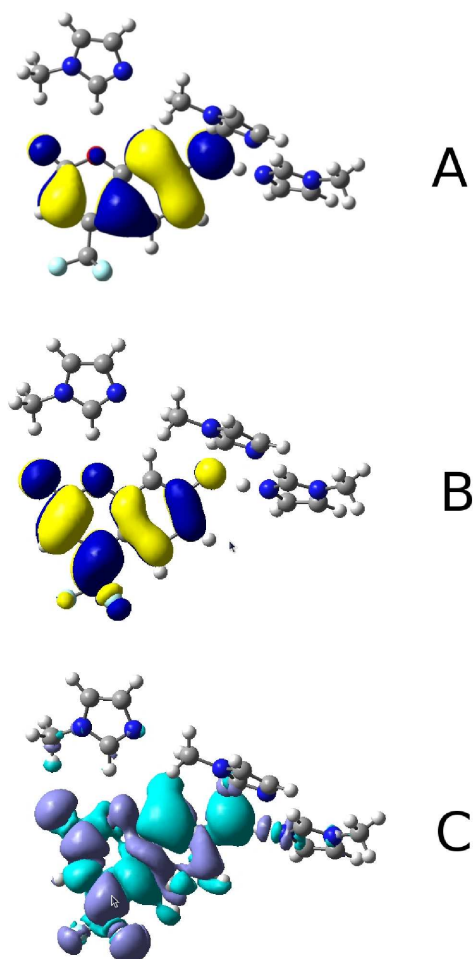


Fig. 3.9: Contours of HOMO (A), LUMO (B), and difference in electronic density (C) involved in the initiating ESPT in the $[\text{CouO-}]^*-(1\text{-MeIdH})+(1\text{-MeIdH})_2$ adduct. Spatial orientation of the coumarin molecule is analog to structures shown in Figure 3.4.

from the coumarin to the first base molecule (here after 1-MeIdA), the geometry optimizations needed to fully characterize the elementary steps in the transport process have been performed considering the coumarin molecule in its ground state, in order to simplify and speed up the calculations. The excited state profile has thus been constructed by vertically computing the energy of the first excited state on the obtained ground state geometries. Only when the proton is back transferred

to the tautomeric form of the coumarin (that is for the emitting tautomeric species, 9*), the structural features were computed considering the coumarin in its excited state, in order to correctly take into account the change in basicity/acidity of the tautomeric OH group at the excited state. For this point, the ground state energy has been computed vertically from the excited state optimized geometry. Such an optimization procedure allows for obtaining a reasonable picture of the ES profile, enabling to locate also transition states. As matter of fact it corresponds, in first approximation, to consider that the change in electronic structure upon excitation, localized on the coumarin molecule and responsible for the initial ESPT reaction, will not affect strongly the inter imidazoles proton transfer reactions (here represented by the intermediate and transition states from 3,TS to 8). This assumption is partially justified by the fact that the PT barriers related to the transfer between two imidazole molecules are not very sensitive to the electronic structure of the coumarin (i.e. to the fact that this molecule is computed in its ground or excited electronic state). Indeed, the barrier corresponding to the transfer from 1-MeIdA to 1-MeIdB (i.e. the central one in the base chain), associated to the conversion of species 5 to 7, is practically identical on the GS (black line, Figure 3.4) and ES (red line, Figure 3.4) profiles, as also reported in Table 3.4. Furthermore, the base to base interaction when the proton has been transferred to the chain significantly increases, and is estimated between 26 and 56 kcal/mol, thus representing the leading interaction in the activated proton chain.

	GS B3LYP	ES/TD-B3LYP	ES/TD-CAM-B3LYP
1	0.0	0.0	0.0
2*	11.0	-8.8	-5.4(-8.1) ^a
3	17.7	5.7	4.1
4	9.2	-2.1	-2.8
5	6.2	-4.8	-5.7
6	16.7	5.9	5.2
7	9.4	-3.1	-4.9
8	12.7	-1.8	-3.8
9	16.8	-9.1	-7.7(-9.8) ^a

* values refer to structure optimized at the TD-B3LYP/6-31+G(d,p) level of theory. a values refer to structure optimized at the TD-CAM-B3LYP/6-31+G(d,p) level of theory.

Table 3.4: Relative energies of all species (in kcal/mol) computed at the ground (GS) and (ES) excited state at B3LYP and CAM-B3LYP level.

Overall inspection of Table 3.4 and of Figure 3.4, clearly shows that tautomerization reaction at the ground state is thermodynamically unfavorable (endo-ergonic), the product of the tautomerization reaction, CouOHTau-(1-MeId)₃, lying 16.8 kcal/mol above the reagents. Furthermore, beside the unfavorable initiating proton transfer from the coumarin to the first imidazole (of 11.0 kcal/mol), the transition state associated to the proton transfer from this latter base molecule to the second (3,TS) is computed to be roughly 7 kcal/mol higher in energy. Overall, the initial steps of the PT reaction thus appear extremely unfavorable. On the other hand, at the ES the stabilization of the ESPT product from the coumarin to the base (compound 2*), computed to be -8.8 kcal/mol, determines that all the stable intermediates of the proton shuttling reactions are lying below the reactant energy (1), and that relevant transition states (3,TS and 6,TS) are only few kcal/mol higher (in all cases less

than 6 kcal/mol). Therefore, the favorable thermodynamic balance of the reaction is indeed due from one side to the photoacidity of the normal form of CouOH, leading to the formation of the stable ESPT initial product, and to the slightly larger stability of the coumarin tautomer adduct (9* of ca 1 kcal/mol more stable than 2*) at the excited state. While the neutral tautomeric form of the CouOH, CouOHTau-(1-MeId)₃, at the ES shows OtauH and HN distances which are 1.56 and 1.07 Å, respectively, the final product of the proton shuttling (9*) presents both OH and ON distances that better fit to an adduct of CouOtau-(1-MeIdH⁺)(1-MeId)₂ type, in agreement with the very negative acidic constant computed for the tautomer in the previous Chapter. Emission of this species is computed in quantitative agreement with the experimental value (522 nm computed with respect to 520 nm experimentally measured [6]) thus somehow confirming the nature of product as a coumarin tautomer to protonated base adduct. Noteworthy, this overall picture of the proton shuttling does not qualitatively change when range separated hybrids (such as CAM-B3LYP) are used to describe the ES potential energy profile, though the stabilization of the tautomer product appears more marked (Table 3.4).

In summary, here a general protocol for the characterization of an intermolecular excited state proton shuttling reaction based on DFT and TD-DFT is presented and validated. As results, the tautomerism of 7-hydroxy-4-(trifluoromethyl)coumarin is found to be activated only in the excited state, as previously experimentally hypothesized only on the basis of emission bands assignment. From a mechanistic

point of view, results clearly show that the overall driving force of the entire shuttling remains the coumarin photoacidity, which is responsible both of the first proton transfer event and of the strengthening of the following chain mechanism of base to base proton hopping.

Chapter 4

Proton coupled electron transfer reactions

Undoubtedly proton coupled electron transfer reactions (PCET) play a major role in many systems of biological relevance, including, for instance, those responsible for nitrogen or oxygen fixation. [148–150] Analogously, they are also essential mechanisms for many redox processes occurring in synthetic reactions [150–152]. Not surprisingly great efforts have been devoted to better understand and model the elementary steps of PCET processes from both an experimental and a theoretical point of view [133,153–158]. A PCET can occur either as an asynchronous (not concerted) proton and electron (or electron and proton) transfer or as a synchronous mechanism. Indeed, the discrimination between a sequential or a concerted mechanism is far to be trivial for both experiment and theory. [159–161] Many related aspects play a crucial rule in determining the kinetic and thermodynamic properties of the PCET event. Extremely important are both the properties of the donor (D) and acceptor (A), (such as redox potential E and pK_a [162]) and the conformation of

the peptide bridge binding them. [163] From a theoretical point of view there is also the additional challenge to find effective models for the description of such delicate processes. Very recently, the group of B. Giese developed a peptide system [164,165] (Figure 4.1) in which intramolecular ET takes place between a C-terminal dialkoxy phenylalanine radical cation as electron acceptor, and an N-terminal neutral tyrosine as electron donor. In the middle between donor and acceptor an amino acid

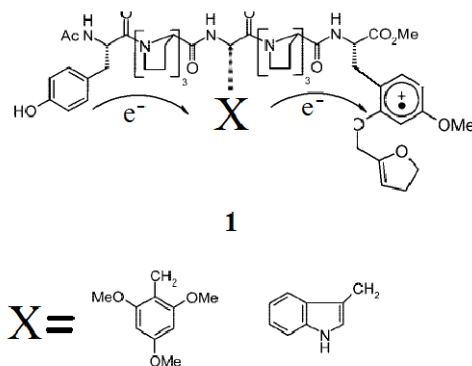


Fig. 4.1: Model peptide for the investigation of intramolecular ET with X as side chain of an amino acid that is used as relay station. Figure from ref. [9].

with natural or artificial side chain X was introduced, and these three amino acids were separated from each other by proline bridges enforcing a polyproline II (PPII) helical structure. [164] The ET between the two terminal amino acid side chains of the peptide is strongly dependent on the nature of the bridging amino acid X. [9] In particular really interesting are results experimentally obtained with tryptophan and 2,4,6-trimethoxyphenylalanine as X amino acid. Indeed, trimethoxyphenylalanine leads to a 30% of oxidized tyrosyl radical while only 10% of yield is obtained

with the tryptophan amino acid. [9,166]

4.1 A model for PCET in oligopeptides

Looking at the last step of the entire ET process (Figure 4.1), we considered the study of a model peptide involving only the tyrosine, the triproline bridge and X amino acid. In order to reduce the size of the system, the triproline bridge was substituted with three glycine amino acids blocked in a PPII helix conformation. In the analysis two different systems were considered: *Tyrosine–Glycine–Glycine–Glycine–2,4,6–Trimethoxyphenylalanine* ($YGGGF_{TRM}^{\bullet+}$), and *Tyrosine–Glycine–Glycine–Glycine–Tryptophan* ($YGGGW^{\bullet+}$), both treated in the form radical cations. In order to study the micro solvation effects of the tyrosine (PCET donor residue) on the PCET process, we considered several peptide - water clusters, including three (α cluster), four (β cluster), five (γ cluster) and six (δ cluster) water molecules, respectively. The statistic weight of these peptide-waters cluster has been examined through an ONIOM/ADMP molecular dynamic simulation. [147] The theoretical analysis provided significant insight into the surrounding medium effects on the energetics of the PCET reaction, showing how the microsolvation structures can affect the energy of electronic states involved in the process. The results also rationalize the observed experimental trends.

The four clusters build up to represent different tyrosine microsolvations are reported in Fig. 4.2. In the α cluster (fig. 4.2(a)) the tyrosine microsolvation is represented by three water molecules arranged in an *eigen*-like structure. By

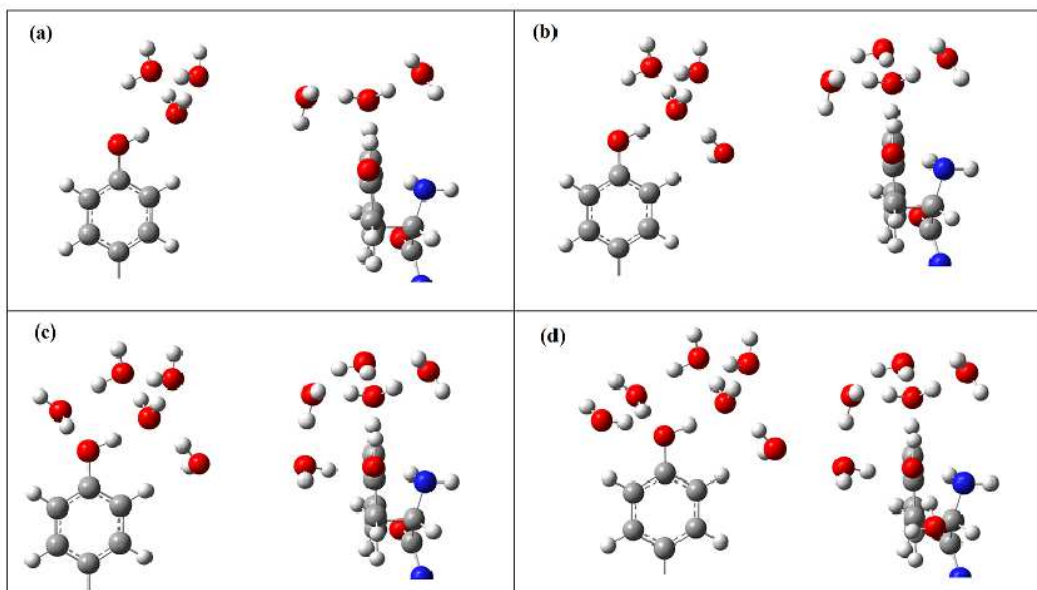


Fig. 4.2: $[YGGGF_{TRM}(H_2O)_n]^{\bullet+}$ clusters:(a) cluster α ; (b) cluster β ;(c) cluster γ ; (d) cluster δ .

adding further water molecules to complete the first solvation sphere of the acceptor water, the β cluster is obtained while saturating the tyrosine solvation sites give us the δ and γ arrangements.

This allowed to effectively assess the impact of the micro-solvation on the PCET reaction. Note that, the tyrosine is solvated only by the proton acceptor water, in the α and β clusters, while one and two water molecules act as hydrogen bonds donor (HBD) in the γ and δ clusters, respectively.

A constrained potential energy profile following an *ad-hoc* defined reaction coordinate was computed on α , β , γ and δ clusters, in order to follow the proton transfer from tyrosine oxygen (O_{tyr}).

The distance was scanned in the 1.00-1.60 Å range while relaxing all other degrees of freedom, and maintaining a constraint on the angles ϕ and ψ of the

polypeptide backbone ($\phi = -75^\circ$ and $\psi = 145^\circ$) to preserve the PPII helix conformation. [167]

In order to follow the ET process, the Mulliken spin densities (SD) on each residue of the peptide along the PT coordinates were monitored. According to this assumption, the ET reactant state corresponds to a SD=1 on the trimethoxyphenylalanine residue (radical form) and SD=0 on the tyrosine (closed shell form). On the contrary, the ET product is characterized by a SD=0 on the trimethoxyphenylalanine residue (closed shell form) and SD=1 for the tyrosyl radical.

To gain information on the tyrosine microsolvation the potential energy surface of the system under study has been explored through ab-initio molecular dynamics. Due to the high computational cost of the ONIOM/ADMP simulation [147] required for the target system a preliminary analysis has been conducted on the microsolvation of a phenol molecule. This can be considered representative of the reactant state solvation in which neither the electron nor the proton have been transferred yet. An ab-initio trajectory for a total period of 10 ps with a time step of 0.2 fs have been collected. In particular, the phenol ring has been solvated with 304 water molecules (covering about four solvent shells) and kept at the center of a sphere with radius of 13 Å.

The full QM level (B3LYP/6-31G(d,p)) was adopted for the phenol molecule, whereas the remaining explicit solvent molecules have been described at MM level using the TIP3P water model. [168] Furthermore, non periodic boundary condition

has been employed using a nonperiodic ab initio dynamics model, namely, the general liquid optimized boundary (GLOB). [169–171]

The collected trajectories have been analysed evaluating the radial distribution function of the hydroxyl group and the variation with time of the hydrogen bond number.

4.2 2,4,6-trimethoxyphenylalanine as electron acceptor

In fig. 4.3 energy profiles along the PT coordinate are reported for clusters α , β , γ , and δ . In order to indicate the diabatic state of reference, red lines refer to a situation in which the unpaired electron can be localized on the trimethoxyphenylalanine residue, while blue ones refer to situations in which the radical can be attributed to the tyrosine residue. Analysis of the energetic profile of cluster α , reveals that the

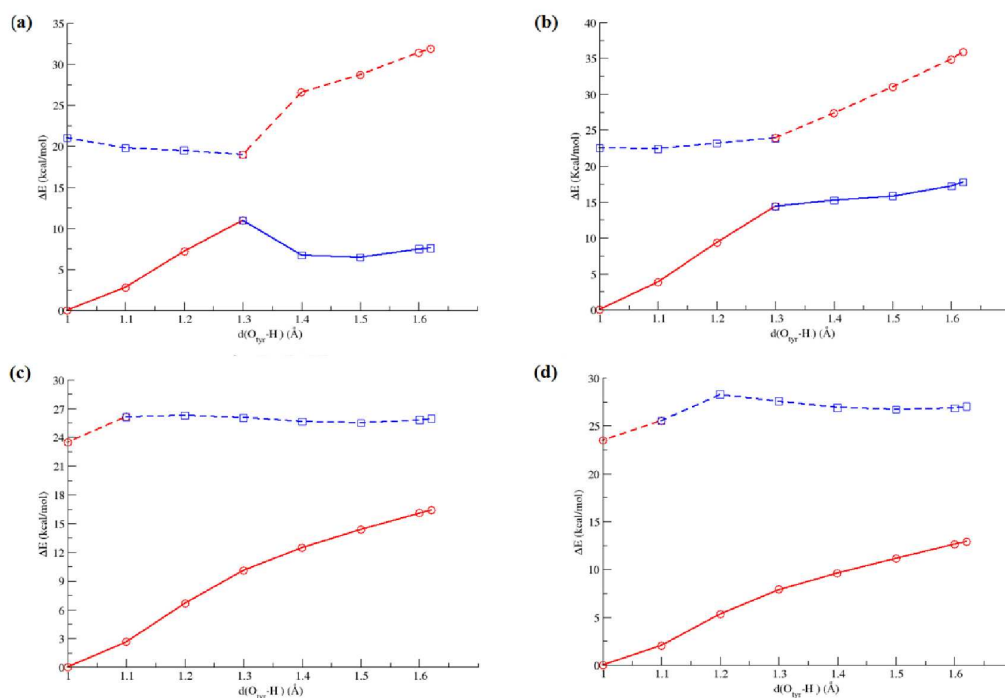


Fig. 4.3: Energetics profiles:(a)cluster α ; (b)cluster β ;(c) cluster γ ; (d) cluster δ . Solid and dashed lines represent the ground state and first excited state adiabatic potential energy surface respectively. In the red and blue lines the radical is respectively localized on trimethoxyphenylalanine or tyrosine residue.

electron transfer occurs at the ground state. More closely, the electron is transferred when the distance $O_{tyr} - H$ is close to the value of 1.403 \AA . However, this dis-

tance should be considered as only indicative, because electrons and protons behave quantum mechanically and hence can not be localized to a single point at any given time.

The energy barrier for the process is about 10 kcal/mol, although it could be still lowered considering the Zero Point Vibrational Energy (ZPVE).

As it can be inferred from Figure 4.3(a) the two adiabatic PESs are quite separated with a minimum energy difference of 8 kcal/mol (0.347 eV) occurring at the maximum of the ground state PES.

Analysis of spin densities localization revealed that the two electronic states (adiabatic states) are well described in terms of two diabatic ones. One of these, that is to say the reactant one, corresponds to the situation in which the electron and proton are located on the tyrosine residue. The other one (product state), represents the situation where the electron is on the trimethoxy residue, and the proton is transferred on the acceptor water.

This picture remains unchanged in the case of the β cluster (see Figure 4.3(b)). However, in this case the energy surfaces are more flat and the energy barrier is higher than in the α cluster. Regarding to γ and δ clusters, it is worthy to note that within these microsolvation structures the ET event doesn't take place on the ground state.

The analysis of the Mulliken charges (Figure 4.4) revealed that, when the solvation of tyrosine is represented by the cluster δ , the formation of the phenolate

resulted to be stabilized with respect to the phenoxide. As it can be inferred from analysis of Figure 4.4 this situation corresponds to stabilize a zwitterionic state with a net positive charge on trimethoxy residue, a net negative charge on tyrosine one and finally a net positive charge on the hydronium ion. From this point of view the water molecules labeled as W5 and W6 energetically favor the formation of the ion pair between the tyrosine anion and the hydronium ion.

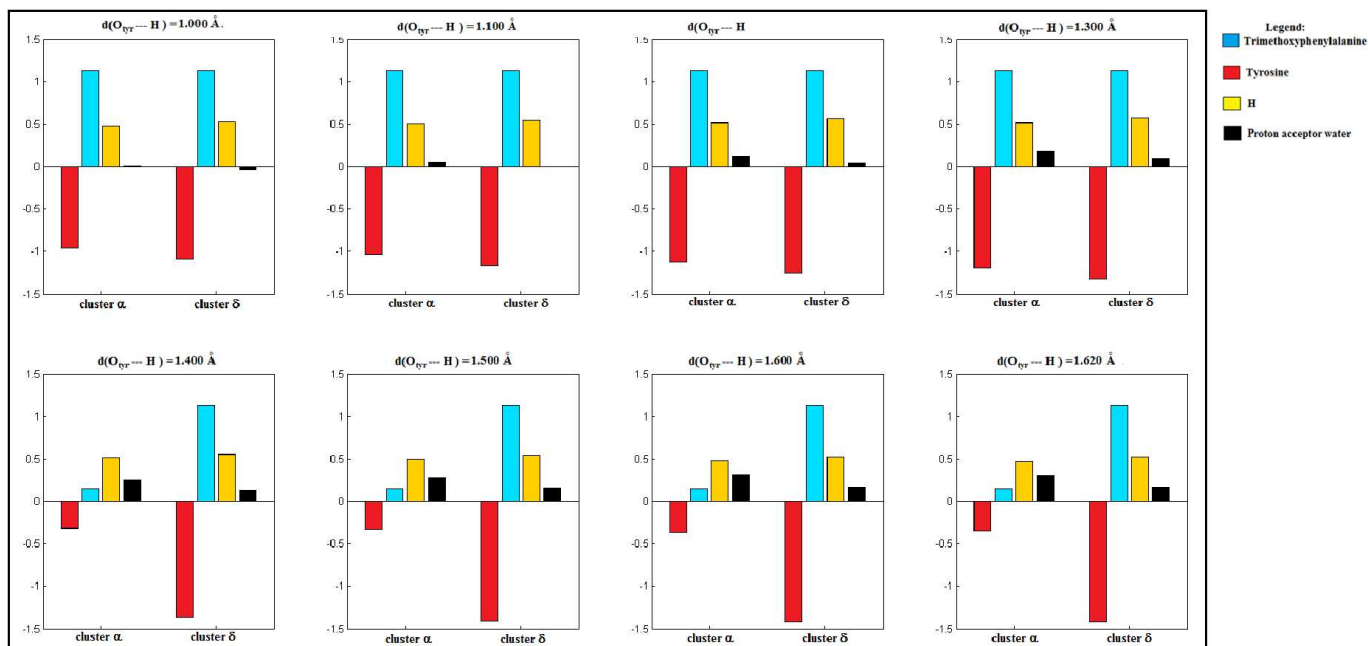


Fig. 4.4: Mulliken charges calculated for cluster α and δ at each point of the PCET profile. The H charge has to be added to that of tyrosine in the first points of the profile. In the same manner it has to be added to that of proton acceptor water in the last points.

At this point it's relevant to analyse the situation when one a single water molecule is considered as HBD the tyrosine oxygen, namely cluster γ . Also in this case the electron transfer does not take occur on the ground state PES.

4.3 Tryptophan as electron acceptor

The same analysis performed on the $YGGGF_{TRM}^{\bullet+}$ system has been repeated on $YGGGW^{\bullet+}$ one. As in the previous case, different solvation clusters including three, four, five and six water molecules, labeled as α , β , γ and δ , have been considered. In analogy to what happened with the trimethoxyphenilalanine, with the cluster α the electron is transfered along the ground state PES in correspondence of the a distance of 1.503 \AA for $O_{tyr} - H$. The situation remains unchanged when the fourth water molecule (cluster β) is considered.

In the situation of the δ cluster (Figure 4.2 (d)), the electron transfer doesn't occur on the ground state PES, and coupling with excited state PES is mandatory. The ET does not take place on the ground state PES, even in the case of cluster γ , in which a single water molecule solvates the tyrosine oxygen as HBD.

From this point of view the same consideration previously done are still valid. In particular, the analysis of the Mulliken charges similar to that of Figure 4.4 has shown that when the solvation of tyrosine is represented by the cluster γ or δ the formation of the phenolate rather than that of the phenoxide is more favored.

This situation is energetically promoted by the solvation water molecules of tyrosine oxygen.

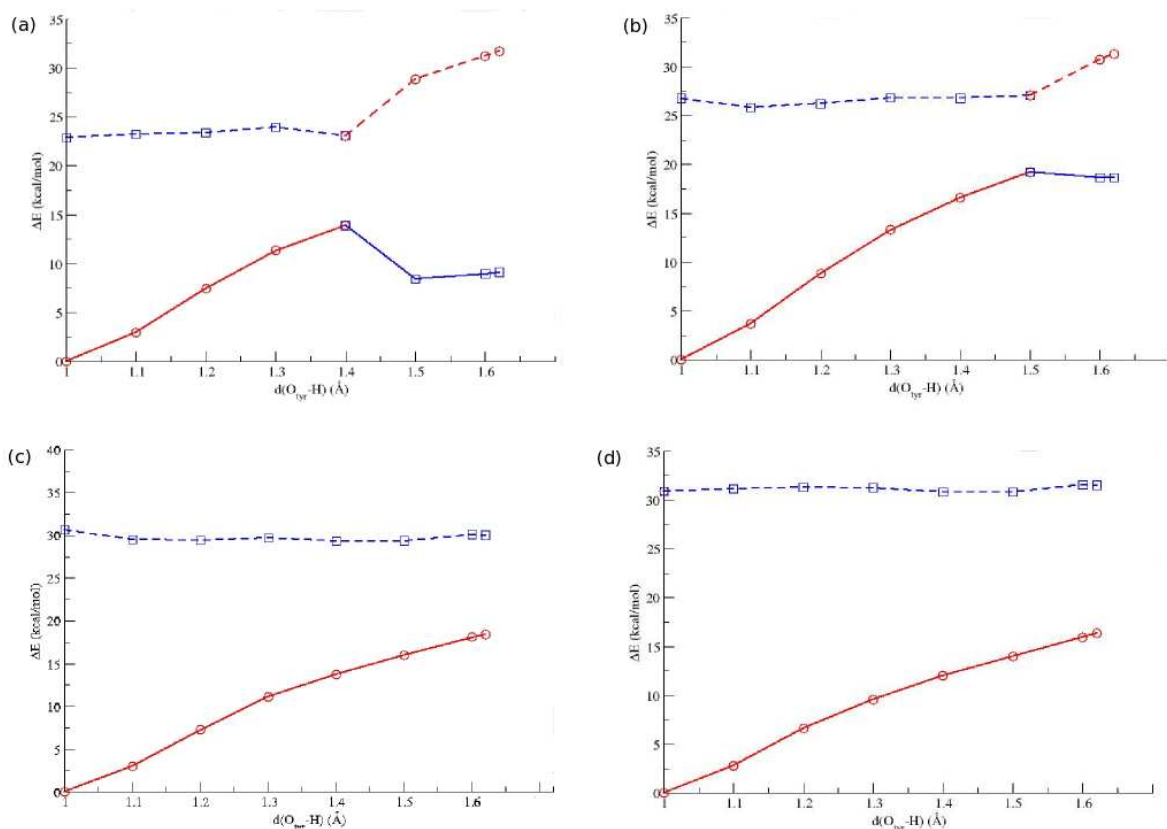


Fig. 4.5: Energetics Profiles:(a)cluster α ; (b)cluster β ;(c) cluster γ ; (d) cluster δ . Solid and dashed lines represent the ground state and first excited state adiabatic potential energy surface respectively. In the red and blue lines the radical is respectively localized on trimethoxyphenylalanine or tyrosine residue.

4.4 Results of the molecular dynamics simulation

Considering the results showed in previous Sections, it becomes very important to address the pending question, of which situation among α , β , γ and δ clusters should be considered more representative of the reality.

So, the exploration of the potential energy surface of the peptide through ab initio molecular dynamics simulation can provide an insight. A preliminary analysis on the microsolvation of the phenol has been performed. In Figure 4.6 *oxygen* –

oxygen and the *hydrogen–oxygen* radial distribution functions (RDF) involving the phenol hydroxyl group and water are shown as calculated from the ADMP/ONIOM trajectory. The $O_{phenol} - O_{water}$ RDF shows a maximum at about 2.5 Å, while the first two peaks of the $O_{phenol} - H_{water}$ RDF are located at about 2.0 Å and 3.3 Å respectively. The $H_{phenol} - O_{water}$ RDF shows a maximum at about 1.6 Å, after which RDF is lowered almost to zero. These results suggest that at standard condition, a proton acceptor water interacts with the proton of the phenol hydroxyl group. Analysis of the trajectory has also showed that for about 22% of the time O_{phenol} doesn't form any hydrogen bond (HB) as acceptor, for about 61% is acceptor of one HB, and for the remaining 17% of the time, it is acceptor of two HB. Instead, the time in which the hydroxyl group acts as HB donor of one water molecules is 99%.

This analysis can provide some indications about the statistical weight of the peptide-waters clusters previously examined. The microsolvation analyzed by MD indicates a distribution for which clusters α , γ and δ are representative of the 20%, 60%, 20%, of the time respectively. It turns that, the most representative cluster is the γ one. At this point a specific detail of the experimental setup has to be considered: the reaction was conducted in a mixture acetonitrile-water 3:1. A molecular dynamic simulation mimicking the ACN-water mixture in the ONIOM/ADMP with non periodic boundary condition formalism is really a stiff task, because of the significant effort required for the potential calibration. Here it is proposed an *a posteriori*

discussion, based on trivial statistical considerations. In a mixture 3:1 ACN-water the presence of a single water in a given volume is reduced to 1/4 with respect to the neat liquid. Therefore, the lifetime of clusters involving a large number of water molecules around the phenol can be expected to be quite reduced with respect to what inferred by MD in pure water. Hence, we can reasonably assume that the weight of α and β clusters is indeed more respect to the γ or δ . Doing so the statistic weight of α cluster rises becoming comparable to that of γ cluster.

4.5 2,4,6-trimethoxyphenylalanine versus tryptophan: a comparison of relative reactivity

As analyzed in section 4.2 and 4.3, the PCET process can occur differently depending on the tyrosine microsolvation considered. For what regards the electron acceptor, both trimethoxyphenylalanine and tryptophan showed the same general trend with respect the solvation cluster structure. In Figure 4.7 it is compared energetic profiles obtained for $YGGGF_{TRM}^{\bullet+}$ and $YGGGW^{\bullet+}$ with three water clusters. In both cases the PCET process occurs on the ground state PES. From inspection of Figure 4.7 it's clear that the energetic barrier for $YGGGW^{\bullet+}$ is higher of about 4 kcal/mol then the one of $YGGGF_{TRM}^{\bullet+}$. Despite this difference is relatively small, it implies alike a difference in the reaction rate of about three orders of magnitude. According to Marcus's theory, the rate constant can be calculated as :

$$k_{ET} = \frac{H_{DA}^2}{\hbar} \sqrt{\frac{\pi}{\lambda k_B T}} \exp^{-\frac{\Delta G^\ddagger}{k_B T}}$$

where H_{DA} is the electronic coupling between donor and acceptor, ΔG^\ddagger is the activation energy, and λ is the energy needed to transform the system coordinates into the final state with no charge transfer taking place. The accurate evaluation of the kinetic constant is beyond the goal of this work, but some indications about the relative reactivity can indeed be obtained. Assuming in first instance the electronic coupling and the reorganization energy to be comparable in the two cases, the relative ratio of the rate constants, can be considered is directly proportional to $\exp^{-\frac{\Delta\Delta G^\ddagger}{k_B T}}$.

Considering a $\Delta\Delta G^\ddagger$ of about 4 kcal/mol, a relative ratio of about three order of magnitude is found in the two kinetic constants. This difference can be attributed to the variation of molecular dipole moment along the PT coordinate. Indeed, in the region of transition state the dipole moment increases with a larger derivative its variation toward bigger value is greater in the case of $YGGGF_{TRM}^{\bullet+}$ with respect to $YGGGW^{\bullet+}$. As a consequence in a polar environment the transition state of $YGGGF_{TRM}^{\bullet+}$ is reasonable, leading to a smaller activation energy.

Therefore, our theoretical treatments predict and support the experimental evidences, even if we have considered only a partially relaxed energy profile. In a future works this protocol of analysis can be refined including for example, the effects of dynamics fluctuations of both the peptide and solvent degrees of freedom.

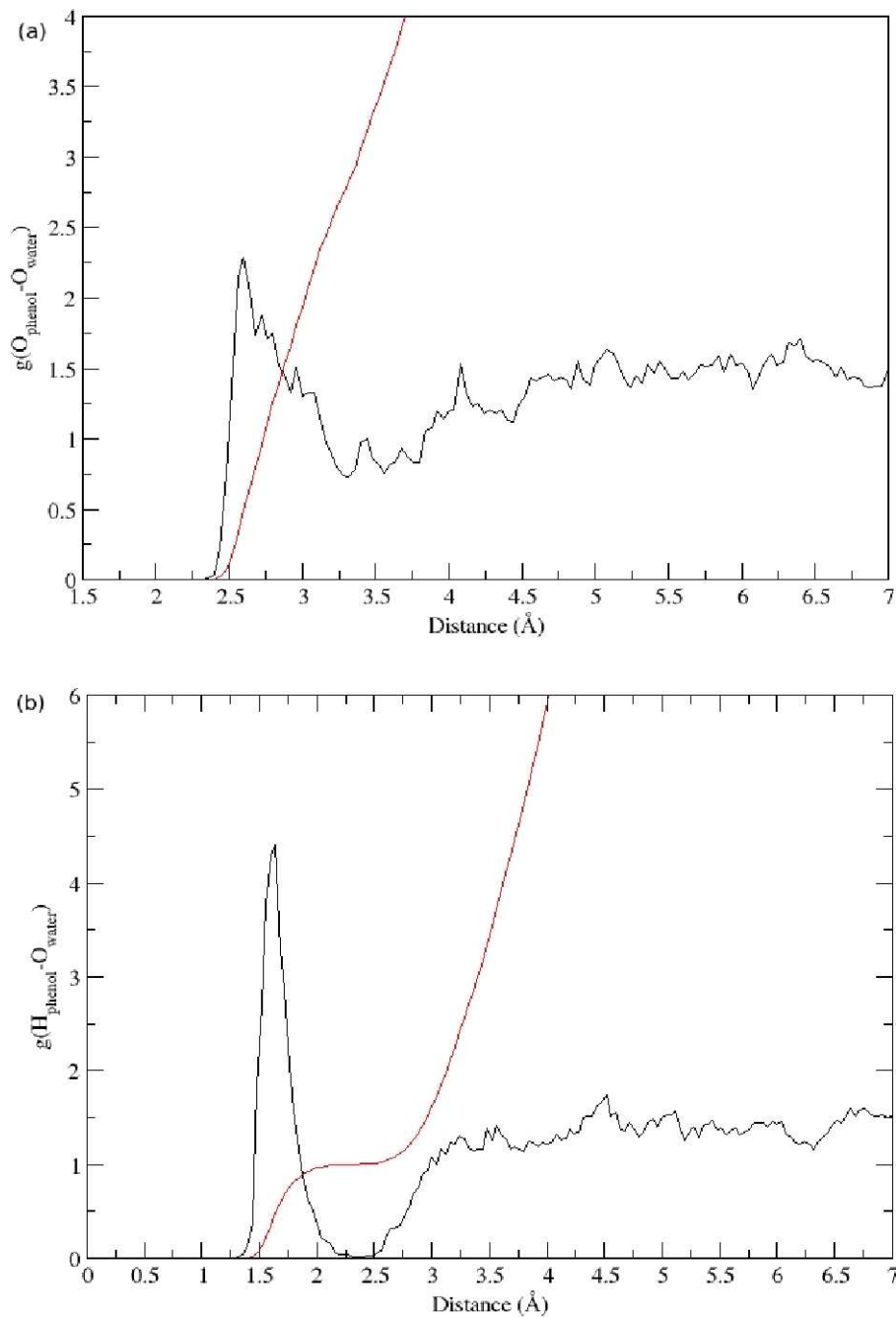


Fig. 4.6: Radial distribution functions of phenol oxygen (a) and hydrogen (b). All radial distribution functions (RDF) have been calculated in the following fashion. The number of events inside a certain bin-size has been calculated from the ADMP trajectory. This number has been then divided by the total number of configurations used, volume inside the spherical shell created by the chosen bin-size, and the number density of the system.

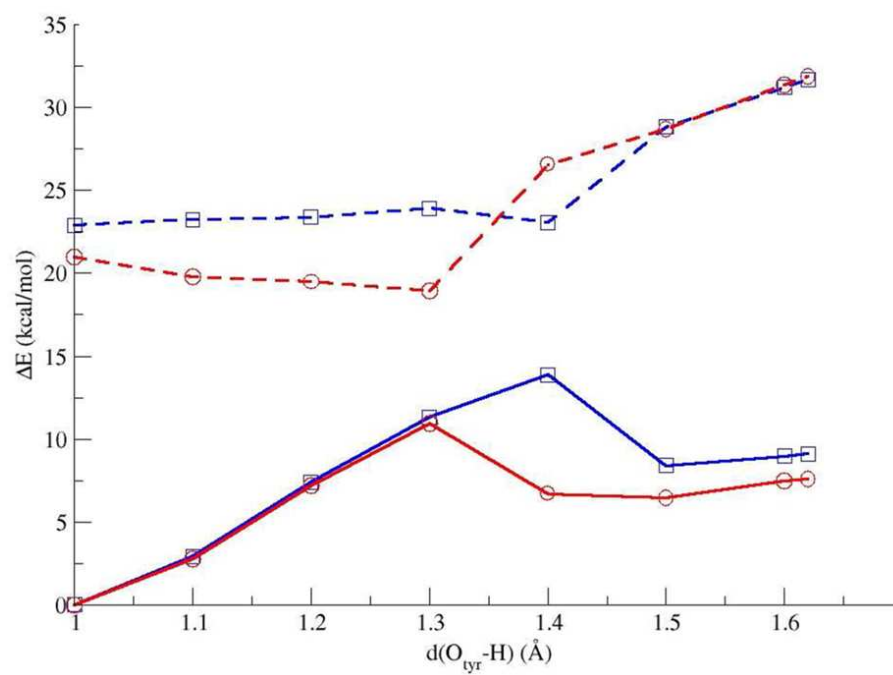


Fig. 4.7: Comparison of energetic profile of $YGGGF_{TRM}^{\bullet+}$ and $YGGGW^{\bullet+}$ in α cluster.

Chapter 5

On DFT accuracy in describing PCET reactions

From the theoretical point of view, the full characterization of a PCET reaction claims for an accurate description of the ground and excited potential energy surfaces (PESs). The accurate description of the Potential Energy Surface is far to be trivial for the difficulties encountered in the choice of both, on the quantum method able to provide a sufficiently accurate quantitative description of the PES and the effective reaction coordinate, As a matter of fact, since the proton motion, beside the problem related to the classical or quantum treatment of its dynamic, is accompanied to a significant electronic rearrangement and normally coupled to other nuclear degrees of freedom. In this sense, the separated fields of proton transfer (PT), and electron transfer (ET) reactions have been explored in terms of performances of exchange-correlation functionals thanks to a numerous systematic studies carried out in the last twenty years. It is established that gradient generalized approximations (GGAs) induce an underestimation of PT barrier, while the inclusion of a part

of Hartree-Fock (HF) exchange can alleviate this problem [172–177]. Similarly, it is well known that range-separated hybrids (RSHs) functionals give a better description of charge transfer processes. All these studies indicate that HF exchange is a key parameter in determining the capability of a density functional to describe the charge transfer phenomena. However, it is still to establish yet how these fine effects combine when ET and PT reactions are coupled together, and how the solvent can affect them. In this Chapter we analyzed the numerical performances of a large number of functionals, chosen as covering classes ranging from GGAs to RSHs, on PCET and ESPT reactions, with particular regard to the robustness of the common methods used to treat the condensed phase, Polarizable Continuum Model, PCM in its continuum like version [178, 179]. More closely, we compare results obtained adopting this implicit solvation models and with explicit models, taking the latter as reference for the solvent phase calculation.

5.1 Proton coupled electron transfer modeling and benchmarking

$\text{YGGGF}_{TRM}^{\bullet+}$ is a radical cation formed by the loss of an electron from 2,4,6-trimethoxyphenylalanine of the parent molecule. In the reactant state the radical and the positive charge are both localized on trimethoxyphenylalanine residue, the PCET leads to a product in which the radical and the positive charge are localized on the tyrosine residue and an hydronium ion, respectively. The electron transfer takes place between tyrosine and trimethoxyphenialanine, while the proton transfers between the tyrosine hydroxyl

group and a water molecule. The PCET reaction has been studied considering the water molecule cluster α considered in Chapter 4 and by scanning the energy along a constrained potential profile following an *ad-hoc* defined reaction coordinate (O_{tyr} -H distance). This cluster has been adopted to study the PCET reaction in gas phase and with an implicit model for the solvent. In order to obtain a peptide in aqueous solution with an explicit representation of the solvent, it was performed an ONIOM/ADMP simulation of the entire peptide system. The construction of the energy profiles has been done by extracting snapshots from the trajectory. In all cases, as previously illustrated in Chapter 4 a Mulliken spin densities (SD) analysis on each residue of the peptide along the PT coordinates has been considered for the progress of the electron transfer.

In the gas phase and in the aqueous solution the implicit solvation model partially relaxed energy profiles of the PCET reaction were obtained as follows.

The distance was scanned in the 1.00 Å to 1.62 Å range, while relaxing all other degrees of freedom, maintaining a constraint on the angles ϕ and ψ of the polyglycine backbone ($\phi = 75^\circ$ and $\psi = 145^\circ$) at the PBE0/6-31G(d,p)/CPCM level of theory. Bulk solvent effects were included by the means of the latest implementation of the polarizable continuum model CPCM [178, 179].

On the same structures we performed single points calculation in both the gas and in the implicit solvent. For what regards profiles obtained with the explicit representation of the solvent, an ONIOM/ADMP dynamics of the entire peptide was

simulated by embedding it inside a spherical box of radius 20.5 Å containing 1180 water molecules. During the simulation the YGGGF_{TRM} was treated at full QM level (B3LYP/6-31G), whereas harmonic constraints with force constant of 1×10^{-5} Hartree/Bohr² were imposed to the peptide to retain the PPII helix conformation. Non-periodic boundary conditions were enforced by the Generalized Liquids Optimized Boundary (GLOB) model. [169–171] A trajectory of about 2ps, of which the first 0.8 ps have been considered as equilibration time, has been collected. As starting point for the construction of the profiles it has been considered a snapshot of the trajectory in which the tyrosine oxygen forms only one hydrogen bond with the proton acceptor water. Starting from this structure it was performed an energy profile for the PCET reaction, scanning with single point calculations the O_{tyr}-H distance in the range of 1.00 Å to 1.68 Å. In all cases the following different functionals have been considered including GGA (BLYP, [180,181]), metaGGA (B97D, [182]), global hybrids (GHs) (B3LYP, [183] PBE0, [184] M06, [185] M06-2X, [185] BHandHLYP, [186] TPSSh), RSHs (CAM-B3LYP, [47] LC- ω PBE, [48] ω B97X, [49]). Moller - Plesset perturbative approaches [187], truncated at the second order (MP2) were chosen as reference level of theory for the gas and solvent phase calculations. The whole list of functionals adopted, with the associated HF exchange percentage is reported in Table 5.1.

The study of PCET in solution was performed by using both implicit and explicit models. In the former picture calculations were performed adopting the Polarizable

functional	% HF exchange ^a	reference
GGA		
BLYP	0	[180], [181]
meta-GGA		
B97D	0	[182]
GH		
TPSSH	10	[188]
B3LYP	20	[183]
PBE0	25	[184]
M06	27	[185]
M06-2X	54	[185]
BHandHLYP	50	[186]
RSH		
CAM-B3LYP	19/65 (0.33) ^b	[47]
LC- ω PBE	0/100 (0.40) ^b	[48]
ω B97X	16/100 (0.30) ^b	[49]

Table 5.1: List of the exchange-correlation functionals adopted in this thesis. ^aThe min/max for range separated hybrids. ^b Damping parameter in bohr⁻¹

Continuum Model in its Conductor-like version, the CPCM. We also tested two different type of molecular surface representing the solute-solvent boundary. The first one is the Van der Waals surface (VDW): it uses atomic radii for the atomic spheres composing the cavity (UFF radii scaled by a factor of 1.1), and skips the generation of added spheres to smooth the surface. This choice is the default in Gaussian 09 package. [189] The second one is the Solvent Accessible Surface (SAS), in which the radius of the solvent is added to the unscaled radii of solute atoms. On the contrary, in explicit solvent model the single point calculations were performed at ONIOM/CPCM level, [190] treating the $\text{YGGGF}_{TRM}^{\bullet+}(\text{H}_2\text{O})_3$ at QM level of theory (functionals list in 5.1), and the remaining water molecules at MM level using the TIP3P water model. [168] All of the single point calculations were carried out by

using the 6-31+G(d,p) basis set. All calculations have been performed using the Gaussian09 suite of programs. [189]

5.1.1 PCET energy profiles in the gas phase

In Figure 5.1 we report energy profiles calculated in the gas phase for the PCET reaction by adopting HF, MP2 and DFT functionals as level of theory.

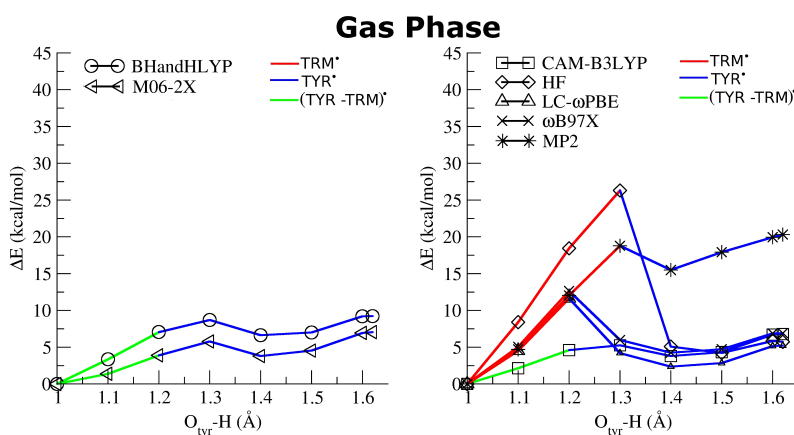


Fig. 5.1: Energetic profiles carried out in gas phase at different levels of theory and employing the 6-31+G(d,p) basis set. Reference structures have been optimized at PBE0/6-31G(d,p) level of theory. Red, blue and green lines represent respectively situations in which the radical is completely localized on 2,4,6-trimethoxyphenylalanine, on tyrosine, or is delocalized on both.

Making reference to functionals listed in 5.1, the graph does not include data obtained by BLYP, B97D and TPSSh because the Khon-Sham procedure on single points did not convergence. Other functionals like PBE0, M06, B3LYP, are excluded, because the gave convergence problems at some points along the profile. This is symptomatic of the sensitivity of the electronic problem for this radical cation, and the difficulty of obtaining a ground electronic state by DFT. In general,

functionals with high percentage of HF exchange, like M06-2X, BHandHLYP and RSH's functionals, are not affected by this convergence problem.

Regarding the PT barrier heights, a quantitative analysis is out of the purpose of the present work. As expected, taking MP2 as reference level we observe that HF overestimates the PT barrier of about 10 kcal/mol, while ω B97X and LC- ω PBE give PT barriers of about 12 kcal/mol, closer to the MP2 result. The other functionals (BHandHLYP, M06-2X, CAM-B3LYP) sensibly underestimate the barrier (~ 5 kcal/mol).

This lowering of the PT activation barrier is a well known limit of DFT [172–177, 191–193], and it can be related to the self interaction error, inducing an artificial overstabilization of delocalized states. As expected, this effect is less pronounced for functionals mixing in a certain amount of HF exchange. Regarding the energy profiles, BHandHLYP, M06-2X and CAM-B3LYP functionals show similar shapes, qualitatively comparable to the MP2 description. LC- ω PBE and ω B97X, on the other hand, anticipate of about 0.1 Å the O_{tyr} -H distance value corresponding to the maximum energy, that is our approximation of the PT Transition State (TS). BHandHLYP, M06-2X, CAM-B3LYP functionals, on the other hand, are in agreement with the TS position of the MP2 profile.

The proton transfer analyzed above is coupled to the electron transfer from tyrosine to the trimethoxyphenylalanine, and a consequent relocation of the radical on the peptide. In the MP2 case, the ET takes place at O_{tyr} -H distance of about

1.3 Å, in correspondence of the maximum energy. That means, up to a distance of 1.3 Å and before the PT event, the adiabatic ground electronic state fully corresponds to the diabatic configuration locating the radical form on the F_{TRM} residue (Mulliken spin density of F_{TRM} fragment SD=1). After the PT event, the adiabatic ground electronic state is represented instead by the diabatic configuration locating the radical form on tyrosine, while the F_{TRM} residue is in a closed shell-like form (thremethoxyphenylalanine SD=0, tyrosine SD=1). In proximity of the TS, therefore, we can predict an inversion of the two diabats in the composition of the electronic state, corresponding to the ET event. It is important to underline that Mulliken spin densities on the glycine residues and on the water molecules are zero along all the points of the energy profile.

Taking MP2 as reference, we analyzed Mulliken spin densities of tyrosine and trimethoxyphenylalanine residues obtained by HF and DFT. In 5.2 we report a 3D histogram of the spin density for each level of theory and at each value of the O_{tyr} -H coordinate.

Our analysis shows that, as it happens in the MP2 case, Mulliken spin densities on the remaining peptide and water molecules are negligible in all the cases, and are not reported in the graphs.

Notably, from inspection of 5.2 we observe that only LC- ω PBE, ω B97X functionals reproduce the behavior of MP2 and HF. As matter of fact, in these cases the radical remains on trimethoxyphenylalanine (the electron acceptor) until the tyro-

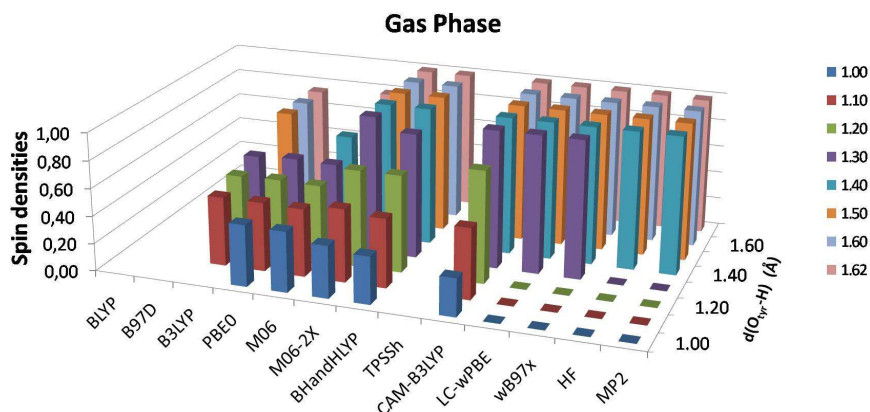


Fig. 5.2: Spin densities on tyrosine residue calculated in gas phase at different levels of theory. Single point calculations at BLYP, B97D and TPSSh levels of theory show convergence problems at any point of the profiles. The following single point calculations have shown SCF convergence problems: $O_{tyr-H}=1.00$ and 1.40 Å at B3LYP level; $O_{tyr-H}=1.40-1.62$ Å at PBE0 level; $O_{tyr-H}=1.50$ and 1.60 Å at M06 level of theory.

sine hydrogen is at least weakly bound to the proton acceptor water. On a closer inspection, we found that MP2, HF, LC- ω PBE, and ω B97X give a similar description of the PCET event also for what regards structural parameters other than the O_{tyr-H} distance. In particular MP2 predicts the PCET event at a $O_{tyr-O_{water}}$ distance of 2.643 Å, corresponding to a distance O_{tyr-H} of 1.403 Å, while LC- ω PBE and ω B97X give the reaction at a $O_{tyr-O_{water}}$ distance of 2.474 Å, corresponding to a distance O_{tyr-H} of 1.303 Å.

Other functionals instead, describe a progressive electronic transfer, with a spin density widespread on both the ET donor and ET acceptor. Therefore, the spin density assumes fractional values along the profile, gradually moving from trimethoxyphenylalanine to tyrosine, as the deprotonation proceeds.

More in detail, functionals as CAM-B3LYP, BHandHLYP, M06-2X describe a

complete ET after the PT event (tyrosine SD=1 for $O_{tyr-H} > 1.2 \text{ \AA}$) Remaining functionals, namely B3LYP, PBE0 and M06, predict a fractional spin density also in the PT product state, and are often characterized by SCF convergence problems.

In summary, functionals with an high percentage of HF exchange as ω B97X or LC- ω PBE (100 % of HF exchange at long range), describe well-localized radicals along the PT coordinate, in nice agreement with MP2 and HF. Functionals with a lower HF exchange amount, as M06-2X (54% of HF exchange), BHandHLYP (50%) or CAM-B3LYP (65% at long-range) describe delocalized spin densities at the beginning of the PCET reaction. Further decreasing of the HF exchange leads to convergence problems at many points of the profile: this trend is observed with B3LYP (20% of HF exchange), PBE0 (25%), M06 (27%). When the HF exchange is null like in the case of B97D and BLYP the convergence of the electronic state is never achieved, demonstrating a criticality in locating the radical. Again, this criticality of DFT is strictly related to SIE. Adding the HF exchange, which is free of the SIE by construction, allows for the reduction of the unphysical delocalization error. Semilocal functional (GGA, metaGGA) are unable to give a physically sound description of the radicals; the HF percentage in GH functionals is not adequate to localize the radical entirely; the 100% of HF exchange at long range of RSHs allows for a description of the electronic density localization similar to the MP2 and HF counterpart.

5.1.2 PCET energy profiles with an explicit solvation model

We recall that, at variance with other energy profiles discussed here, those obtained in explicit solvent refer to structures of the peptide not relaxed. As a consequence, reactants are presumably overstabilized with respect to products. Moreover, they are not directly comparable with the corresponding ones in the gas phase, at least from the quantitative point of view. However, a quantitative discussion on solvation effects in the PCET reaction is out of purpose of the present work. PCET energy profiles in explicit solvent and related Mulliken spin densities are reported in 5.3 and 5.4, respectively.

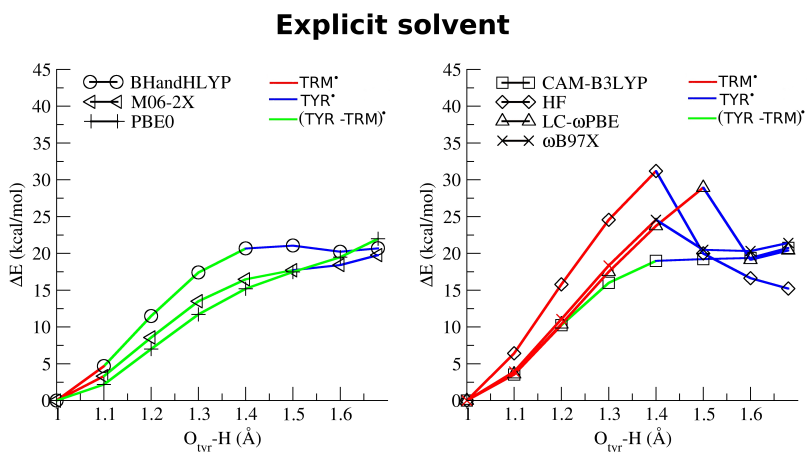


Fig. 5.3: Energetic profiles carried out with explicit solvation model at different levels of theory and employing the 6-31+G(d,p) basis set. Reference structures have been optimized at PBE0/6-31G(d,p) level of theory. Red, blue and green lines represent respectively situations in which the radical is completely localized on 2,4,6-trimethoxyphenylalanine, on tyrosine, or is delocalized on both.

By inspection of the results on Mulliken spin densities (5.4) it is clear that LC- ω PBE and ω B97X functionals give a localized picture of the radical, as HF. For what

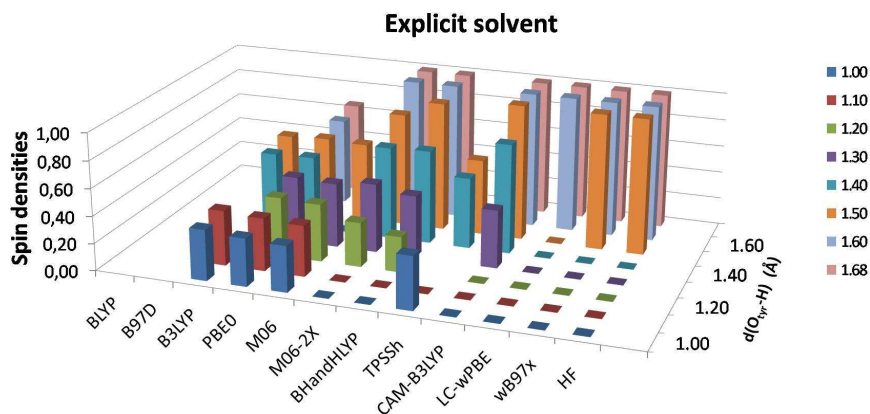


Fig. 5.4: Spin densities on tyrosine residue calculated with explicit solvent at different levels of theory. Single point calculations at BLYP and B97D levels of theory show convergence problems at any point of the profiles. The following single point calculations have shown SCF convergence problems: $O_{tyr-H}=1.20, 1.30, 1.60$ and 1.62 Å at B3LYP level; $O_{tyr-H}=1.40, 1.60$ and 1.62 Å at M06 level; $O_{tyr-H}=1.10-1.30, 1.60$ and 1.62 Å at TPSSh level of theory.

regards functionals as BHandHLYP, M06-2X, and CAM-B3LYP, the spin densities gradually moves from the trimethoxyphenylalanine to tyrosine, as the deprotonation occurs. Hybrid functionals with a small exchange as B3LYP, M06 give convergence problems.

In summary, the functionals performs a trend similar to that previously discussed in the gas phase. [194]

5.1.3 PCET energy profiles with an implicit solvation model

Energy profiles carried out in the gas phase have been recalculated in water by adopting the CPCM approach. We first discuss results obtained with the molecular cavity constructed by default in Gaussian, namely that included in a van der Waals surface. Energy profiles and spin densities are reported in 5.5 and 5.6, respectively.

At variance of what observed in both the gas phase and the explicit representa-

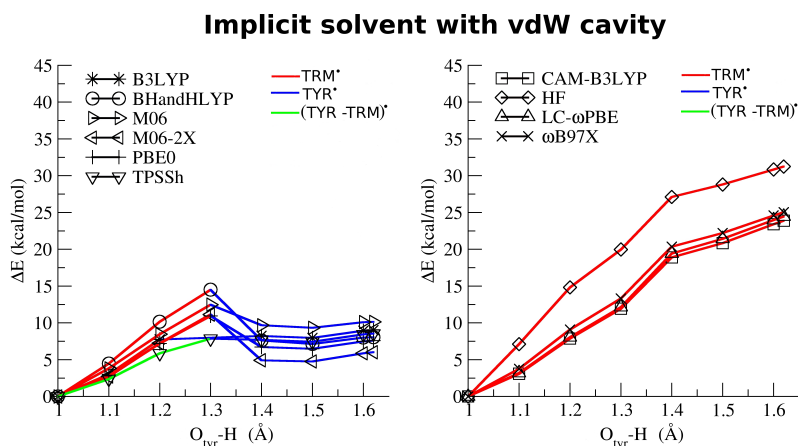


Fig. 5.5: Energetic profiles carried out with C-PCM model and VDW surface at different levels of theory and employing the 6-31+G(d,p) basis set. Reference structures have been optimized at PBE0/6-31G(d,p) level of theory. Red, blue and green lines represent respectively situations in which the radical is completely localized on 2,4,6-trimethoxyphenylalanine, on tyrosine, or is delocalized on both.

tion of the solvent, description at HF and RSH functionals levels of theory does not involve an electron transfer along the PT coordinate, at least in the ground electronic state. Instead, we observe an increasing of the energy of the ground state, which describes the radical always localized on the trimethoxyalanine residue. In particular, the final structure ($O_{tyr}-H=1.6 \text{ \AA}$), is characterized by a strong separation of charge, with a positive charge (and the radical) localized on the trimethoxyphenylalanine, a negative one on the tyrosine, and a positive charge on the H_3O^+ ion (see as SI the distribution of Mulliken charges). Therefore, the localization of the electronic density provided by HF and RSH functionals appears to be over-stabilized by the continuum solvent, and, although high in energy, the radical remains on the trimethoxyalanine also after the proton transfer to the water. As a consequence, the electron transfer is possible only in excited state. As an example, at the CAM-B3LYP/CPMC level the

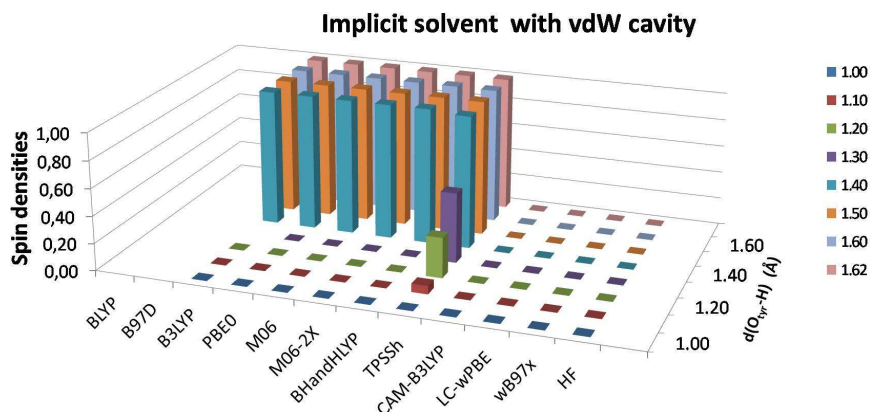


Fig. 5.6: Spin densities on tyrosine residue calculated with implicit solvent (vdW cavity) at different levels of theory. Single point calculations at BLYP and B97D levels of theory show convergence problems at any point of the profiles. The single point calculation at O_{tyr} -H distance of 1.30 Å has shown convergence problem at B3LYP level of theory.

PCET product lies 1.56 eV over the separated charge structure. On the other hand, functionals like B3LYP, PBE0, M06, M06-2X, BHandHLYP, and TPSSh, providing a delocalized picture in the explicit representation of the solvent, lead instead to the a correct PCET energy profile when combined with CPCM. In particular, in these cases the energy profile is characterized by an energy maximum corresponding to a O_{tyr} -H distance of 1.303 Å, and a PCET product corresponding to a relative minimum. That means, these functionals provide a complete electronic transfer upon formation of the hydronium molecule. As expected, the increase of HF exchange in the functional implies the growth of the barrier height, reaching its maximum value with BHandHLYP functional. The reversal of behavior in the vacuum or the explicit solvent with respect the continuum model can be also discussed focusing on the Mulliken spin densities distribution along the reaction coordinate (see 5.6). We observe that HF, ω B97X, LC- ω PBE, and CAM-B3LYP show a null spin densities

on the tyrosine residue along all the PT event. This is in contrast with the results gained in the explicit solvation model, which can be considered as reference for the solvent phase calculations. On the contrary functionals as M06-2X, BHandHLYP, M06, PBE0, B3LYP, describing delocalized spin densities in the gas phase and in explicit solvent, give instead a well localized description of the radicals when coupled to CPCM and the vdW surface. In these cases the addition of the solvent reaction field allows to better localize the radical and, somehow, to compensate the SIE effects observed in the gas phase and explicit solvent. This is a reasonable result, the SIE effects concerning the delocalization of charge, and being sensitive to the interaction with the solvent represented by a dielectric medium. In fact, this compensation has been already observed in other study cases, [194, 195] where the application of a dielectric field can essentially remove the artificial delocalization connected with the SIE.

In order to investigate better the effect of the continuum solvent, we carried out PCET energy profiles by CPCM calculations by adopting the Solvent Accessible Surface to build up the molecular cavity. By definition, the volume included by the solvent accessible area is larger than that enveloped by the van der Waals surface. Hence, the solvent reaction field calculated on SAS is monitored in proximity of a solute/solvent boundary that is, on average, more distant from the solute density, which can experience a minor solute/solvent interaction. As a consequence, the use of SAS should lead to the mitigation of both the stabilization effect of the separated

charge form and of the compensation of the Self Interaction Error. Moreover, we can expect that this effect is more important for those functionals exhibiting a faster asymptotic decay of the density, namely those with a small HF exchange percentage at long range. This is what we actually can infer from PCET energy profiles and Mulliken spin densities calculated by CPCM/SAS and reported in 5.7 and 5.8.

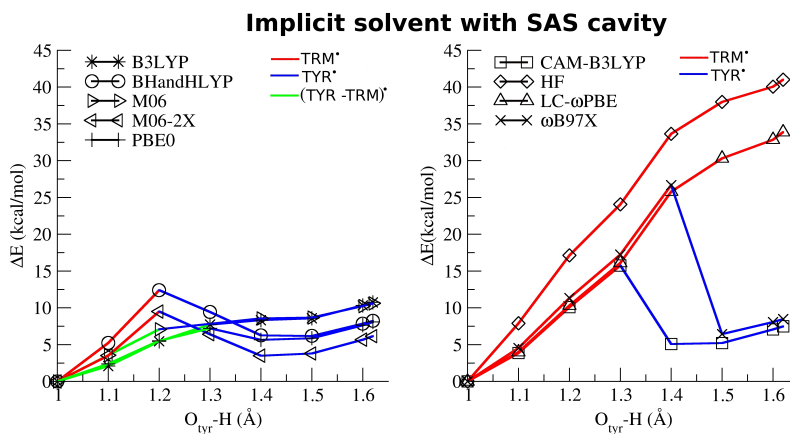


Fig. 5.7: Energetic profiles carried out with C-PCM model and SAS surface at different levels of theory and employing the 6-31+G(d,p) basis set. Reference structures have been optimized at PBE0/6-31G(d,p) level of theory. Red, blue and green lines represent respectively situations in which the radical is completely localized on 2,4,6-trimethoxyphenylalanine, on tyrosine, or is delocalized on both.

More closely, we observe for HF and LC- ω PBE the same behavior previously discussed for the vdW cavity, e.g. an over-stabilization of the separated charge form with respect to the PCET product, and a PT profile characterized by a steadily increasing of the energy. On the other hand, CAM-B3LYP and ω B97X describe a complete PCET with the stabilization of the tyrosil radical, showing a behavior opposed to the corresponding one obtained with the vdW cavity, but analog to the result given in explicit solvent. BHandHLYP and M06-2X provide a complete

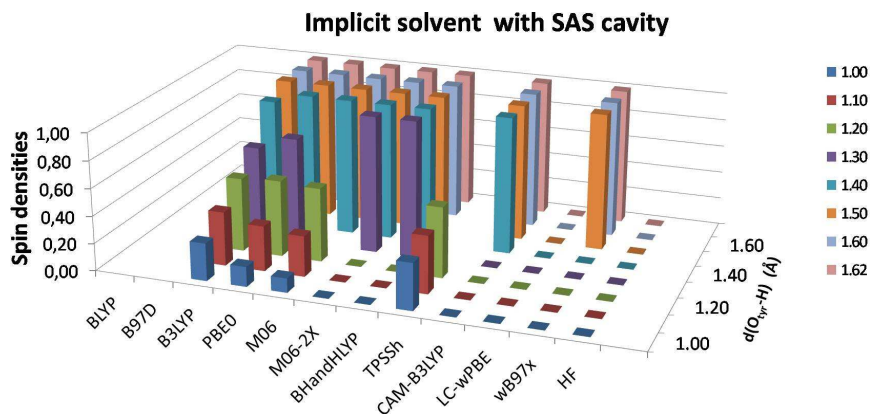


Fig. 5.8: Spin densities on tyrosine residue calculated with implicit solvent (SAS cavity) at different levels of theory. Single point calculations at BLYP and B97D levels of theory show convergence problems at any point of the profiles. The following single point calculations have shown SCF convergence problems: $O_{tyr}-H=1.30$ Å at M06 level; $O_{tyr}-H=1.30-1.62$ Å at TPSSH level of theory.

electronic transfer at a $O_{tyr}-H$ distance of 1.203 Å, therefore anticipating the event with respect to the explicit and implicit VDW solvent results. B3LYP, M06 and PBE0 provide a complete ET at a $O_{tyr}-H$ distance of 1.403 Å, similarly to what calculated by the vdW surface. PBE0, however, returns to a delocalized description of the spin density on the first points of the profile. In summary, HF and LC- ω PBE give a poor performance in aqueous solution in the PCM vision independently of the surface cavity, while for CAM-B3LYP and ω B97X we observe a surface cavity dependence: to reproduce the results obtained with the explicit solvent it is more suited the use of SAS surface respect to the VDW one. All the other hybrid functionals give a PCET in combination with the implicit PCM, although they can show a certain dependence on the cavity surface. In particular, B3LYP, PBE0 and M06 describe a delocalization of the spin densities in the first point of profile in combination with the SAS cavity, although it is less pronounced than that

previously observed in the gas phase and explicit solvent. Therefore, for all these these functional it seems more suited the use of the VDW surface. BHandHLYP and M06-2X with both cavities don't show a delocalization of the spin densities even if the ET event is anticipated with the SAS cavity. Criticities still remain for functionals with no HF exchange as B97D and BLYP, regardless of the cavity type.

5.2 Excited state proton transfer modeling and benchmarking

In Chapter it was presented a case of a light induced proton transfer reaction which represents an example of a "double wells" excited state reaction. The accuracy in the description of the excited state PES is not a negligible factor, due to the small quantities of energy regulating the balance between reactant and product. As reported previously, that gradient generalized approximations induce an underestimation of PT barrier when dealing with ground state reactions, and the inclusion of Hartree Fock exchange can correct this problem, [172–177]. In this sense an assessment step is mandatory if the issue under study involves an excited state proton transfer reaction. Therefore the ESPT reaction occurring between 7-hydroxy-4-(trifluoromethyl)coumarin and 1-methylimidazole(1-MeId, Figure efabrname) schematically represented in Figure 5.9 there considered as case study. The ESPT reaction has been studied considering to follow the proton transfer from the CouOH to the nitrogen atom of the 1-MeId base, by monitoring the energy of the system along a scan of the O-H distance in the 1.00-1.50 Å range, keeping the same

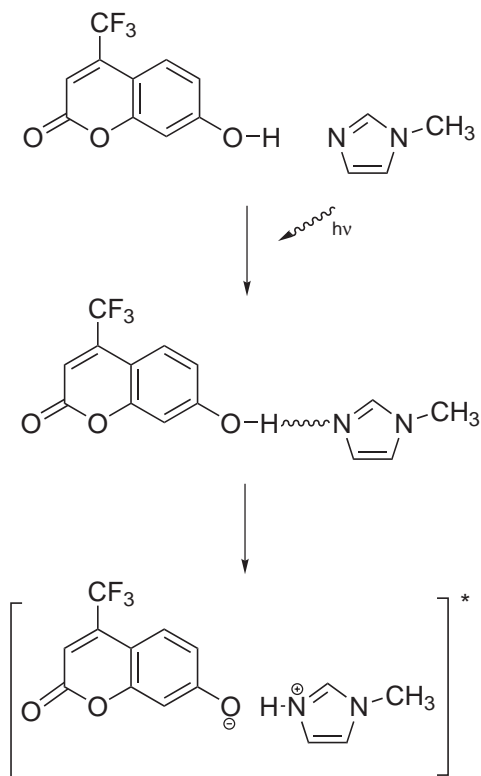


Fig. 5.9: Schematic representation of the ESPT reaction analyzed in this work

geometry when comparing different functionals. As it is well known in literature, most benchmarks are based on the assumption that structural parameters are less sensible in the choice of the functional than other properties, including thermochemistry. Therefore, it is well accepted nowadays to test DFT approaches using given fixed structures, for example obtained with properly chosen levels of theory. On this line, it was chosen to test DFT functionals by fixing structures obtained at TD-B3LYP/6-61+G(d,p).

DFT and TD-DFT [32] approaches were exploited to investigate ground and excited state potential energy surfaces.

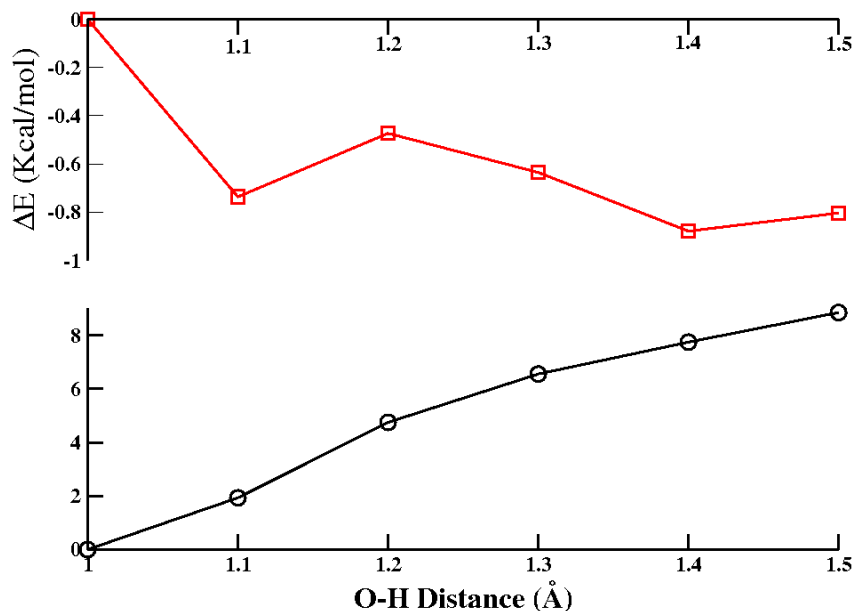


Fig. 5.10: Energetic profiles computed at B3LYP/6-31+G(d,p)/PCM level of theory. Black circle and red square lines correspond to the ground and excited states, respectively.

A constrained potential energy profile following an *ad-hoc* defined reaction coordinate was computed by scanning the O-H distance in the 1.00-1.50 Å range, while relaxing all other degrees of freedom at the TD-B3LYP/6-31+G(d,p)/PCM level.

On these structures we performed single point calculations with different functionals keeping the same basis set and model for the solvent, which is toluene in all cases.

Functionals considered include GGA (GRAC, [196] BLYP, [180,181], TCA, [197] PBEPBE [198]), metaGGA (VSXC, [199] B97D, [182]), global hybrids (GHs) (B972, [200] B1LYP [201] BMK [202] X3LYP, [203] B3LYP, [183] B3LYP-D, [204,205] BHandHLYP, [186] mPW1PW91, [206] mPW1K, [207] PBE0, [184] M06, [185] M06-2X, [185] M06-HF [208] TPSSh [188]), RSHs (CAM-B3LYP, [47] LC-PBEPBE, [209]

LC- ω PBE, [210, 211] ω B97XD, [212] ω B97X, [213] ω B97, [213] and double hybrids PBE0-DH, [214] and B2PLYP [215]

5.2.1 Unrelaxed energy profiles

In Figure 5.11 they are reported energy profiles obtained with GGA functionals (BLYP and PBEPBE), and meta-GGA (VSXC, B97D). In the case of GGA functional (Figure 5.11(a)) both BLYP and PBEPBE decrease the energy by contracting the O-H distance, namely by forming an H-bond adduct when compared to B3LYP, i.e., it results that BLYP and PBEPBE predict this H-bond adduct to be more stable. For what regards PBEPBE, the ES curve is rather flat for O-H values corresponding to the H-bond adduct, namely, 1.10-1.15 Å, while the BLYP functional locates this H-bond adduct as a minimum with a shorter length of the O-H distance (1.10 Å). It is evident that, in absence of HF exchange, the ESPT reaction results to be not thermodynamically favored due to the higher energy of the product compared to the reagent.

Regarding the shape of the profile, while the BLYP functional gives a very low barrier (about 0.10 kcal/mol) with respect to B3LYP (which was computed to be about 0.25 kcal/mol), with PBEPBE functional we observe a monotonically increase of the energy by elongating the O-H distance.

When the kinetic energy density is included in the functional (Figure 5.11(b)) it can be observed that, the H-bond adduct is located as a minimum (which again results to be more deep compared to the B3LYP case). As in the previous case,

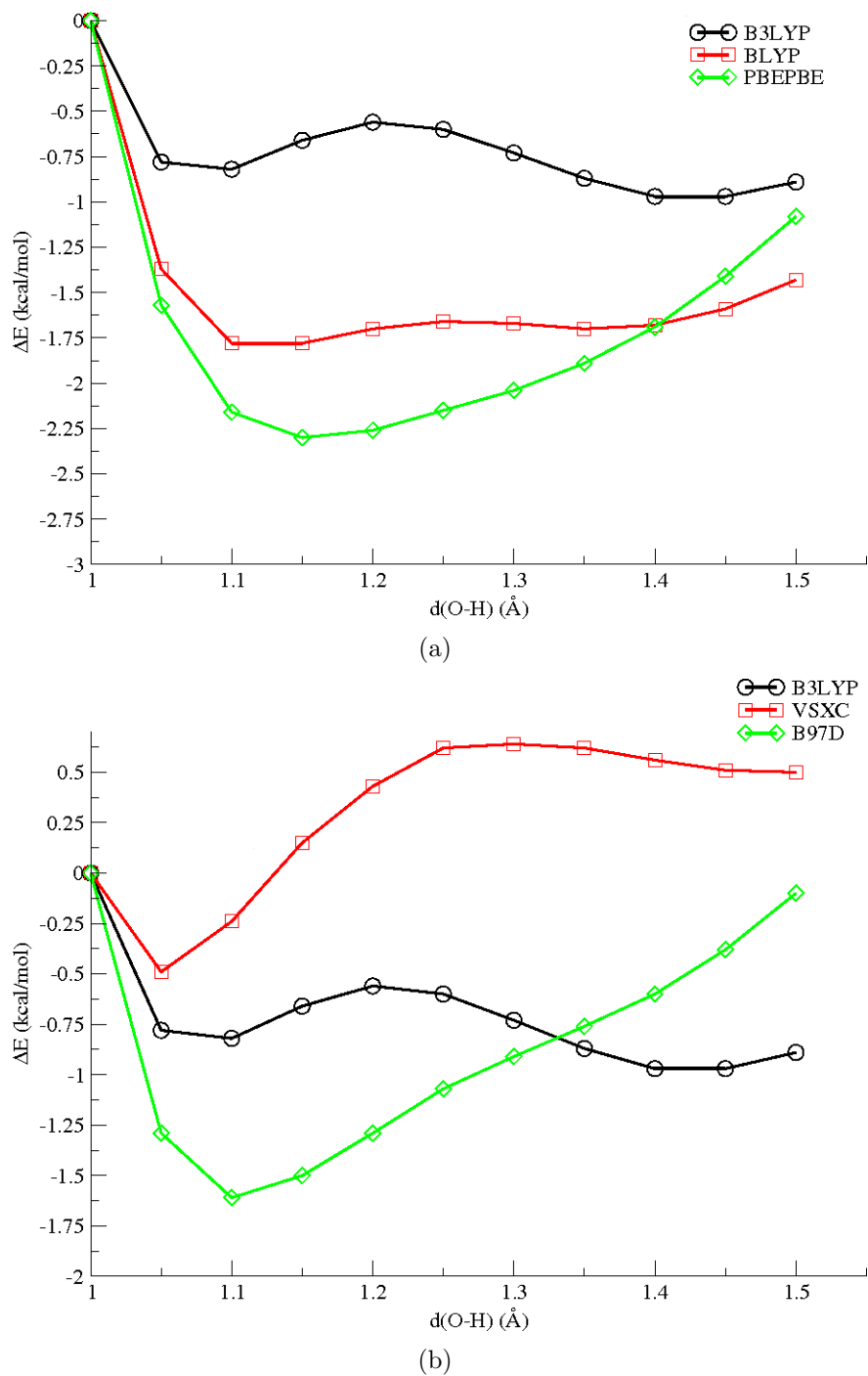


Fig. 5.11: Energetic profiles carried out with PCM model the 6-31+G(d,p) basis set (list of functionals in the legend). Reference structures have been optimized at B3LYP/6-31+G(d,p) level of theory.

the product shows a higher energy compared to the reagent for both functionals. In the case of the VSXC functional, after the H-bond adduct is formed, an increase of the energy of about 1 kcal/mol up to *plateau* is observed. Regarding to the B97 including the Grimme's correction [215], namely B97D, after the H-bond adduct minimum, located at an O-H distance of 1.10 Å, a monotonical increase of the energy is reported. The behavior of global hybrid functionals with an HF exchange less than 40% is reported in Figure 5.12.

From inspection of Figure 5.12(a), it can be noted that X3LYP behaves quite similarly to B3LYP, with the H-bond adduct located at about -0.7 kcal/mol with respect to the zero, and the product stabilized with respect to the reagent of about 0.2 kcal/mol. Regarding to the shape of the energetic profile, a small barrier of about 0.2 kcal/mol is individuated. B1LYP energetic profile results to be similar to X3LYP and B3LYP, but the reagent exhibits an O-H distance in accordance with the B3LYP (1.05Å), while the product shows a longer O-H distance (1.45Å), when compared to B3LYP results. The energetic difference between reagent and product computed with the B1LYP functional is rather small (about 0.05 kcal/mol).

The hybrid functional with the Tao, Perdew, Staroverov, and Scuseria correlation, TPSSh, shows a similar shape of the profile compared to the B3LYP, but in this case the reagent exhibits a longer O-H distance (1.10Å), while the product located at a O-H of 1.40Å is well characterized as minimum. The energetic difference between them results to be rather small (about 0.05 kcal/mol), with an associated

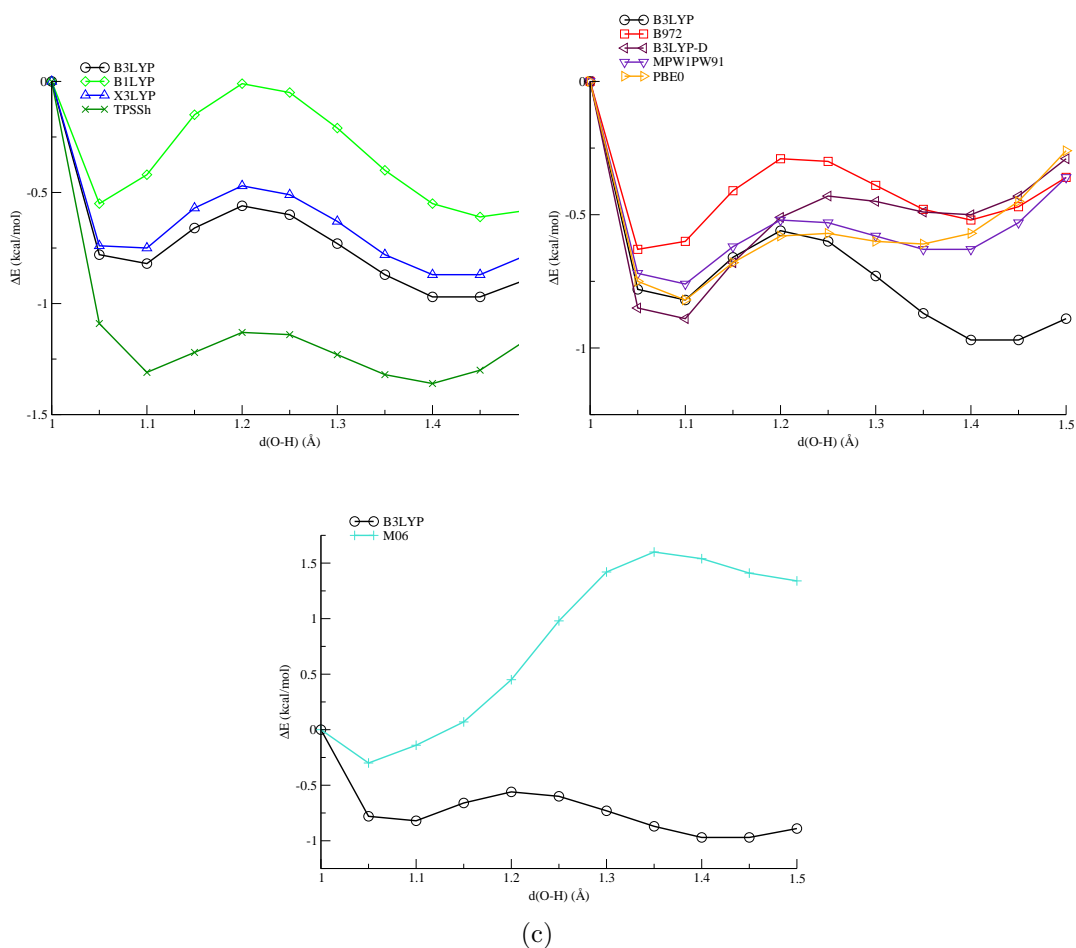


Fig. 5.12: Energetic profiles carried out with PCM model the 6-31+G(d,p) basis set (lower panel functionals with less than 40% of HF exchange, upper panel those with more than 40% of HF exchange). Reference structures have been optimized at TD-B3LYP/6-31+G(d,p) level of theory.

barrier of about 0.15 kcal/mol.

In Figure 5.12(b) B972, B3LYP-D, MPW1PW91 and PBE0 profiles are reported. It results that, when including Grimme's dispersion [215] in the B3LYP functional, the reactant lies in a deeper minimum compared to B3LYP, while the product exhibits a higher energy compared to the reagent. PBE0 also, shows a similar behavior for the product, while the description of the reagent is rather similar to B3LYP. At a first glance, the problem of describing the "double wells" excited state reaction seems to be connected to the description of the well in which lies the product, and therefore to the description of the energetic barrier between the two wells, rather than to the description of the reagent's well. B972 functional anticipates the minimum of the reagent at a O-H distance of 1.05Å, and the energetic profile predicts the product to be not favored of about 0.10 kcal/mol with an associated energy barrier of 0.30 kcal/mol. The mPW1PW91, with Perdew-Wang exchange as modified by Adamo and Barone [206] combined with PW91 correlation, describes rather well the first well and the following barrier, but the well of the product is not so stabilized to predict the ESPT reaction to be favored.

Finally, in Figure 5.12(c) results obtained through the Truhlar and Zhao hybrid functional M06 [185] are reported. It can be inferred from inspection of Figure 5.12(c) that M06 fails in describing the thermodynamics of the reaction, being the product destabilized of about 1.7 kcal/mol. Furthermore, the minimum of the reagent is centered in correspondence of a O-H distance of 1.05Å.

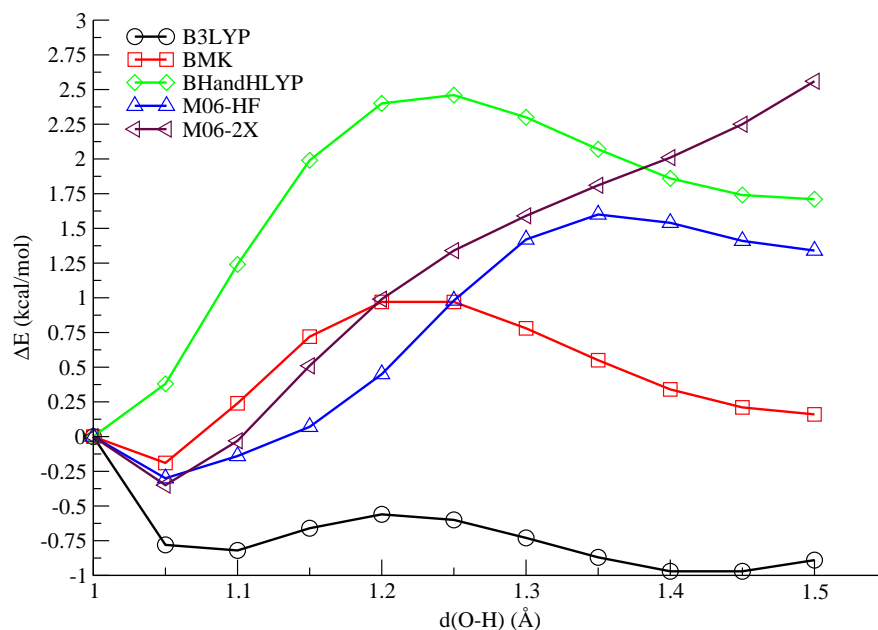


Fig. 5.13: Energetic profiles carried out with PCM model the 6-31+G(d,p) basis set (list of functionals in the legend). Reference structures have been optimized at TD-B3LYP/6-31+G(d,p) level of theory.

Energetic profiles obtained with functional including more than 40% of HF exchange, namely BMK, BHandHLYP, M06-HF, and M06-2X are reported in Figure 5.13. Starting from those belonging to Truhlar and Zhao hybrid functional M06 family, M06-HF and M06-2X behave quite well in describing the reagent as lying in a minimum. However M06-HF seems to be able to locate the product as lying in a minimum, but, as seen for M06, it is predicted to be higher in energy with respect to the reagent. On the other hand, M06-2X increases monotonically the energy along the entire profile. Boese and Martins kinetic energy density dependent hybrid functional, BMK, and half and half Becke's functional, BHandHLYP, describe energy profiles quite similarly in the barrier and product regions. Main differences can be

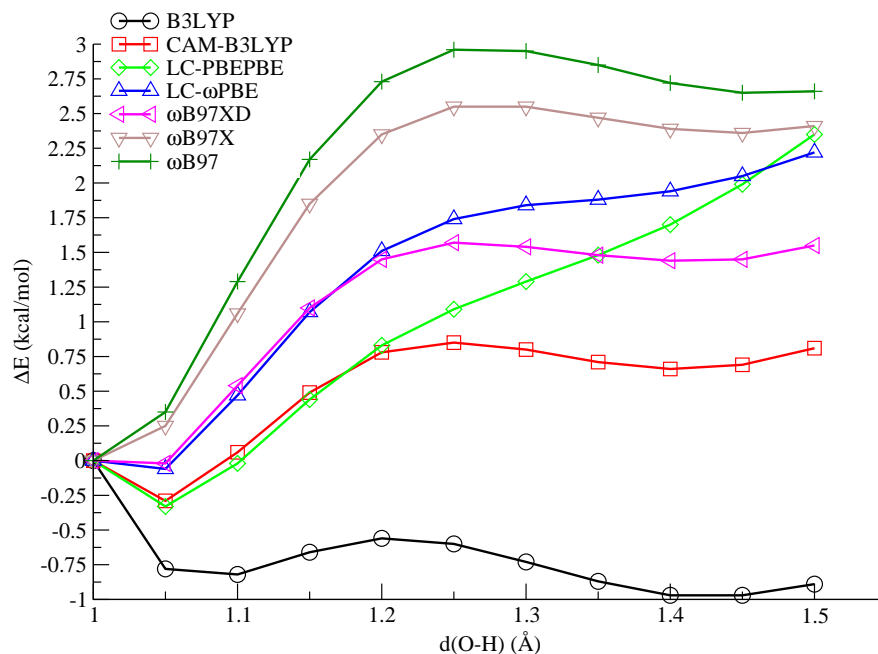


Fig. 5.14: Energetic profiles carried out with PCM model the 6-31+G(d,p) basis set (list of functionals in the legend). Reference structures have been optimized at TD-B3LYP/6-31+G(d,p) level of theory.

found in the description of the minimum in which lies the reagent which is better described by BMK functional, while it results to be absent in the BHandHLYP case. Regarding to Long Range corrected functionals, CAM-B3LYP, LC-PBEPBE, LC- ω PBE, ω B97XD, ω B97X and ω B97 results are reported in Figure 5.14. From inspection of Figure 5.14 it can be inferred that all RSH functionals seems to be able to locate the reagent (O-H distance 1.05 Å in all cases) in a minimum that can be more or less pronounced. For what regards the energetics of the overall process, all RSH functionals attribute an higher relative energy to the product when compared to the reagent. For what concerns the B97 functionals family, including an extra parameter, in the long range correction best performances in describing the shape

of both wells are obtained with ω B97XD. Generally speaking, for the family of B97 functionals the energetic barrier is rather high (at least 1.60 kcal/mol). Regarding LC-PBEPBE and LC- ω PBE, this latter performs rather similar to ω B97XD in the first part of the energetic profile, while higher relative energies are computed after the barrier. For what concerns LC- ω PBE the minimum in which lies the reagent seems to be described quite well, but the energy monotonically increases and the product is not found to lie in a minimum. Finally, CAM-B3LYP functional is considered. Handy and coworkers long range corrected version of B3LYP behaves quite well (very similarly to C- ω PBE) in describing the shape of the minimum in which lies the reagent. However, comparing CAM-B3LYP and B3LYP, B3LYP predicts a lower relative energy associated to the H-bond adduct. On the other hand, CAM-B3LYP (as all RSH do) fails in describing the thermodynamics of the overall process, placing the product higher in energy with respect to the reagent of about 0.95 kcal/mol.

5.2.2 Relaxed energy profiles with other functionals

Comparing the S_1 scan along the O-H distance obtained with different functionals on S_1 B3LYP relaxed structures represents a way to single out effects due to intrinsic nature of the functional. However, in order to investigate further the DFT accuracy in describing S_1 PES associated to the excited state proton transfer, it is mandatory to investigate the possibility that, vertical energies computed with each functional on TD-B3LYP relaxed structures, can be affected by the difference between potentials. Therefore constrained potential energy profiles following the same reaction coordi-

the product are obtained by single points calculation on S_1 relaxed structure with B3LYP with respect to those obtained by relaxing with the corresponding functional. This feature is true also in the case of the H-bond adduct, the reagent, when the PBE0 is considered, even if both energies are quite similar to those computed with B3LYP, at variance with other cases. M062X functional monotonically increases the energy after the minimum in which lies the reagent, and it is quite interesting to observe that, after the energy profile point in which O-H distance assume the 1.25 Å values, M062X relaxed structures assume higher relative energetic values with respect to the ones computed on B3LYP structures. For what concerns half and half Becke's functional, BHandHLYP, the reagent does not lie in a minimum and not relevant differences can be achieved by comparison of BHandHLYP and B3LYP S_1 relaxed structures. Finally, regarding BMK functional, from inspection of Figure 5.15 both energy profiles computed on BMK and B3LYP S_1 relaxed structures behaves quite well in describing the minimum in which lies the reagent, but not so well for what concerns the minimum of the product. Furthermore, by relaxing on the S_1 PES with BMK functionals higher energies are achieved compared to S_1 relaxed B3LYP structures. In Figure 5.16 they are reported long-range corrected functionals: Handy and coworkers long range corrected scheme for B3LYP, CAM-B3LYP, long range corrected PBE/PBE and Head-Gordon's ω B97XD including dispersion. CAM-B3LYP (Figure 5.16(a)), among RSH functionals, produces the sharpest minima for the reagent and the product, but as it happen for all RSH, the product is

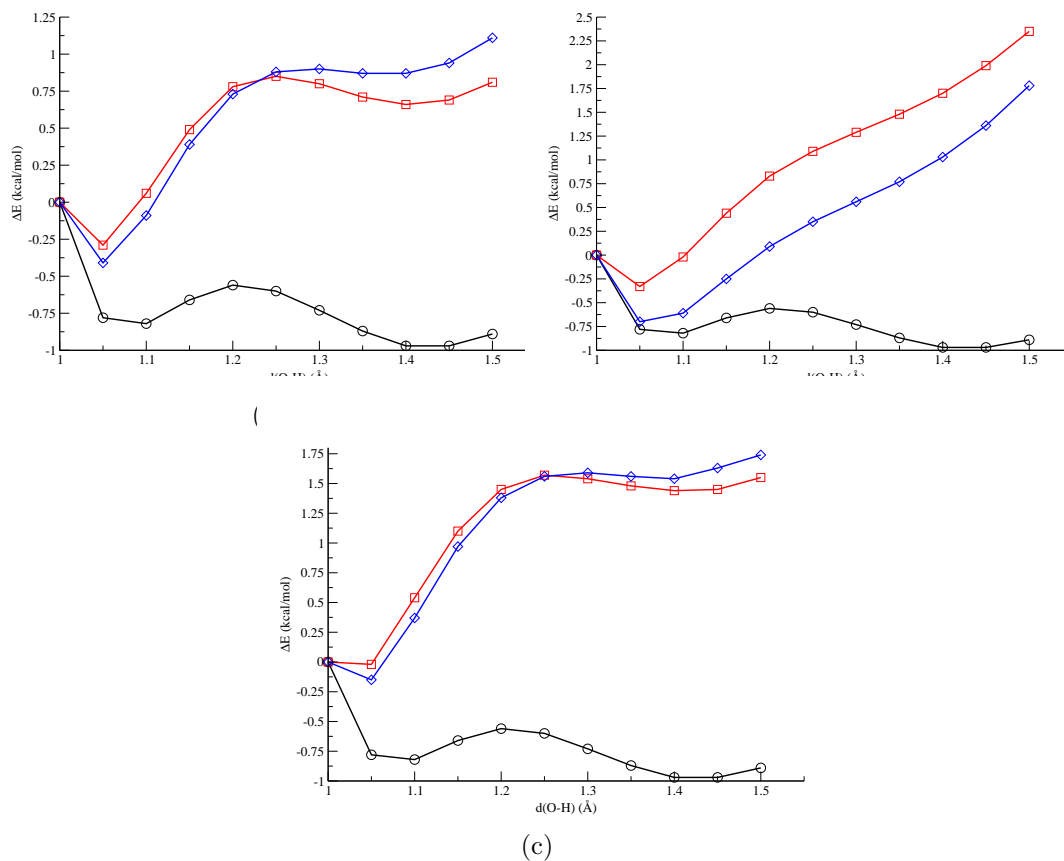


Fig. 5.16: Relaxed energetic profiles carried out with PCM model the 6-31+G(d,p) basis set with different RSH functionals

unfavored in energy respect to the reagent (in average of about 0.75 kcal/mol). In the case of long range corrected PBE-PBE, a monotonically increase of the energy along the profile is recorded, therefore compared to PBE-PBE computed energy on S_1 relaxed B3LYP structures main differences are not observed. Finally in the case of Head-Gordon's ω B97XD the relative behavior of ω B97XD and B3LYP relaxed structures is replied.

Chapter 6

Non Radiative Decay Process: the Intriguing Spiropyran Case

The goal of the present Chapter is to show how, using reliable and robust DFT approaches, it is possible to correlate the charge transfer character of an excited state to the main photophysical features of a photo-reaction, including the characterization of stationary points of the ES PES. In particular, well-suited electronic density based indices can be of great support in providing hints on the most probable reaction channels. To illustrate this approach, the photo-induced ring opening reaction of a photochromic spiropyran schematically represented in Figure 5.9 is here considered as case study. This system has been deeply studied in last years, both experimentally, in particular from a spectroscopic point of view, and also by theoretical approaches, in particular regarding the nature and the mechanism of the excited-state ring opening reaction.

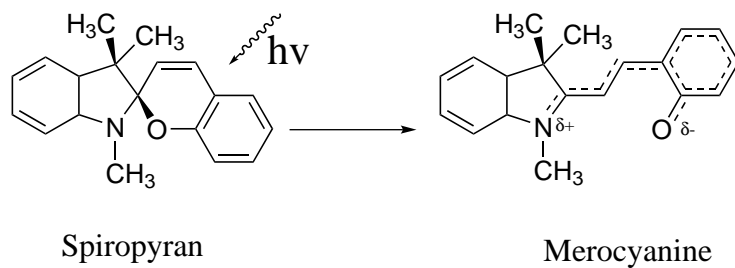


Fig. 6.1: Structural formula of the species considered in this work.

6.1 Structural and electronic features of SPt and BIPS

Before describing in more details the excited state ring opening mechanism, the electronic and structural features of two spiropyrans, the SPt and BIPS molecules, are compared (Please see Figure 6.1). The main structural parameters are summarized in Table 6.1.

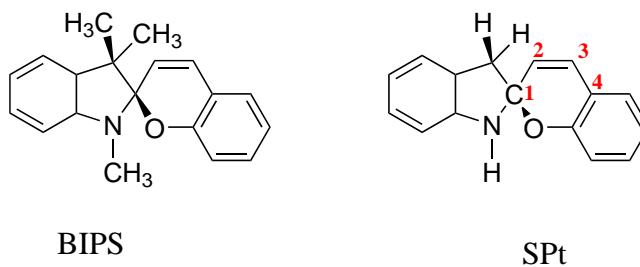


Fig. 6.2: Structural formula of the species considered in this work.

	BIPS	SPt
C_1O	1.47	1.47
C_1N	1.46	1.45
C_1C_2	1.50	1.51
α	-111.29	-142.39
β	-0.83	3.71
γ	-3.84	8.90
μ	-5.74	12.71
τ	177.04	-176.78

Table 6.1: Main structural parameters (\AA and degrees), computed for the ground S_0 state of BIPS and SPt. α N-C₁-C₂-C₃, β C₁-C₂-C₃-C₄, γ C₂-C₃-C₄-C₅, μ O-C₃-C₂-C₁ and τ H(C₂)-C₁-C₃ dihedral angles connectivity.

For what regards the ground state, the C_1O , C_1N and C_1C_2 distances are rather similar in the two molecules, while regarding the dihedral angles some differences can be found. In particular the α angle assumes values of -111.29 and -142.39 for BIPS and SPt, respectively.

This reflects the fact that in SPt the two methyl substitutes have been replaced with two H atoms, and as a consequence, the reduced steric interactions with benzopyrane oxygen atom experienced from H atoms in SPt molecule permits the α angle to assume an higher value.

Regarding β and γ dihedral angles, it is possible to find more similar values, because the reduced effect of substitution.

Focusing on the two dihedral angles more involved in the ring opening process, we observe that, μ describes the coplanarity of C_1 atom with respect to the O- C_3 - C_2 atoms belonging to the pyran ring, while τ describes the coplanarity of H(- C_2) with respect to C_2 - C_1 - C_3 atoms. The μ angle adopts values of -5.74 and 12.71, in BIPS and SPt, respectively, while the τ angle has very similar values of 177.04 and -176.78 in the two cases. The rather similar values of C_1O , C_1N and C_1C_2 , distances and τ angles can ensure us, that, at least in the molecular portion in which the reaction takes place, the reduced molecule, SPt, is very similar to BIPS.

Regarding the absorption process, on these ground state minimum energy structures excitation energies were computed at the TD-CAM-B3LYP/6-31+G(d,p) level of theory. In both cases the nature of one intense vertical transition, corresponds

basically to a one electron excitation from the HOMO-1 to the LUMO, as it can be inferred from the analysis of the orbitals involved, and of the associated ground to excited state density difference reported in Figure 6.3. That transition shows

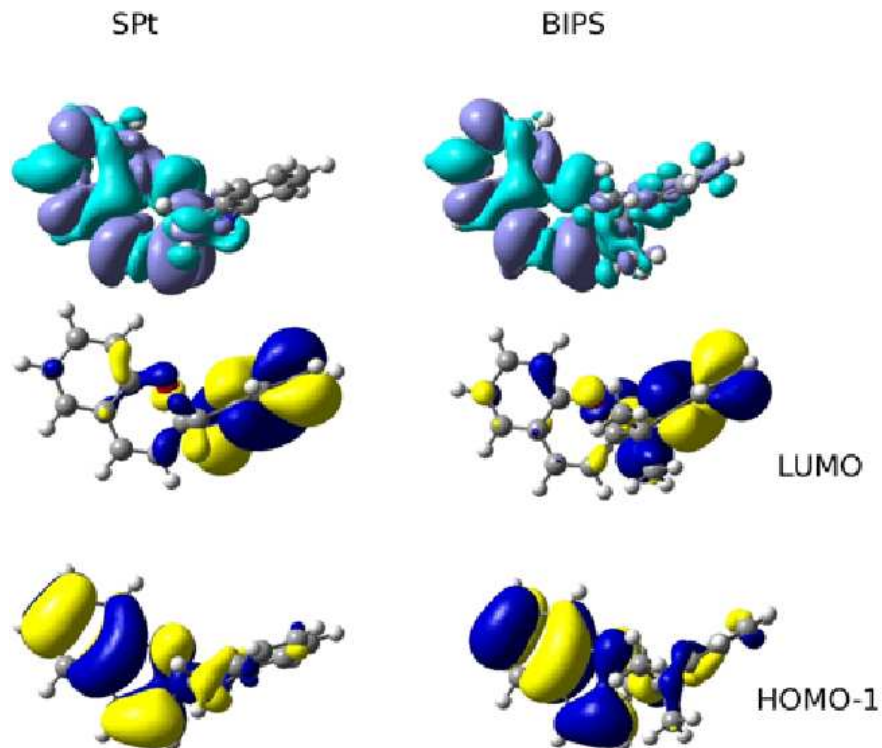


Fig. 6.3: Contours of HOMO-1 and LUMO and difference in electronic densities (upper panel) computed at the TD-CAM-B3LYP/6-31+G(d,p) level of theory on ground state minimum energy structures obtained at the B3LYP/6-31+G(d,p) level of theory for Spt and BIPS molecules.

maximum for BIPS at 4.39 eV ($f=0.0714$) and 4.41 eV ($f=0.1092$) (CAM-B3LYP) for the Spt molecule, respectively.

Moreover, it shows a $\pi \rightarrow \pi^*$ and a locally excited (LE) character, rearranging electronic density in the benzopyran molecular portion, as confirmed by the computed vertical D_{CT} of 0.618 and 0.913 Å for BIPS and Spt, respectively. Finally, this transition has to be compared with the spectroscopical characterization performed

in Reference [10], which shows a 4.13 eV sharp band for the absorption spectrum of 1 mM BIPS in tetrachloroethene.

It follows that our calculations quantitatively reproduce the BIPS absorption, with an error of 0.26 eV. If the B3LYP functional is taken into consideration, a dark state results to be the first excited one, as it can be expected by of global hybrid functionals when dealing with extended delocalized electronic systems. If the correct excited state is considered, namely the bright second state, it can be found a HOMO-1 \rightarrow LUMO transition, exhibiting a $\pi\rightarrow\pi^*$ locally excited character, which locates a maximum absorption at 4.15 eV ($f=0.0948$) for the BIPS molecule and a 4.11 eV ($f=0.0828$) for the SPt one, therefore reproducing the experimental absorption band (4.13 eV) with an error of 0.02 eV for the BIPS molecule. Therefore, from the observation that from a computational point of view SPt reproduces BIPS main feature, it seem to be reasonable to focus our attention on SPt to characterize the BIPS open ring reaction.

6.2 The energetic aspects of ring opening reaction: ground and excited state potential energy profiles

Having proven the accuracy of the level of theory used in quantitatively reproducing the minima on the ground state PES, the same approach was applied to describe the ring opening mechanism at the excited state. In order to understand if D_{CT} can actually describe the minimum reaction path and the internal conversion occurring

between S_1 and S_0 excited states, we focused on the analysis of the reactivity of the SPt when excited. In order to get a first flavor of the PES associated to the reaction, a constrained potential energy profile following an ad-hoc defined reaction coordinate was computed on the ground electronic state. In particular, the C_1 -O distance was scanned in the 1.30-2.60 Å range, while relaxing all other degrees of freedom at the B3LYP/6-31+G(d,p) level of theory. In Figure 6.4 they are reported the corresponding ground and vertical excitation energy profiles computed at the TD-CAM-B3LYP/6-31+G(d,p). In all cases the energy of the ground minimum

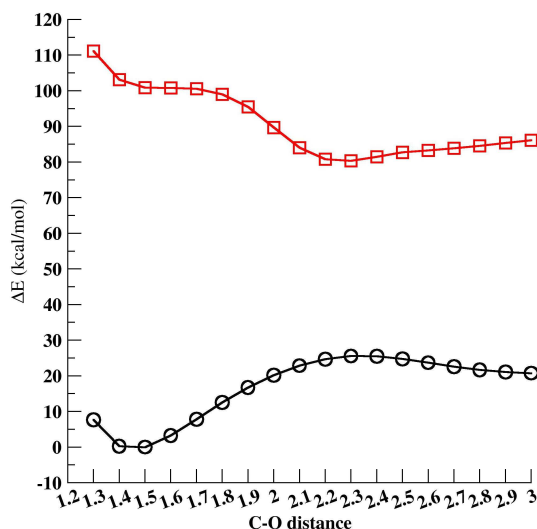


Fig. 6.4: Energetic profiles (S_1 and S_0 , square and circle lines respectively.) computed at the TD-CAM-B3LYP/6-31+G(d,p) level of theory on minimum energy structures obtained at the B3LYP/6-31+G(d,p).

energy structure (the one with the C_1 -O distance equal to 1.5 Å), was set to zero. From these two relative energy profiles it is evident that at the ground state, the reaction does not spontaneously occur with a monotonic energy increase as a function of the C_1 -O distance up to a value of 25 kcal/mol (C_1 -O = 2.0 Å). At the same time,

by vertical TD calculations it can be inferred that in correspondence of $C_1-O = 2.30 \text{ \AA}$ a local minimum is reached with a ΔE about of -20 kcal/mol from the reagent, i.e. the Franck-Condon region in the excited state. If the same kind of analysis is performed by relaxing all degree of freedom except the C_1-O along the S_1 profile at the TD-CAM-B3LYP/6-31+G(d,p) level of theory, it can be obtained the result reported in Figure 6.5. Where it can be observed that at $C_1-O = 2.30 \text{ \AA}$ the ΔE

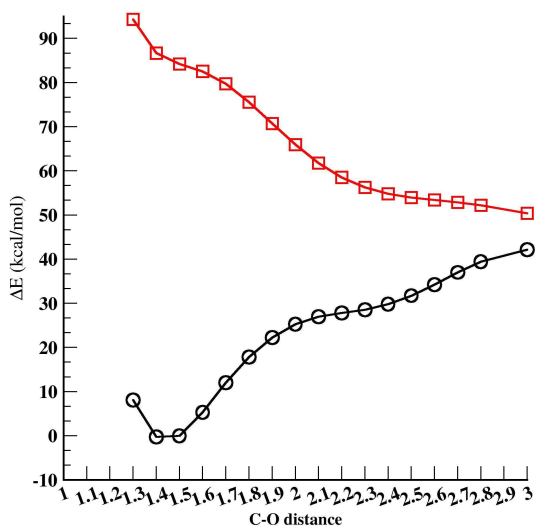


Fig. 6.5: Energetic profiles (S_1 and S_0 , square and circle lines respectively.) computed at the TD-CAM-B3LYP/6-31+G(d,p).

is lowered at about 45 kcal/mol with respect to the Franck-Condon region and an energetic *plateau* is reached.

6.3 2D PESs for the HOOP Valley and OBF path

As described in the previous subsection, the ring opening reaction in the SPt system is a S_1 excited state process. After the absorption event, the reaction seems to follow

an excited state reaction path along the S_1 excited state with no evident barrier to the process.

Recently it has been proposed by Prof. Morokuma [216] that a more pyramidalized C_2 center, namely, an out of plane torsion on the $H(-C_2)$ can provide access to a low energy valley which has been denoted as S_1 -HOOP valley. HOOP valley, in turn, can be differentiated from the one bond flipping mechanism (OBF) path. Therefore the two paths are here investigated at the DFT level of theory. In Figure 6.3 it is reported a 2D S_1 relaxed scan the along the C_1 -O (from 1.40 Å to 2.60 Å) distance and the dihedral angle (τ from 120° to 240°). It can be observed from

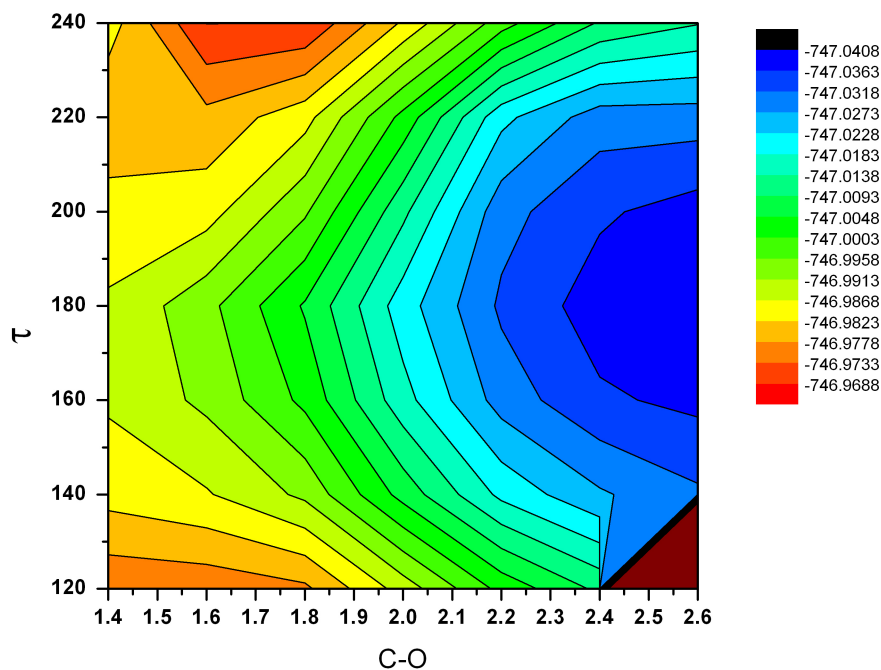


Fig. 6.6: Potential energy surface (in hartree) relaxed on the first excited state (S_1) for the SPT model at the TD-CAM-B3LYP/6-31+G(d,p) level of theory.

analysis of Figure 6.3 that, while no energetic barrier are present for both the OBF

path (which involves no variation of the τ dihedral angle) and for the HOOP-Valley, the DFT picture seems to suggest that, in proximity of the Franck-Condon region a steeper lowering of the energy corresponds to τ dihedral of 180° . Starting from C-O of about 1.40 \AA , no appreciable difference in the energy map is observed for asymmetrical values of τ .

Experiments suggest that, once the SPt molecule get excited on the first excited state, S_1 [217] it will experience a spontaneous $S_1 \rightarrow S_0$ non radiative decay, leading the ring opening process last step take place on the ground state, S_0 .

Prof.Morokuma [216] suggested that the non radiative decay to ground state should occur when the C_1 -O distance assumes values of about 2.00 - 2.20 \AA . It seems to be reasonable that, the lower energy difference between states concurs with a certain similarity between electronic states transition. Assuming that our $S_1 \rightarrow S_0$ non radiative decay could be assimilated the use of electronic density based analysis could be useful in the understanding the complex photochemistry behind this ring opening reaction. Therefore the question is whether through a density based analysis, is possible to describe the non radiative decay between S_1 and S_0 electronic states.

6.4 Analysis of density based indices, D_{CT} , for the $S_1 \rightarrow S_0$ interconversion

From the earlier study of the photochromism of spiropyran molecules, a non planar form on the S_1 surface has been ascribed as a funnel for an $S_1 \rightarrow S_0$ internal conversion (Ernsting chemical physical letter 1989). It is well known that excitation

energy can be dissipated through an internal conversion between electronic states, a non radiative process, that means, through the involvement of vibrational levels if they strongly overlap with electronic levels. Here it is taken into consideration the possibility to exploit an analysis through electronic density based indices to get information on non radiative decay probability. Based on the 2D grid of points previously defined, a scan on the S_1 excited state along the C_1 -O distance and the τ dihedral angle, DCT indices have been evaluated and the DCT surface is reported in Figure 6.4. Starting from a situation of low DCT values, it can be inferred from

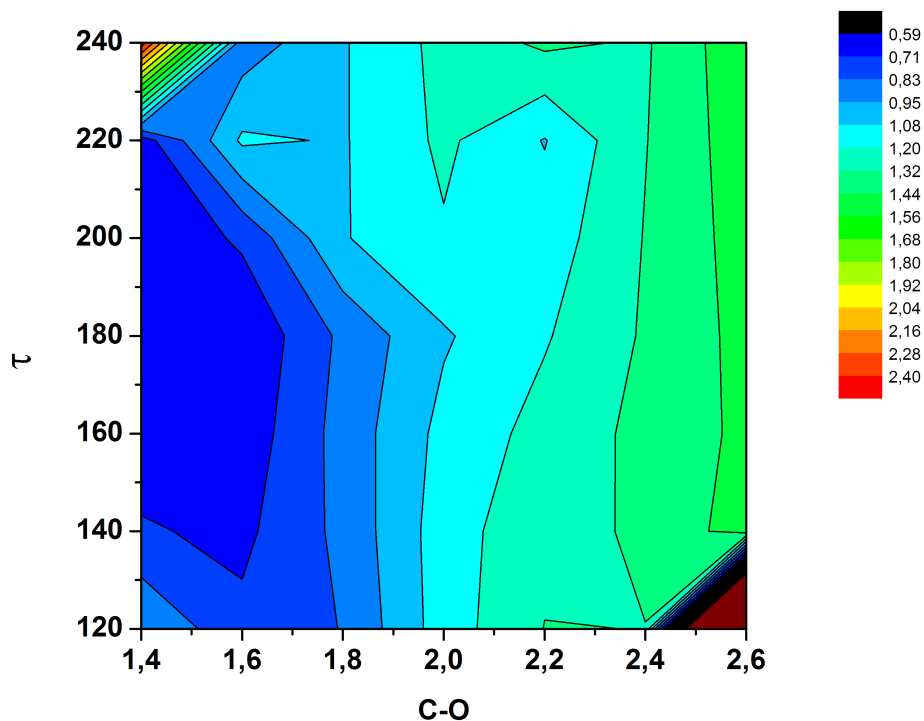


Fig. 6.7: D_{CT} calculated for the first excited state (S_1) on S_1 relaxed geometry for the SPt model.

Figure 6.4 that elongating the a C_1 -O distance a general increasing values can be observed.

Regarding variations along the τ coordinate, the general trend seems to indicate that according to what previously observed with the PES, along first steps of S_1 path, DCT values show a larger gradient when τ dihedral angle assumes 180° value. Moreover an higher DCT value can be observed for the grid point ($C_1-O=1.60 \text{ \AA}$, $\tau= 220^\circ$), which in turn corresponds to higher energetic values observed in Figure 6.4.

A certain degree of correspondence between putative transition states and higher DCT value has been reported in our previous work (Ref. [8]).

However, in last steps (starting from $C_1-O=2.00 \text{ \AA}$) involving a distortion of the τ dihedral angle from the 180° value, an activated HOOP mode path could have a role in the crossing region between the S_1 and S_0 states. As a matter of fact, in correspondence of the grid point ($C_1-O=2.20 \text{ \AA}$, $\tau= 220^\circ$) minimum value of DCT is met.

Starting from these observations, and from the consideration that, in order to let a $S_1 \rightarrow S_0$ conversion taking place two ingredients must concur, namely the lower energetic difference and the higher electronic similarity.

A new index here named intuitive probability, Π has been defined. First of all, this probability depends on how much the two potential energetic surfaces associated to the states involved in the transition are close. Moreover we assume that a similarity between electronic density is well represented by the difference between electronic dipole moment in the two electronic states.

We then define Π as:

$$\Pi = \frac{1}{\Delta E^2 * D_{CT}^2 * q_{CT}^2} \quad (6.1)$$

In Figure 6.4 it is reported Π values over the 2D grid previously defined. From

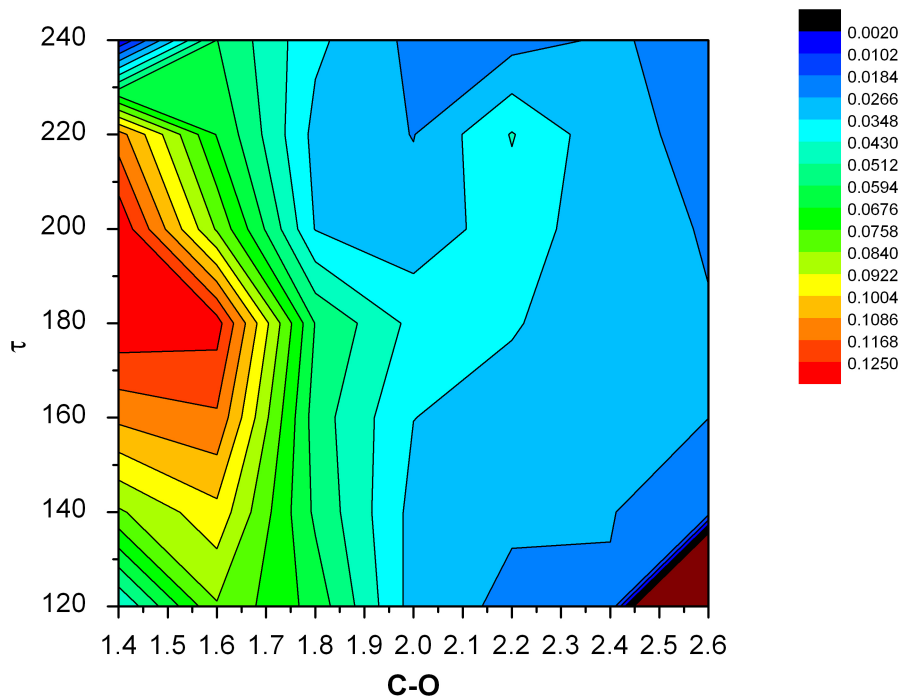


Fig. 6.8: Π descriptor calculated for the first excited state on S_1 relaxed geometry for the SPT model.

inspection of that map it is evident that an hot zone can be individuated, focused around the grid point $C_1-O=1.60 \text{ \AA}$, $\tau=180^\circ$ close to Franck-Condon region. This finding is in a great accordance with the experimental observation [10] that when the BIPS molecule absorbs due to a very efficient internal conversion path to the ground state (around 90%) only a remaining 10% molecules can undergo the ring opening reaction.

Another zone in which Π assumes high values can be individuated around the grid point $C_1-O=2.20 \text{ \AA}$, $\tau=220^\circ$. This finding confirms predictions recently reported by Prof. Morokuma and co-workers [216,218] able to see a narrowing of the S_1/S_0 gap (about 20 kcal/mol) with a C_1-O distance around 2.00-2.20 \AA . Moreover they have individuated the HOOP Valley as a possible radiationless $S_1 \rightarrow S_0$ transition channel.

Conclusions

The understanding of molecular processes triggered by the electronic excitation relies on a proper chemical-physical characterization that can be based on a sound theoretical modeling of the photophysics and the photochemistry. From the more strict point of view of the computational chemistry, this requirement corresponds to a full quantum mechanical description, of the molecular system under study, by which both electrons and nuclei are represented by time-dependent wave-functions. Computational methods provide nowadays a powerful tool to analyse and single out structural, electronic, and environmental factors affecting molecular systems. In the present Ph.D. project, several photo-induced events have been studied by originally proposed computational protocols. Examples of processes have been chosen among not yet understood cases of great importance in photochemistry and photophysics. First, a theoretical model has been developed to obtain spontaneous emission decay rate k_r from excited to ground state ($S_1 \rightarrow S_0$ transition), which is based on the quantum mechanical calculations of energy minimum structures in the fluorescent excited state. When combined with experimental measurements of the fluorescence lifetime, this model can be used to forecast fluorescence quantum yields. This pro-

cedure has been applied to a family of fluorescent dyes, the rhodamine derivatives, leading to results in very good agreement with experimental counterparts. For what regards rhodamines, it was also individuated a non-radiative path of the fluorescence decay, involving a photoinduced electron transfer from the carboxylate group to the xanthene ring. This non radiative decay has been investigated for Rhodamine B and tetramethyl-carboxy Rhodamine in polar solvents. To this aim, the conversion from a bright locally excited toward a dark charge transfer state has been analysed by the support of ad hoc designed density depending parameters. Coming to more challenging examples of charge transfer events, methods based on time-dependent density functional theory have been validated for the description of optically allowed excited states, and have been tested in the case of an excited state proton transfer reaction. Moreover, the efficiency of the various density functionals has been tested in terms of reliability and feasibility when describing a process of proton coupled electron transfer. It has been found that the quality of the description of the evolving electronic density, correlates to the HF percentage in the density functional. This assertion is true in the case of the gas phase but even more in the solvent one, especially when dealing with continuum models. Similar trends have been obtained considering an explicit representation of the solvent. Once the computational methods has been established, it has been possible to analyse in detail the PCET reaction, with particular regard to the description of the overall reaction by adopting different cluster of solvation of the electron donor moiety. ET

has been performed by changing the nature of the electron acceptor. Experimentally known differences in yields of the PCET reaction have been interpreted in terms of different trends of the dipole moment calculated in the two cases along the PT coordinate. Regarding the photoreactivity, an excited state proton transfer reaction between a coumarin dye and a base molecule has been analyzed, and the phototautomerism observed upon irradiation in presence of a high concentration of the base has been disclosed. In particular, an energetical analysis of reagents, products and intermediates of the proton shuttle along a chain of three base molecules clearly showed that the overall driving force of the entire process is the coumarin photo-acidity. Furthermore, the photoacidity of the coumarin has been analyzed in term of electron density based indices and the variation of the pK_a upon excitation. Electron density based indices have also been used to describe possible excited state paths for the excited state reaction. In order to gain a description of the minimum energy paths in term of electron density based indices, a new index, $D_{CT,react}$ has been developed during this thesis, by cumulating in its formulation both the electronic and the nuclear rearrangements. This new parameter resulted to be an effective descriptor of the minimum energy path associated to the ESPT reaction in the coumarin dye. Finally, a non radiative decay affecting the light induced ring-opening reaction of a spiroiran molecule has been analyzed. It resulted that, through an accurate description of the excited state PES and the use of new quantities derived from electron density indices, it is possible to reproduce the ex-

perimental low quantum yield affecting the reaction. Moreover, in accordance with previous high level computational studies it has been observed an involvement of a distortion of a dihedral angle describing an out of plane mode in the excited state path. In conclusion, we have illustrated how the theoretical modeling is a powerful tool to rationalize excited state processes and to propose new insights, spanning from photophysics to photochemistry.

The computational approach, if properly handled, provides a great contribution in the characterization of excited and ground states PESs, that is mandatory when dealing with light induced phenomena.

New theoretical tools can support the understanding of very complex processes, such those involving both electronic and nuclear rearrangements. Therefore, their use is not limited to the theoretical analysis, but may became crucial, to model and interpret phenomena of the everyday life, such those involved in the development of healthcare products and new energy devices.

However, the contribution of the present thesis leaves a large number of questions rather than answers. These question fall in the really intriguing scenarios that are nowadays opened, e.g., how to provide excited state reaction paths? And also, how to take care of the change of multiplicity, namely intersystem crossing processes? Another problem to account for is the influence of solvation affecting the way a molecule relax its degrees of freedom. All this open issues require a modern modelling for a deeper understanding, which theo-computational approaches can afford,

especially when combined with latest improvements in experimental techniques.

Appendix A

Computational details

A.1 Rhodamine dyes: Chapter 2

DFT and TD-DFT methods were exploited to obtain minimum structures in both the ground and excited states for two pyronin systems and nine rhodamine derivatives, namely Pyronin B (PyrB), Pyronin Y (PyrY), RhodB, 5TMR, 6TMR, Rhod6G, 5Rox, 6Rox, Rhodamine 123 (Rhod123), Rhodamine 19 (Rhod19) and Rhodamine 101 (Rhod101).

Grimme [205] correction energy terms were combined with the B3LYP [204] density functional to account for electronic dispersion interactions (DFT-D). Solvent effects were treated by the Conductor-like Polarizable Continuum Model (CPCM) in the linear response formalism. [122, 219] in its equilibrium model [220] when excited state geometry optimization were performed, while non equilibrium model [221] have been employed in any remaining case. A specific solvent was chosen for each xanthene dye to mimic the experimental conditions of both FLIM measurements and lifetime determinations reported in literature. Structure optimizations were performed

at the B3LYP-D/6-31+G(d,p)/CPCM and TD-B3LYP-D/6-31+G(d,p)/CPCM levels of theory for the ground and excited states, respectively. Single point energies for ground and excited states were calculated adopting both B3LYP and long-range corrected [46] CAM-B3LYP [45] functionals. The same levels were exploited to calculate the emission parameters (transition energy, transition electric moment).

All calculations were performed with the Gaussian09 suite of programs, [189] but the D_{CT} index which was evaluated using a in house developed software, as previously described in literature. [11]

A.2 Coumarin dyes: Chapter 3

DFT and time-dependent DFT (TD-DFT) [32] approaches were exploited to investigate ground and excited state potential energy surfaces. The global hybrid B3LYP exchange correlation functional [51] was applied since it has been proven to provide a balanced description of ground and valence excited states' structures, thermochemistry and energetics. [52, 222].

In this context it should be noticed that, although the transition involved in the ESPT reaction is of Charge Transfer type, its through-space character is actually negligible as clearly shown by the difference density plots discussed in this work and by computed density derived diagnostic indices (t [11]) all below the threshold value of 1.7\AA . Furthermore, the variation of the indices seems to be qualitatively insensitive to the functional used, for example when going from B3LYP to range separated hybrids such as CAM-B3LYP. [223] Solvent effects were included by the means of the Polarizable Continuum Model (PCM) in the linear response formalism. [122, 224] When not differently specified, all calculations were performed considering toluene as solvent, in order to allow a direct comparison with the experimental data. [6] Structural optimizations were performed at the B3LYP/6-311G(d,p)/PCM and TD-B3LYP/6-31+G(d,p)/PCM levels of theory for the ground and excited state, respectively. Partial structural optimizations of the first excited state (S_1) were performed, constraining the O-H distance, at the same level of theory (that is TD-B3LYP/6-31+G(d,p)/PCM). This level of theory was also applied to construct a

bi-dimensional (S_1) excited state Potential Energy Surface (PES) by performing a series of constrained optimizations on O-H and O-N distances.

In the case of the dye in presence of three base molecules, structural optimizations were performed at the B3LYP/6-31+G(d,p)/PCM and TD-B3LYP/6-31+G(d,p)/PCM levels of theory for the ground and excited state, respectively. Additionally, vertical excited state energies were computed at TD-CAM-B3LYP/6-31+G(d,p)/PCM level of theory. For all TD-DFT calculations at least three excited states were kept, the first one being that of interest.

All calculations have been performed using the Gaussian09 suite of programs, including the ground and excited state densities, computed using the cubegen utility provided in Gaussian Package. Grids of electronic densities are necessary for indices calculations, and were evaluated taking care, when needed, to chose a consistent grid definition and molecular orientation, namely shifting the center of mass and rotating the molecular axis in order to maximize the overlap between ground and excited state structures. [189]

A.3 PCET reaction: Chapter 4

DFT and TD-DFT were applied to model ground and excited state potential energy surfaces, respectively. When not differently stated, the global hybrid exchange correlation functional PBE0 [184] was adopted to solve the electronic problem. Bulk solvent effects were included by the means of the latest implementation of the polarizable continuum model (PCM) named as CPCM [178, 179]. Single points calculations have been performed at PBE0/6-31+G(d,p)/CPCM, and TD-PBE0/6-31+G(d,p)/CPCM level of theory, respectively for the ground and excited state. All the calculations were performed by the Gaussian suite of programs. [189]

A.4 Spyropiran : Chapter 6

DFT and time-dependent DFT (TD-DFT) [32] approaches were exploited to investigate ground and excited state potential energy surfaces. The global hybrid B3LYP exchange correlation functional [51] was applied since it has been proven to provide a balanced description of ground and valence excited states structures, thermochemistry and energetics. [52, 222]

Partial structural optimizations of the ground state (S_0) were performed, constraining the C₁-O distance, were performed at the B3LYP/6-31+G(d,p) levels of theory, while at the first excited state energies were computed vertically with the Handy and coworkers long range corrected version of B3LYP, CAM-B3LYP [47] at the TD-CAM-B3LYP/6-31+G(d,p) level of theory.

This latter level of theory was also applied to construct a bi-dimensional (S_1) excited state Potential Energy Surface (PES) by performing a series of constrained optimizations on C₁-O distance and of the τ dihedral angle, i.e. the angle defined by H(C2)-C2-C1-C3 atoms labeled in Fig.6.1 For all TD-DFT calculations at least four states were kept, the first or the second one being that of interest. All calculations have been performed using the Gaussian09 suite of programs, including the ground and excited state densities, computed using the cubegen utility provided in Gaussian Package. [189]

Bibliography

- [1] N. J. Turro, V. Ramamurthy, and J. C. Scaiano, *Principles of molecular photochemistry: an introduction* (University science books, 2009).
- [2] W. Koch and M. Holthausen, *A chemist's guide to density functional theory, 2000* (1989).
- [3] M. Savarese, A. Aliberti, I. De Santo, E. Battista, F. Causa, P. Netti, and N. Rega, *J. Phys. Chem. A* (2012).
- [4] A. P. Demchenko, K.-C. Tang, and P.-T. Chou, *Chem. Soc. Rev.* **42** (3), 1379 (2013).
- [5] S. Hammes-Schiffer, *Proc. Natl. Acad. Sci. USA* **108** (21), 8531 (2011).
- [6] B. C. Westlake, J. J. Paul, S. E. Bettis, S. D. Hampton, B. P. Mehl, T. J. Meyer, and J. M. Papanikolas, *J. Phys. Chem. B* **116** (51), 14886 (2012).
- [7] M. Savarese, N. Rega, P. A. Netti, C. Adamo, and I. Ciofini, *Physical Chemistry Chemical Physics* (2014).
- [8] M. Savarese, P. A. Netti, C. Adamo, N. Rega, and I. Ciofini, *The Journal of Physical Chemistry B* **117** (50), 16165 (2013).
- [9] B. Giese, M. Wang, J. Gao, M. Stoltz, P. Mueller, M. Graber *et al.*, *ChemInform* **40** (31) (2009).
- [10] M. Rini, A.-K. Holm, E. T. Nibbering, and H. Fidler, *Journal of the American Chemical Society* **125** (10), 3028 (2003).
- [11] T. Le Bahers, C. Adamo, and I. Ciofini, *J. Chem. Theory Comput.* **7** (8), 2498 (2011).
- [12] B. S.E. and H. N.K., *A useful guide to the terminology of photochemistry* (Applied Chemistry, 1988).
- [13] R. G. Pearson, *Symmetry rules for chemical reactions: orbital topology and elementary processes* (Wiley New York, 1976).

- [14] C. Moser, J. Keske, K. Warncke, R. Farid, P. Dutton *et al.*, *Nature* **355** (6363), 796 (1992).
- [15] K.-L. Han and G.-J. Zhao, *Hydrogen bonding and transfer in the excited state* (Wiley Online Library, 2011).
- [16] T. Förster, *Physik. Chem* **54** (42), 531 (1950).
- [17] A. Weller, *z. Elektrochem* **56**, 662 (1952).
- [18] S. Webb, S. W. Yeh, L. A. Philips, M. Tolbert, and J. Clark, *Journal of the American Chemical Society* **106** (23), 7286 (1984).
- [19] A. Part and S. M. Sensing .
- [20] E. Sproviero, J. Gascón, J. McEvoy, G. Brudvig, and V. Batista, *Journal of the American Chemical Society* **130** (21), 6728 (2008).
- [21] P. Hohenberg, W. Kohn *et al.*, *Phys. Rev* **136** (3B), B864 (1964).
- [22] W. Kohn, L. Sham *et al.*, *Phys. Rev* **140** (4A), A1133 (1965).
- [23] J. P. Perdew and A. Zunger, *Physical Review B* **23** (10), 5048 (1981).
- [24] P. Mori-Sánchez, A. J. Cohen, and W. Yang, *The Journal of chemical physics* **125** (20), 201102 (2006).
- [25] A. Ruzsinszky, J. P. Perdew, G. I. Csonka, O. A. Vydrov, and G. E. Scuseria, *The Journal of chemical physics* **125** (19), 194112 (2006).
- [26] A. J. Cohen, P. Mori-Sánchez, and W. Yang, *Science* **321** (5890), 792 (2008).
- [27] A. Savin, *Theoretical and computational chemistry* **4**, 327 (1996).
- [28] M. Casida, C. Jamorski, K. Casida, and D. Salahub, *The Journal of Chemical Physics* **108**, 4439 (1998).
- [29] R. Stratmann, G. Scuseria, and M. Frisch, *The Journal of Chemical Physics* **109**, 8218 (1998).
- [30] C. Carillie and A. R.D., *Chemical Physics Letters* **308**, 249 (1999).
- [31] C. Carillie and A. R.D., *Chemical Physics Letters* **317**, 159 (2000).
- [32] E. Runge and E. K. Gross, *Physical Review Letters* **52** (12), 997 (1984).
- [33] S. F. Sousa, P. A. Fernandes, and M. J. Ramos, *The Journal of Physical Chemistry A* **111** (42), 10439 (2007).

- [34] N. E. Schultz, Y. Zhao, and D. G. Truhlar, *The Journal of Physical Chemistry A* **109** (49), 11127 (2005).
- [35] Y. Zhao and D. G. Truhlar, *The Journal of Physical Chemistry A* **108** (33), 6908 (2004).
- [36] Y. Zhao and D. G. Truhlar, *The Journal of Physical Chemistry A* **109** (25), 5656 (2005).
- [37] Y. Zhao and D. G. Truhlar, *The Journal of chemical physics* **125**, 194101 (2006).
- [38] Y. Zhao and D. G. Truhlar, *The Journal of Physical Chemistry A* **110** (35), 10478 (2006).
- [39] Y. Zhao, O. Tishchenko, and D. G. Truhlar, *The Journal of Physical Chemistry B* **109** (41), 19046 (2005).
- [40] G. F. Mangiatordi, E. Bremond, and C. Adamo, *Journal of Chemical Theory and Computation* **8** (9), 3082 (2012).
- [41] Y. Zhao and D. G. Truhlar, *Journal of Chemical Theory and Computation* **1** (3), 415 (2005).
- [42] A. Dreuw and M. Head-Gordon, *Chem. Rev.* **105**, 4009 (2005).
- [43] F. Santoro, V. Barone, and R. Improta, *J. Am. Chem. Soc.* **131**, 15232 (2009).
- [44] L. Künnle, *Zeitschrift für Physikalische Chemie* **204** (Part_1_2), 263 (1998).
- [45] T. Yanai, D. P. Tew, and N. C. Handy, *Chem. Phys. Lett.* **393**, 51 (2004).
- [46] Y. Tawada, T. Tsuneda, S. Yanagisawa, T. Yanai, and K. Hirao, *J. Chem. Phys.* **120**, 8425 (2004).
- [47] J. M. Winne, S. Catak, M. Waroquier, and V. Van.Speybroeck, *Angew. Chem. Int. Ed.* **50** (50), 11990 (2011).
- [48] O. A. Vydrov, J. Heyd, A. V. Krukau, and G. E. Scuseria, *J. Chem. Phys.* **125** (7), 074106 (2006).
- [49] J.-D. Chai and M. Head-Gordon, *The Journal of Chemical Physics* **128** (8), 084106 (2008).
- [50] T. Yanai, D. Tew, and N. Handy, *Chemical Physics Letters* **393** (1-3), 51 (2004).
- [51] A. D. Becke, *J. Chem. Phys.* **98**, 5648 (1993).

- [52] D. Jacquemin, V. Wathelet, E. A. Perpète, and C. Adamo, *Journal of Chemical Theory and Computation* **5** (9), 2420 (2009).
- [53] M. Schreiber, M. R. Silva-Junior, S. P. Sauer, and W. Thiel, *The Journal of chemical physics* **128** (13), 134110 (2008).
- [54] I. Ciofini, T. Le Bahers, C. Adamo, F. Odobel, and D. Jacquemin, *J. Phys. Chem. C* **116** (22), 11946 (2012).
- [55] D. Jacquemin, T. Le Bahers, C. Adamo, and I. Ciofini, *Phys. Chem. Chem. Phys.* **14** (16), 5383 (2012).
- [56] F. Labat, I. Ciofini, and C. Adamo, *J. Mater. Chem.* **22** (24), 12205 (2012).
- [57] J. Goodisman, *Diatomic Interaction Potential Theory: Fundamentals*, vol. 1 (Academic Press, 1973).
- [58] J. Franck and E. Dymond, *Transactions of the Faraday Society* **21** (February), 536 (1926).
- [59] E. U. Condon, *Physical Review* **32** (6), 858 (1928).
- [60] N. Turro, *Modern molecular photochemistry* (Univ Science Books, 1991).
- [61] R. C. Hilborn, *American Journal of Physics* **50**, 982 (1982).
- [62] M. Svensson, S. Humbel, R. D. Froese, T. Matsubara, S. Sieber, and K. Morokuma, *The Journal of Physical Chemistry* **100** (50), 19357 (1996).
- [63] H. Schlegel, J. Millam, S. Iyengar, G. Voth, A. Daniels, G. Scuseria, and M. Frisch, *J. Chem. Phys.* **114**, 9758 (2001).
- [64] H. Schlegel, S. Iyengar, X. Li, J. Millam, G. Voth, G. Scuseria, and M. Frisch, *J. Chem. Phys.* **117**, 8694 (2002).
- [65] S. Iyengar, H. Schlegel, J. Millam, G. Voth, G. Scuseria, and M. Frisch, *J. Chem. Phys.* **115**, 10291 (2001).
- [66] S. Iyengar, H. Schlegel, G. Voth, J. Millam, G. Scuseria, and M. Frisch, *Israel journal of chemistry* **42** (2-3), 191 (2002).
- [67] N. Yapici, S. Jockusch, A. Moscatelli, S. Mandalapu, Y. Itagaki, D. Bates, S. Wiseman, K. Gibson, N. Turro, and L. Bi, *Organic Letters* (2012).
- [68] M. Kumar, N. Kumar, V. Bhalla, P. Sharma, and T. Kaur, *Organic Letters* (2012).

- [69] Z. Yang, M. She, B. Yin, J. Cui, Y. Zhang, W. Sun, J. Li, and Z. Shi, *The Journal of Organic Chemistry* (2012).
- [70] Y. Koide, Y. Urano, K. Hanaoka, W. Piao, M. Kusakabe, N. Saito, T. Terai, T. Okabe, and T. Nagano, *Journal of the American Chemical Society* (2012).
- [71] M. Beija, C. Afonso, and J. Martinho, *Chem. Soc. Rev.* **38**, 2410 (2009).
- [72] Y. Koide, Y. Urano, K. Hanaoka, T. Terai, and T. Nagano, *ACS Chem. Biol.* **6**, 600 (2011).
- [73] D. R. Larson, H. Ow, H. D. Vishwasrao, A. A. Heikal, U. Wiesner, and W. W. Webb, *Chem. Mat.* **20**, 2677 (2008).
- [74] K. Chingin, R. M. Balabin, V. Frankevich, H. Chen, K. Barylyuk, R. Nieckarz, A. Fedorov, and R. Zenobi, *Phys. Chem. Chem. Phys.* **12**, 14121 (2010).
- [75] K. Chingin, R. M. Balabin, K. Barylyuk, H. Chen, V. Frankevich, and R. Zenobi, *Phys. Chem. Chem. Phys.* **12**, 11710 (2010).
- [76] E. Kato and T. Murakami, *Polymer Gels and Networks* **6** (3-4), 179 (1998).
- [77] F. L. Arbeloa and K. K. Rohatgi-Mukherjee, *Chem. Phys. Lett.* **129**, 607 (1986).
- [78] F. L. Arbeloa and I. U. Aguirresacona, *Chem. Phys.* **130**, 371 (1989).
- [79] A. Penzkofer and M. Falkenstein, *Opt. Quant. Electron* **10**, 399 (1978).
- [80] M. Snare, F. Treloar, K. Ghiggino, and P. Thistlethwaite, *J. Photochem.* **18** (4), 335 (1982).
- [81] T. Karstens and K. Kobs, *J. Phys. Chem.* **84**, 1871 (1980).
- [82] K. H. Drexhage, *Top. Appl. Phys.* **1**, 144 (1973).
- [83] K. Drexhage, *J. Res. Natl. Bur. Stand* **80**, 421 (1976).
- [84] K. Drexhage, *Dye lasers* pp. 155–200 (1973).
- [85] M. W. Vogel, W. Rettig, R. Sens, and K. H. Drexhage, *Chem. Phys. Lett.* **147**, 452 (1988).
- [86] Z. Grabowski, K. Rotkiewicz, A. Siemiarczuk, D. J. Cowley, and W. Baumann, *Nouv. J. Chim.* **3**, 443 (1979).
- [87] K. A. Zachariasse, T. von der Haar, A. Hebecker, U. Leinhos, and W. KUhnle, *Pure Appl. Chem.* **65**, 1745 (1993).

- [88] T. von der Haar, A. Hebecker, Y. Il'ichev, Y. B. Jiang, W. Ktihle, and K. A. Zachariasse, *Recl. Trav. Chim. Pays-Bas* **114**, 430 (1995).
- [89] A. Pedone, G. Prampolini, S. Monti, and V. Barone, *Chemistry of Materials* **23**, 5016 (2011).
- [90] V. Barone, J. Bloino, S. Monti, A. Pedone, and G. Prampolini, *Phys. Chem. Chem. Phys.* **13**, 2160 (2011).
- [91] Z. R. Grabowski, K. Rotkiewicz, and W. Rettig, *Chem. Rev.* **103**, 3899 (2003).
- [92] T. Miura, Y. Urano, K. Tanaka, T. Nagano, K. Ohkubo, and S. Fukuzumi, *J. Am. Chem. Soc.* **125** (28), 8666 (2003).
- [93] Y. Koide, Y. Urano, K. Hanaoka, T. Terai, and T. Nagano, *Journal of the American Chemical Society* (2011).
- [94] X.-F. Zhang, Y. Zhang, and L. Liu, *Journal of Luminescence* **145**, 448 (2014).
- [95] L.-l. Jiang, W.-l. Liu, Y.-f. Song, X. He, Y. Wang, C. Wang, H.-l. Wu, F. Yang, and Y.-q. Yang, *Chemical Physics* (2013).
- [96] G. García, C. Adamo, and I. Ciofini, *Physical Chemistry Chemical Physics* **15** (46), 20210 (2013).
- [97] J. B. Prieto, F. L. Arbeloa, V. M. Martinez, T. A. Lopez, and I. L. Arbeloa, *Phys. Chem. Chem. Phys.* **6**, 4247 (2004).
- [98] B. Lounis and M. Orrit, *Rep. Prog. Phys.* **68**, 1129 (2005).
- [99] G. Nienhuis and C. T. J. Alkemade, *Physica B+C* **81**, 181 (1976).
- [100] S. J. Strickler and R. A. Berg, *J. Chem. Phys.* **37**, 814 (1962).
- [101] D. Adhikesavalu, D. Mastropaolo, A. Camerman, and N. Camerman, *Acta Crystallographica Section C: Crystal Structure Communications* **57** (5), 657 (2001).
- [102] H. Watanabe, N. Hayazawa, Y. Inouye, and S. Kawata, *J. Phys. Chem. B* **109** (11), 5012 (2005).
- [103] A. Pedone, J. Bloino, S. Monti, G. Prampolini, and V. Barone, *Phys. Chem. Chem. Phys.* **12** (4), 1000 (2010).
- [104] N. Çelebi, M. ArIk, and Y. Onganer, *J. Lumin.* **126** (1), 103 (2007).
- [105] R. Kubin and A. Fletcher, *J. Lumin.* **27** (4), 455 (1983).

- [106] A. Glazer and R. Mathies, *Current opinion in biotechnology* **8** (1), 94 (1997).
- [107] M. ArIk and Y. Onganer, *Chem. Phys. Lett.* **375** (1-2), 126 (2003).
- [108] Eastman Laboratory Chemicals Catalog No. 55 (1993-94), Fisher Scientific.
- [109] Birge, R. R. (1987) Kodak Laser Dyes, Kodak publication JJ-169.
- [110] D. Jacquemin, E. Perpète, O. Vydrov, G. Scuseria, and C. Adamo, *The Journal of chemical physics* **127**, 094102 (2007).
- [111] D. Jacquemin, E. Perpète, G. Scalmani, M. Frisch, R. Kobayashi, and C. Adamo, *The Journal of chemical physics* **126**, 144105 (2007).
- [112] J. Guthmuller and B. Champagne, *J. Phys. Chem. A* **112** (14), 3215 (2008).
- [113] D. Setiawan, A. Kazaryan, M. Martoprawiro, and M. Filatov, *Physical Chemistry Chemical Physics* **12** (37), 11238 (2010).
- [114] B. Reija, W. Al-Soufi, M. Novo, and J. Tato, *J. Phys. Chem. B* **109** (4), 1364 (2005).
- [115] A. Ribou, J. Vigo, and J. Salmon, *J. Photochem. Photobiol. A* **151** (1-3), 49 (2002).
- [116] J. Clark, P. Miller, and G. Rumbles, *J. Phys. Chem. A* **102** (24), 4428 (1998).
- [117] A. Deshpande and U. Kumar, *J. Lumin.* **128** (7), 1121 (2008).
- [118] G. Vàmosi, C. Gohlke, and R. M. Clegg, *Biophys. J.* **71**, 972 (1996).
- [119] H. Kuhn, *Angew. Chem.* **71**, 93 (1959).
- [120] [Http://www.sigmaaldrich.com/](http://www.sigmaaldrich.com/).
- [121] R. Improta, *Phys. Chem. Chem. Phys.* **10**, 2656 (2008).
- [122] S. Corni, R. Cammi, B. Mennucci, and J. Tomasi, *J. Chem. Phys.* **123**, 134512 (2005).
- [123] C. J. Gagliardi, B. C. Westlake, C. A. Kent, J. J. Paul, J. M. Papanikolas, and T. J. Meyer, *Coord. Chem. Rev.* **254** (21), 2459 (2010).
- [124] C.-C. Hsieh, C.-M. Jiang, and P.-T. Chou, *Acc. Chem. Res.* **43** (10), 1364 (2010).
- [125] S. Hammes-Schiffer, *J. Phys. Chem. Lett.* **2** (12), 1410 (2011).
- [126] O. S. Wenger, *Accounts of Chemical Research* **46** (7), 1517 (2013).

- [127] W. Domcke and A. L. Sobolewski, *Science* **302** (5651), 1693 (2003).
- [128] B. C. Westlake, M. K. Brennaman, J. J. Concepcion, J. J. Paul, S. E. Bettis, S. D. Hampton, S. A. Miller, N. V. Lebedeva, M. D. Forbes, A. M. Moran, T. J. Meyer, and P. J. M., *Proc. Natl. Acad. Sci. USA* **108** (21), 8554 (2011).
- [129] C. Fang, R. R. Frontiera, R. Tran, and R. A. Mathies, *Nature* **462** (7270), 200 (2009).
- [130] F. Han, W. Liu, and C. Fang, *Chemical Physics* [**Online early access**] (Published Online : 21 March 2013).
- [131] J. H. Skone, A. V. Soudackov, and S. Hammes-Schiffer, *Journal of the American Chemical Society* **128** (51), 16655 (2006). PMID: 17177415.
- [132] G. A. DiLabio and E. R. Johnson, *J. Am. Chem. Soc.* **129** (19), 6199 (2007).
- [133] S. Hammes-Schiffer and A. A. Stuchebrukhov, *Chem. Rev.* **110** (12), 6939 (2010).
- [134] A. Sirjoosingh and S. Hammes-Schiffer, *J. Phys. Chem. A* **115** (11), 2367 (2011).
- [135] A. Sirjoosingh, M. V. Pak, and S. Hammes-Schiffer, *J. Chem. Theory Comput.* **7** (9), 2689 (2011).
- [136] A. Sirjoosingh and S. Hammes-Schiffer, *J. Chem. Theory Comput.* **7** (9), 2831 (2011).
- [137] T. Inagaki, T. Yamamoto, and S. Kato, *Journal of Computational Chemistry* **32** (14), 3081 (2011).
- [138] S. Hammes-Schiffer, *Energ. Environ.* **5** (7), 7696 (2012).
- [139] J. S. Kretchmer and T. F. Miller III, *J. Chem. Phys.* **138**, 134109 (2013).
- [140] C. Ko, B. H. Solis, A. V. Soudackov, and S. Hammes-Schiffer, *J. Phys. Chem. B* (2012).
- [141] J. J. Concepcion, M. K. Brennaman, J. R. Deyton, N. V. Lebedeva, M. D. Forbes, J. M. Papanikolas, and T. J. Meyer, *J. Am. Chem. Soc.* **129** (22), 6968 (2007).
- [142] J. L. Dempsey, J. R. Winkler, and H. B. Gray, *J. Am. Chem. Soc.* **132** (47), 16774 (2010).
- [143] T. Le Bahers, C. Adamo, and I. Ciofini, *Chem. Phys. Lett.* **472** (1), 30 (2009).

- [144] E. Bremond, M. Alberto, N. Russo, G. Ricci, I. Ciofini, and C. Adamo, *Phys. Chem. Chem. Phys.* (Published Online : 21 February 2013).
- [145] C. Lee, C. Sosa, and J. J. Novoa, *J. Chem. Phys.* **103**, 4360 (1995).
- [146] D. J. Tozer, C. Lee, and G. Fitzgerald, *J. Chem. Phys.* **104**, 5555 (1996).
- [147] N. Rega, S. S. Iyengar, G. A. Voth, H. B. Schlegel, T. Vreven, and M. J. Frisch, *J. Phys. Chem. B* **108** (13), 4210 (2004).
- [148] C. W. Hoganson and G. T. Babcock, *Science* **277** (5334), 1953 (1997).
- [149] J. B. Howard and D. C. Rees, *Proc. Natl. Acad. Sci. USA* **103** (46), 17088 (2006).
- [150] D. R. Weinberg, C. J. Gagliardi, J. F. Hull, C. F. Murphy, C. A. Kent, B. C. Westlake, A. Paul, D. H. Ess, D. G. McCafferty, and T. J. Meyer, *Chem. Rev.* **112** (7), 4016 (2012).
- [151] M. Meyer and J. Klinman, *J. Chem. Phys.* **319** (1), 283 (2005).
- [152] B. Li, J. Zhao, K. Onda, K. Jordan, J. Yang, and H. Petek, *Science* **311** (5766), 1436 (2006).
- [153] T. Meyer, M. Huynh, and H. Thorp, *Angew. Chem. Int. Ed.* **46** (28), 5284 (2007).
- [154] C.-C. Hsieh, Y.-M. Cheng, C.-J. Hsu, K.-Y. Chen, and P.-T. Chou, *J. Phys. Chem. A* **112** (36), 8323 (2008).
- [155] B. H. Solis and S. Hammes-Schiffer, *Inorg. Chem.* **50** (21), 11252 (2011).
- [156] L. Hammarström and S. Styring, *Energ. Environ.* **4** (7), 2379 (2011).
- [157] J. N. Schrauben, M. Cattaneo, T. C. Day, A. L. Tenderholt, and J. M. Mayer, *J. Am. Chem. Soc.* **134** (40), 16635 (2012).
- [158] R. N. Barnett, J. Joseph, U. Landman, and G. B. Schuster, *J. Am. Chem. Soc.* **135** (10), 3904 (2013).
- [159] B. Giese, *Acc. Chem. Res.* **33** (9), 631 (2000).
- [160] M. Cordes and B. Giese, *Chem. Soc. Rev.* **38** (4), 892 (2009).
- [161] M. T. Koper, *Phys. Chem. Chem. Phys.* **15** (5), 1399 (2013).
- [162] J. M. Mayer and I. J. Rhile, *Biochimica et Biophysica Acta (BBA)-Bioenergetics* **1655**, 51 (2004).

- [163] J. B. Issa, K. Krogh-Jespersen, and S. S. Isied, *The Journal of Physical Chemistry C* **114** (48), 20809 (2010).
- [164] M. Cordes, O. Jacques, A. Köttgen, C. Jasper, H. Boudebous, and B. Giese, *Advanced Synthesis & Catalysis* **350** (7-8), 1053 (2008).
- [165] M. Cordes, A. Köttgen, C. Jasper, O. Jacques, H. Boudebous, and B. Giese, *Angewandte Chemie International Edition* **47** (18), 3461 (2008).
- [166] M. Wang, J. Gao, P. Müller, and B. Giese, *Angew. Chem. Int. Ed.* **48** (23), 4232 (2009).
- [167] H. Zhong and H. A. Carlson, *Journal of Chemical Theory and Computation* **2** (2), 342 (2006).
- [168] W. Jorgensen, J. Chandrasekhar, J. Madura, R. Impey, and M. Klein, *The Journal of chemical physics* **79**, 926 (1983).
- [169] G. Brancato, N. Rega, and V. Barone, *The Journal of chemical physics* **128**, 144501 (2008).
- [170] G. Brancato, V. Barone, and N. Rega, *Theoretical Chemistry Accounts: Theory, Computation, and Modeling (Theoretica Chimica Acta)* **117** (5), 1001 (2007).
- [171] G. Brancato, N. Rega, and V. Barone, *The Journal of chemical physics* **125**, 164515 (2006).
- [172] V. Barone, L. Orlandini, and C. Adamo, *The Journal of Physical Chemistry* **98** (50), 13185 (1994).
- [173] V. Barone, L. Orlandini, and C. Adamo, *International Journal of Quantum Chemistry* **56** (6), 697 (1995).
- [174] V. Barone and C. Adamo, *The Journal of chemical physics* **105**, 11007 (1996).
- [175] S. Sadhukhan, D. Muñoz, C. Adamo, and G. Scuseria, *Chemical physics letters* **306** (1), 83 (1999).
- [176] Q. Zhang, R. Bell, and T. Truong, *The Journal of Physical Chemistry* **99** (2), 592 (1995).
- [177] H. Chermette, H. Razafinjanahary, and L. Carrion, *The Journal of chemical physics* **107**, 10643 (1997).
- [178] M. Cossi, N. Rega, G. Scalmani, and V. Barone, *J. Comp. Chem.* **24**, 669 (2003).

- [179] V. Barone and M. Cossi, *J. Phys. Chem. A* **102** (11), 1995 (1998).
- [180] A. Becke, *Physical Review A* **38** (6), 3098 (1988).
- [181] Y. W. P. R. G. Lee C., *Phys. Rev. B* **37**, 785 (1988).
- [182] S. Grimme, *Journal of Computational Chemistry* **27** (15), 1787 (2006).
- [183] A. D. Becke, *The Journal of Chemical Physics* **98** (7), 5648 (1993).
- [184] C. Adamo and V. Barone, *The Journal of Chemical Physics* **110** (13), 6158 (1999).
- [185] Y. Zhao and D. Truhlar, *Theoretical Chemistry Accounts* **120**, 215 (2008).
- [186] A. D. Becke, *The Journal of Chemical Physics* **98** (2), 1372 (1993).
- [187] C. Mollerr and M. S. Plesset, *Phys. Rev.* **46**, 618 (1934).
- [188] V. N. Staroverov, G. E. Scuseria, J. Tao, and J. P. Perdew, *The Journal of chemical physics* **119**, 12129 (2003).
- [189] M. J. Frisch, G. W. Trucks, H. B. Schlegel, G. E. Scuseria, M. A. Robb, J. R. Cheeseman, G. Scalmani, V. Barone, B. Mennucci, G. A. Petersson, H. Nakatsuji, M. Caricato, X. Li, H. P. Hratchian, A. F. Izmaylov, J. Bloino, G. Zheng, J. L. Sonnenberg, M. Hada, M. Ehara, K. Toyota, R. Fukuda, J. Hasegawa, M. Ishida, T. Nakajima, Y. Honda, O. Kitao, H. Nakai, T. Vreven, J. A. Montgomery, Jr., J. E. Peralta, F. Ogliaro, M. Bearpark, J. J. Heyd, E. Brothers, K. N. Kudin, V. N. Staroverov, R. Kobayashi, J. Normand, K. Raghavachari, A. Rendell, J. C. Burant, S. S. Iyengar, J. Tomasi, M. Cossi, N. Rega, J. M. Millam, M. Klene, J. E. Knox, J. B. Cross, V. Bakken, C. Adamo, J. Jaramillo, R. Gomperts, R. E. Stratmann, O. Yazyev, A. J. Austin, R. Cammi, C. Pomelli, J. W. Ochterski, R. L. Martin, K. Morokuma, V. G. Zakrzewski, G. A. Voth, P. Salvador, J. J. Dannenberg, S. Dapprich, A. D. Daniels, . Farkas, J. B. Foresman, J. V. Ortiz, J. Cioslowski, and D. J. Fox, *Gaussian 09 Revision A.2*. Gaussian Inc. Wallingford CT 2009.
- [190] S. Dapprich, I. Komáromi, K. S. Byun, K. Morokuma, and M. J. Frisch, *Journal of Molecular Structure: THEOCHEM* **461**, 1 (1999).
- [191] H. Chermette, I. Ciofini, F. Mariotti, and C. Daul, *The Journal of Chemical Physics* **114**, 1447 (2001).
- [192] Y. Zhao, B. J. Lynch, and D. G. Truhlar, *The Journal of Physical Chemistry A* **108** (14), 2715 (2004).
- [193] Y. Zhang and W. Yang, *The Journal of chemical physics* **109**, 2604 (1998).

- [194] M. Lundberg and P. E. Siegbahn, *The Journal of chemical physics* **122**, 224103 (2005).
- [195] A. J. Johansson, M. R. Blomberg, and P. E. Siegbahn, *The Journal of chemical physics* **129**, 154301 (2008).
- [196] É. Brémond, D. Pilard, I. Ciofini, H. Chermette, C. Adamo, and P. Cortona, *Theoretical Chemistry Accounts* **131** (3), 1 (2012).
- [197] C. Lee, W. Yang, and R. Parr, *Physical Review B* **37** (2), 785 (1988).
- [198] J. Perdew, K. Burke, and M. Ernzerhof, *Physical Review Letters* **77** (18), 3865 (1996).
- [199] T. Van Voorhis and G. E. Scuseria, *The Journal of chemical physics* **109** (2), 400 (1998).
- [200] P. J. Wilson, T. J. Bradley, and D. J. Tozer, *The Journal of Chemical Physics* **115** (20), 9233 (2001).
- [201] C. Adamo and V. Barone, *Chemical Physics Letters* **274** (1), 242 (1997).
- [202] A. D. Boese and J. M. Martin, *The Journal of chemical physics* **121** (8), 3405 (2004).
- [203] X. Xu and W. A. Goddard, *Proceedings of the National Academy of Sciences of the United States of America* **101** (9), 2673 (2004).
- [204] A. D. Becke, *J. Chem. Phys.* **98**, 5648 (1993).
- [205] T. Schwabe and S. Grimme, *Physical Chemistry Chemical Physics* **9** (26), 3397 (2007).
- [206] C. Adamo and V. Barone, *The Journal of Chemical Physics* **108** (2), 664 (1998).
- [207] B. J. Lynch, P. L. Fast, M. Harris, and D. G. Truhlar, *The Journal of Physical Chemistry A* **104** (21), 4811 (2000).
- [208] Y. Zhao and D. G. Truhlar, *The Journal of Physical Chemistry A* **110** (15), 5121 (2006).
- [209] H. Iikura, T. Tsuneda, T. Yanai, and K. Hirao, *The Journal of Chemical Physics* **115** (8), 3540 (2001).
- [210] O. Vydrov, J. Heyd, A. Krukau, and G. Scuseria, *The Journal of chemical physics* **125**, 074106 (2006).

- [211] O. Vydrov and G. Scuseria, *The Journal of chemical physics* **125**, 234109 (2006).
- [212] J.-D. Chai and M. Head-Gordon, *Physical Chemistry Chemical Physics* **10** (44), 6615 (2008).
- [213] J.-D. Chai and M. Head-Gordon, *The Journal of chemical physics* **128** (8), 084106 (2008).
- [214] E. Brémond and C. Adamo, *The Journal of chemical physics* **135** (2), 024106 (2011).
- [215] S. Grimme, *Journal of computational chemistry* **27** (15), 1787 (2006).
- [216] F. Liu and K. Morokuma, *Journal of the American Chemical Society* **135** (29), 10693 (2013).
- [217] N. P. Ernsting, *Chemical physics letters* **159** (5), 526 (1989).
- [218] F. Liu, Y. Kurashige, T. Yanai, and K. Morokuma, *Journal of Chemical Theory and Computation* **9** (10), 4462 (2013).
- [219] G. Scalmani, M. J. Frisch, B. Mennucci, J. Tomasi, R. Cammi, , and V. Barone, *J. Chem. Phys.* **124**, 094107 (2006).
- [220] M. Cossi and V. Barone, *J. Chem. Phys.* **115**, 4708 (2001).
- [221] M. Cossi and V. Barone, *The Journal of Chemical Physics* **112**, 2427 (2000).
- [222] D. Jacquemin, E. A. Perpète, G. E. Scuseria, I. Ciofini, and C. Adamo, *Journal of Chemical Theory and Computation* **4** (1), 123 (2008).
- [223] D. Jacquemin, E. A. Perpète, G. Scalmani, M. J. Frisch, X. Assfeld, I. Ciofini, and C. Adamo, *J. Chem. Phys.* **125**, 164324 (2006).
- [224] G. Scalmani, M. J. Frisch, B. Mennucci, J. Tomasi, R. Cammi, and V. Barone, *J. Chem. Phys.* **124**, 094107 (2006).